

ELECTRODYNAMIC AND THERMODYNAMIC MODELING OF THE
LIGHTNING CHANNEL

A DISSERTATION
SUBMITTED TO THE DEPARTMENT OF ELECTRICAL
ENGINEERING
AND THE COMMITTEE ON GRADUATE STUDIES
OF STANFORD UNIVERSITY
IN PARTIAL FULFILLMENT OF THE REQUIREMENTS
FOR THE DEGREE OF
DOCTOR OF PHILOSOPHY

Can Liang
May 2014

© 2014 by Can Liang. All Rights Reserved.

Re-distributed by Stanford University under license with the author.



This work is licensed under a Creative Commons Attribution-Noncommercial 3.0 United States License.

<http://creativecommons.org/licenses/by-nc/3.0/us/>

This dissertation is online at: <http://purl.stanford.edu/hb119cm6132>

I certify that I have read this dissertation and that, in my opinion, it is fully adequate in scope and quality as a dissertation for the degree of Doctor of Philosophy.

Umran Inan, Primary Adviser

I certify that I have read this dissertation and that, in my opinion, it is fully adequate in scope and quality as a dissertation for the degree of Doctor of Philosophy.

Sigrid Close

I certify that I have read this dissertation and that, in my opinion, it is fully adequate in scope and quality as a dissertation for the degree of Doctor of Philosophy.

Nikolai Lehtinen

Approved for the Stanford University Committee on Graduate Studies.

Patricia J. Gumport, Vice Provost for Graduate Education

This signature page was generated electronically upon submission of this dissertation in electronic format. An original signed hard copy of the signature page is on file in University Archives.

Abstract

Lightning is a form of an electric breakdown of air caused by the strong electric field that is induced by charge accumulation in the cloud during a thunderstorm. During lightning, a current of tens of thousands of amperes flows in the lightning channel and a charge of several coulombs is transferred between different parts of the cloud or between the cloud and the ground. These high-current and high-energy phenomena cause various effects that influence our daily life and the Earth's electromagnetic environment, including near-Earth space. For this reason it is of great interest to improve our understanding of the characteristics of the lightning channel and the fundamental physics underlying the development of lightning.

Lightning consists of physical processes that span a wide range of spatial and temporal scales. Despite decades of research, many questions concerning the fundamental physics of lightning remain unanswered. This lack of understanding is caused by a combination of factors including the difficulty in obtaining high-quality experimental data and the intrinsic complexity in the physical processes involved.

In this work, a numerical model is constructed to handle the electrodynamics and the thermodynamics of the lightning channel as well as the complex geometrical structure of the lightning channel. This model is applied to investigate three lightning processes: the subsequent return stroke, the leader step and the large scale geometrical structure of the lightning channel. The study of the subsequent return stroke reveals that the current and optical waves may propagate along the channel at significantly different speeds. This result has a profound impact on the calculated return stroke electromagnetic radiation, which in turn affects many aspects of lightning-related studies, including lightning geolocation and lightning-upper-atmosphere coupling. The model also predicts a finite time delay between

the return stroke current and optical wavefront. The leader-step study focuses on reproducing the ground-station recordings of the electric field pulse associated with single leader steps. It is demonstrated that a parsimonious model is sufficient to capture the observed characteristics of the waveforms. In the study of the large-scale structure of the lightning channel, a probabilistic model is used to determine the growth and branching of the lightning channel. The model is then applied in a Monte-Carlo type algorithm to determine the probability distribution of the lightning strike locations on the ground given the location of the initial channel in the cloud. The protection efficiency of a metallic rod on the ground is investigated by comparing the estimated probability distributions using simulations that are with or without the metallic rod present on the ground.

Acknowledgments

I would like to take this opportunity to express my sincere gratitude to some of the many people whose insight, guidance, and support have helped make this work possible. First and foremost, I would like to thank my adviser, Professor Umran Inan. Many years ago when I was on the verge of deciding whether to pursue a PhD program, Professor Inan kindly granted me an independent study opportunity in the group, which then became the beginning of my PhD study at the VLF group. Through the last five years, I was continuously inspired by his infectious enthusiasm and dedication to his work, and helped a great deal by his guidance.

I am immensely grateful for the input and counsel of Dr. Nikolai Lehtinen and Dr. Brant Carlson. Both Dr. Lehtinen and Dr. Carlson have been invaluable sources of insights and knowledge. Without their guidance, it would not have been possible for this work to progress nearly as far as it has. I am also greatly thankful for the guidance and help from Dr. Ivan Linscott. I worked with Dr. Linscott during my first year in the VLF group and his insightful suggestions largely shaped my understanding of the research process. I would also like to thank Dr. Morris Cohen and Dr. Robert Marshall. They have been most encouraging and have offered many helpful suggestions over the course of my PhD program.

For their time and for their input, I thank Professor Sigrid Close for joining my reading committee despite her extremely busy schedule and Professor John Gill III, and Professor Philip H. Scherrer who graciously agreed to join my defense committee on short notice.

It has been a great experience to be a part of the VLF group for the past five years. I have benefited extensively from the wide range of expertise in the group and the warm and friendly environment. I would like to thank Forrest Foust and David Strauss for many

discussions that helped me greatly in understanding the numerical methods and Kevin Graf for his help and suggestions for my defense. I would also like to thank the many other individuals in the group: Patrick Bleas, Rasoul Kabirzadeh, Vijay Harid, Fadi Zoghoghly, Chris Young, Andrew Tronson, Daniel Golden, George Jin, Salman Naqvi, Denys Piddychiy, Naoshin Haque. Besides providing a valuable resource, they also helped to make my graduate career so enjoyable. I thank them for a most memorable moments at Stanford and look forward to many continued friendships. I would like to especially thank Shaolan Min and Helen Niu for their help and their patience with my many odd requests.

Finally, I want to thank my parents for their unwavering support and love. Only with their support, it was possible for me to take the rather unusual path of studying in two of the world's most prestigious schools. Especially for my time in Cambridge and my early years in Stanford, despite the heavy financial burden laid on their shoulders, they never brought up their concern during any of our conversations. Their selfless love is one of the most precious gifts in my life. I am also very grateful to my fiancée Qie Hu for being there throughout the trials and tribulations of graduate school. Her company and encouragement has been an immense help during many difficult times.

Chapter 1

Introduction

1.1 Various forms of lightning

As a result of electric charge accumulation in the thundercloud, strong electric fields (up to 150 kV m^{-1}) are established during a thunderstorm both inside the cloud and in the space between the cloud and the ground. When the electric field becomes strong enough, air breakdown takes place, which can eventually evolve into lightning channels. It is generally believed that a lightning channel consists of a highly conductive high temperature air plasma core and a sheath region of much lower conductivity. Once initiated, the lightning channel can propagate through space where the electric field due to the cloud charge distribution is much lower than the air breakdown threshold.

Depending on its location of initiation and the region within which its channel propagates, lightning has been classified into several categories. The generic term used for all forms of lightning discharge is a “lightning flash” or just a “flash”. The majority of lightning flashes (> 90%) are intra-cloud (IC) or cloud-to-cloud (CC). That is, these flashes are initiated inside the cloud, with their channel confined within or close to the cloud, or in the region between clouds. A lightning discharge that involves an object on the ground or in the atmosphere, e.g. an aircraft, is sometimes referred to as a “lightning strike”. From the observed polarity of the charge effectively lowered to ground and the direction of propagation of the initial channel, four different types of lightning discharges between cloud

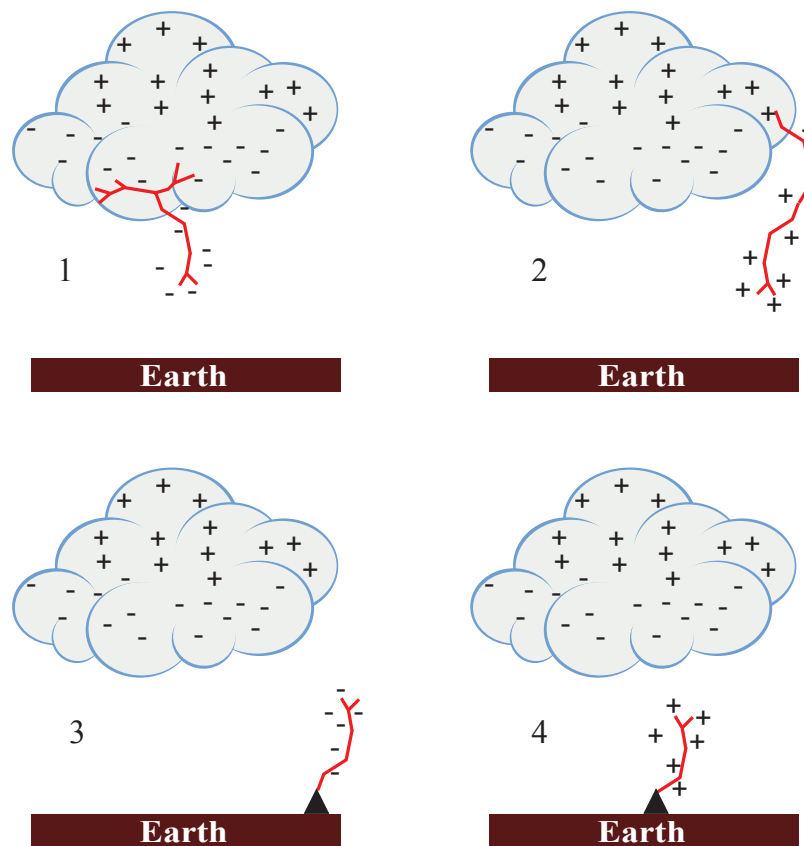


Figure 1.1: Four types of Cloud-to-Ground Lightning: (1) downward negative lightning, (2) downward positive lightning, (3) upward positive lightning, (4) upward negative lightning.

and the Earth have been identified (Figure 1.1): 1) downward negative lightning, 2) downward positive lightning, 3) upward positive lightning and 4) upward negative lightning. Discharges of all four types can be viewed as effectively transporting cloud charge to the ground and therefore are usually termed cloud-to-ground discharges (CGs).

Among the four types of lightning strikes, the downward negative lightning is the most commonly observed. Such lightning initiates in the cloud, develops in an overall downward direction, and transports negative charge to the ground. The overall negative cloud-to-ground flash consists of a number of processes (Figure 1.2). Firstly, as the charge distribution in the cloud develops and the electric field strengthens, an in-cloud process called the preliminary or initial breakdown takes place and lasts from a few milliseconds to some tens of milliseconds. Although there is no consensus on the mechanism of this process,

multi-station electric field measurements and VHF-UHF channel imaging in conjunction with electric field records suggest that the initial breakdown can be viewed as a sequence of channels extending in seemingly random directions from the cloud charge source. Part of the channel eventually extends outside the cloud and grows towards the ground in a series of discrete steps. Each step is typically $1 \mu\text{s}$ in duration and tens of meters in length, with the time interval between steps being 20 to $50 \mu\text{s}$. Each discrete step creates a new portion of the lightning channel, which is called a negative stepped leader. Due to the high conductivity of the lightning channel, several coulombs of negative charge is deposited along the channel as the channel propagates towards the ground. As the leader approaches the ground, the electric field at the ground surface, particularly at objects protruding above the surrounding terrain, increases until it exceeds the critical value for the initiation of one or more upward-connecting leaders. The initiation of an upward connecting leader from the ground in response to the descending stepped leader marks the beginning of the attachment process. This process ends when contact is made between the downward and upward moving leaders, probably some tens of meters above the ground [Rakov and Uman, 2002, Ch.4, p. 111], whereafter the first return stroke begins. A current wave initiates at the connection point and propagates both upward along the channel and downwards towards the ground. When the downward propagating wave reaches the ground, its reflected wave propagates upward along the channel and eventually merges with the upward wave initiated at the connection point. The current wave can have a peak magnitude from a few kA up to well above 100 kA [Rakov and Uman, 2002, Ch.4, p. 145–146]. The joule heating associated with the current wave causes rapid heating in the core, bringing the core temperature well above 30 kK, causing intense optical radiation and fast thermal expansion. The return stroke current typically lasts for a period on the order of $100 \mu\text{s}$ and several coulombs of charge are transferred between the cloud and ground. Sometimes the return stroke is followed by a continuing current stage, which features relatively low current (tens to hundreds of amperes) that lasts for tens to hundreds of milliseconds. The faintly luminous continuing current channel may experience temporary enhancement in the brightness, which is identified as the M-component [Rakov and Uman, 2002, Ch.4, p. 112]. When the first return stroke and any associated in-cloud discharge activities ceases, the flash may end. However, more often than not, after a time period on the order of tens of milliseconds, a

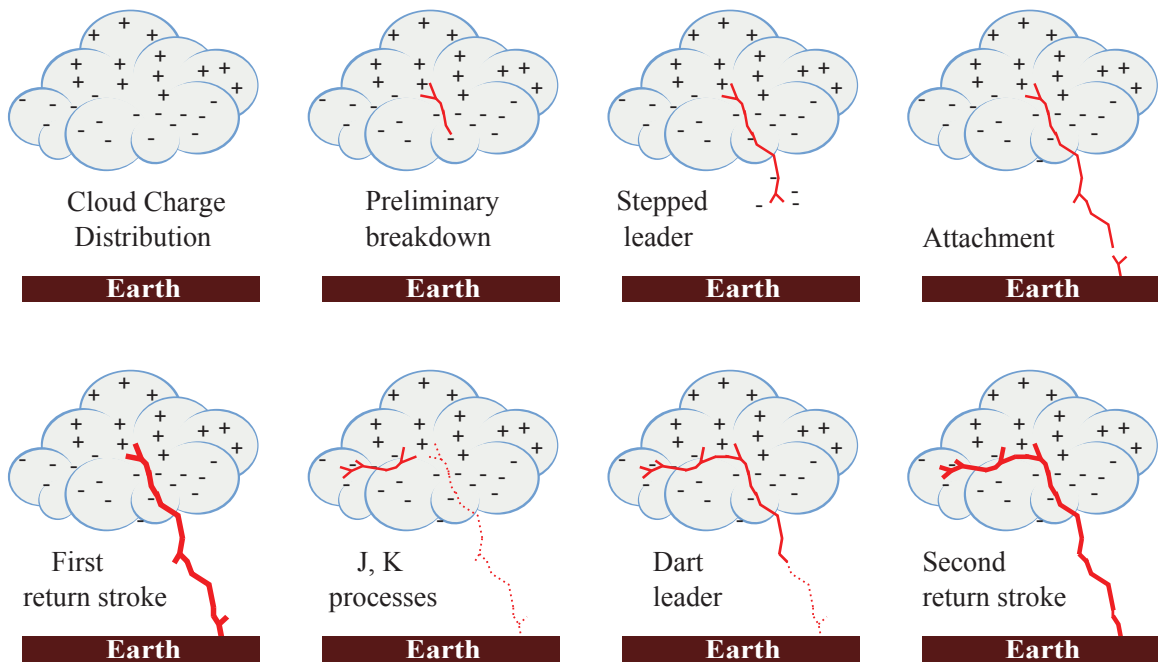


Figure 1.2: Various stages of negative Cloud-to-Ground Lightning

continuously moving leader, called a dart leader, may traverse along the residual of the previous stroke channel, reheating and re-ionizing the channel. Once this leader reaches the ground, another return stroke, called a subsequent return stroke is initiated. During the time interval between the end of the previous return stroke and the initiation of a dart leader, J and K-processes occur in the cloud [Rakov and Uman, 2002, Ch.4, p. 112]. The K-process can be viewed as a transient occurring during the slower J-process. The J-process amounts to a redistribution of cloud charge on a time scale of tens of milliseconds.

1.2 Lightning induced phenomena

1.2.1 The distant lightning electromagnetic environment

Lightning flashes induce electromagnetic radiation over a wide spectrum at all phases and stages, and most noticeably, during the return stroke. At frequencies below 30 kHz, both the ionosphere and the ground appear to be highly conductive and together they form the

Earth-ionosphere waveguide for the lightning induced electromagnetic waves to propagate over thousands of kilometers. These long range signals carry much information about the ionosphere and have been used as a probe for the study of ionospheric conditions. Moreover, lightning detection networks that are capable of tracking the magnitude and location of lightning in real time on national or even global scales have been constructed based on the use of these long-range signals [*Said et al.*, 2010].

Part of the ELF and VLF energy components of the upward-propagating electromagnetic radiation from the causative lightning discharge can traverse the ionosphere and travel along the geomagnetic field lines in the magnetosphere to the opposite hemisphere in the form of a so-called whistler-mode wave [*Helliwell and Katsufakis*, 1974]. During its propagation through the magnetosphere, the whistler-mode wave can interact with energetic electrons in the radiation belts. Such interactions can result in amplification of the wave, triggering of emissions at new frequencies, as well as precipitation of some of the energetic electrons, which in turn modifies the ionospheric properties [e.g., *Inan and Carpenter*, 1987]. These type of signals are an important source of information for the study of the Earth's magnetosphere.

1.2.2 Effects in the middle and upper atmosphere

Three general types of low-luminosity transient optical phenomena that occur in the clear air above thunderstorms have been observed: sprites, jets, and elves [*Rakov and Uman*, 2002, Ch.14, p.480]. The location and appearance of sprites, jets, and elves are illustrated in Fig. 1.3. Blue starters and blue jets, subtypes of jets, propagate upward from the top of the cloud, generally at a height of 20 km or less, in the form of blue, cone-shaped structures [*Wescott et al.*, 1995]. They are apparently not necessarily associated with any individual cloud-to-ground lightning. Sprites are most luminous between 40 and 90 km heights, are mostly red in color, and often have faint bluish tendrils extending downward from 50 km or so to altitudes as low as 20 km [*Sentman et al.*, 1995]. Sprites exhibit a diversity of forms and features and generally occur in association with the larger positive cloud-to-ground flashes [*Bocippio et al.*, 1995]. Elves are circles of light expanding radially across the bottom of the ionosphere and are likely to be caused by the acceleration of electrons in the

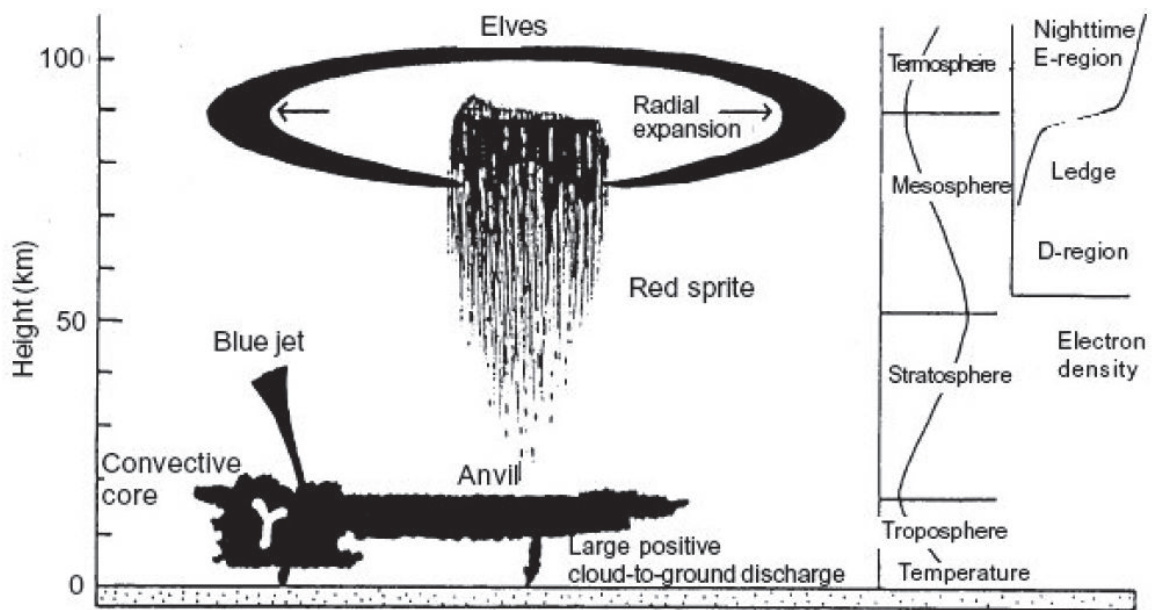


Figure 1.3: Lightning related phenomena in the upper atmosphere [Sharma *et al.*, 2004]

lower ionosphere by radiation fields of return strokes [Inan *et al.*, 1991, Boeck *et al.*, 1992, Fukunishi *et al.*, 1996]. Lightning can also lead to the production of X-rays, gamma-rays, and relativistic runaway electrons [Lehtinen *et al.*, 1999].

Some of the phenomena discussed above, as well as the electron precipitation caused by lightning-induced whistlers, change the properties of the lower ionosphere and hence alter the ELF/VLF wave propagation in the Earth-ionosphere waveguide as well as the trans-ionospheric propagation [Helliwell *et al.*, 1973].

1.2.3 Lightning effects on the chemistry of the atmosphere

Various forms of atmospheric electrical discharges, including the corona on thundercloud water droplets and ice particles, various types and phases of lightning discharge, and the sprites, blue starters, blue jets, and elves occurring in the region between the cloud tops and the ionosphere, produce new trace molecules from the ambient constituents of the atmosphere. Nitric oxide, NO, is the most important electric-discharge-produced molecule, primarily because it facilitates chemical reactions that determine the concentrations of ozone,

O₃, and of the hydroxyl radical OH [e.g., *Crutzen, 1970, Chameides and Walker, 1973*]. In particular, the current-carrying lightning channels of initial breakdown processes, leaders, return strokes, M-components, continuing currents, K and J-processes generate primarily NO as a trace gas with considerably less NO₂. But NO, once present, is always accompanied by the NO₂ produced from atmosphere oxidation of NO.

Many aspects of lightning study play an important role in the quantitative understanding of NO production. For example, the thermodynamics, especially the cooling of the core determines the NO production per channel core length [*Hill et al., 1984*]. Moreover, since all the lightning channels in the various processes comprising cloud and ground discharges can contribute to the NO production, detailed data on the geometry of lightning channels and the global lightning flash rate are thus essential for the estimation of the global production rate of NO production [*Rakov and Uman, 2002, Ch. 15, p. 513*].

1.2.4 Lightning induced damage

Lightning inflicts damage to a wide range of objects and systems, including electronic integrated circuits, trees, electric power and communication systems, buildings, boats, and aircrafts. The type and amount of lightning damage that an object suffers depends on both the characteristics of the lightning discharge and the properties of the object. Some of the characteristics of lightning of interest in this respect are the various properties of the current waveform and of the electromagnetic fields.

For objects that are in direct contact with the lightning channel, damage is caused by the high current and the induced high voltage and intense heating. Four aspects of the lightning current waveform are important in assessing this form of damage: (i) the peak current, (ii) the maximum rate of change of current, (iii) the total amount of charge transferred and (iv) the integral of the current square over time. For conducting objects such as power lines and electronic circuits, lightning can also induce damage without direct contact, but through the radiated electromagnetic pulse by inducing currents and resultant voltages in those objects. This type of damage is directly related to the peak values and the maximum rates of change of the electric and magnetic fields, both are in turn determined by the maximum rate of the change of current.

Currently available lightning protection designs may be classified into two categories: (i) diversion and shielding with metallic constructs for structural protection and for reducing the lightning electric and magnetic fields within the structure, and (ii) surge protection to limit the of currents and voltage induced in electronic, power, and communication systems. Knowledge of the lightning return stroke characteristics is essential for the design of the protection system.

1.3 Highlights of current research on lightning

Lightning involves a collection of physical processes that are of vastly different temporal and spatial scales. Current lightning research is rich both in quantity and variety, but many questions about the fundamental physics underlying these processes remain unanswered. Difficulties arise both from the need for observations of extremely high temporal and spatial resolutions and the intrinsic complexity of the physics involved. It is beyond the scope of this thesis to provide a comprehensive account of all the topics related to lightning studies. In this section, we briefly discuss some of the existing experimental techniques and numerical models that are relevant to the studies presented in this thesis. The relevant theory of the lightning processes is discussed in Chapter 2.

1.3.1 Experimental techniques

Electromagnetic observations - field and current

Recordings of the electric and magnetic fields associated with lightning processes at multiple stations on the ground have been one of the primary data types used for lightning studies. Depending on the frequency range of observation, different types of studies can be performed with such data. Recordings of electromagnetic field pulses in the MHz range are believed to be associated with the leader stepping process. These types of recordings can be used to identify the spatial coordinates and time at which the events take place. An example of this type of system is the Lightning Mapping Array (LMA) which uses VHF radiation from leader steps to study the spatial and temporal evolution of the lightning channel structure inside the cloud [Rison *et al.*, 1999]. Electromagnetic radiation in the VLF and ELF

range radiated by return strokes propagates within the Earth-ionosphere waveguide over hundreds up to thousands of kilometers. These type of recordings can be used to provide information on the location, magnitude and polarity of lightning return strokes on a global scale. An example is the NLDN system [Cummins *et al.*, 1998]. Recordings at lower frequencies have been used to study the overall thundercloud charge structure and to estimate the location and magnitude of charge removal by individual return strokes [Krehbiel *et al.*, 1979].

In-situ measurements of the electric and magnetic fields with aircraft and balloons provide more accurate data on the fields inside the thundercloud. However, this type of data can only cover a very small spatial region of the cloud.

Recordings of the return stroke current at the ground are made available by experiments that control the strike location using towers or rocket triggering techniques. These data provide high time resolution information on the return stroke current waveform, but are limited to the measurement of only the ground current.

1.3.2 Optical observation

Optical observations provide information on the thermodynamics of the lightning channel. High resolution data in this category can only be obtained for the portion of the lightning channel outside the thundercloud. Some typical recording systems used are still cameras, streak cameras, high time resolution cameras, photoelectric diodes and spectrometers. Note that data provided by these systems are relatively limited in temporal and spatial resolutions. In particular, they are insufficient to reveal quantitative information about processes such as the streamers, sheath formation and streamer-leader transition in natural lightning.

Still camera recordings are used to reveal the geometry of the lightning channels. Streak camera recordings provide information on the temporal and spatial evolution of the lightning channel, and have been used to observe the various stages of return strokes. More quantitative data such as the stepped leader, dart leader and return stroke propagation speeds and the leader step length can also be extracted from the streak camera data. Photoelectric diode recordings provide high time resolution recordings of optical radiation for small segments of the return stroke channel. Such recordings often serve as an alternative technique

for the various speed measurements. The spectroscopy of the lightning channel, obtained by spectrometers, provides information on the temporal evolution of the thermodynamic properties of the lightning channel. This type of data is often limited to a time resolution of several microseconds.

Triggered lightning

Triggered lightning refers to the discharges intentionally stimulated to occur by ground-based activity, while the primary energy source is a naturally electrified cloud. The most commonly used technique involves the launching of a small rocket that extends a thin wire (either grounded or ungrounded) into the gap between the ground and the thundercloud [Rakov and Uman, 2002, Ch. 7, p. 267]. A distinct advantage of the triggered lightning system is the control of the time and spatial location of the lightning channel and the strike location. Although the initial strike in the triggered lightning can have different characteristics from the first return stroke in natural downward lightning, the dart leaders and the following return strokes in triggered lightning are similar to “dart-leader to upward-return-stroke” sequences in natural lightning.

Triggered lightning is an excellent source of experimental data for the study of subsequent return strokes and related processes. The better control of the experimental environment has allowed for optical observations of higher spatial and temporal scales and has made possible a number of new insights into the various lightning processes and effects. Furthermore, with triggered lightning, it is possible to obtain data of synchronized observations of the optical radiation, electromagnetic radiation and ground current. As discussed in Chapter 4, this type of synchronized observation greatly facilitates the study of the physics of lightning.

Laboratory study

With its much better controlled experimental environment, laboratory studies with long spark discharges often provide data of much higher spatial and temporal resolutions in comparison with observations of natural lightning. However, it is important to bear in mind that the validity of the assumption of the similarity between a lightning discharge and

a laboratory spark in terms of the various processes comprising the leader and the initiation criteria for each of these processes is yet to be confirmed.

The study of spark channel formation and growth provides many useful insights on the physical processes associated with streamers and streamer-leader transition. One example is the description of the development of the negative stepped leader given by *Bazelyan and Raizer* [1997, Ch. 6, p. 254] based on observations using electronic image-converter cameras in conjunction with measurements of the current through the air gap.

Studies of the temporal and radial evolution of the thermodynamic properties of the spark channel, with the current through the channel being specified to match the observed return stroke current at the ground, often serve as the experimental foundation for models, such as the gas dynamic models [*Rakov and Uman*, 1998], that aim at reproducing the thermodynamics in the radial direction of a small segment of the lightning channel.

1.3.3 Modeling of lightning processes

Models for lightning processes such as initial breakdown, attachment, J and K- processes are at a relatively underdeveloped stage due to limited theoretical understanding and experimental data. On the other hand, several models for return stroke, dart leader, stepped leader and M-component are relatively well established. That is, these models are verified against experimental data in terms of their ability to reproduce certain aspects of the physical processes involved in the lightning discharge.

Stepped leader models

The stepped leader stage is a very complicated physical process involving sub-processes of distinctly different temporal and spatial scales (section 2.4). A variety of models have been devised to capture different aspects of the stepped leader process.

One type of model explicitly includes the stepping mechanism. An example is the model proposed by *Bondiou-Clergerie et al.* [1996]. In this model, the downward negative stepped leader is treated by using fluid dynamics in conjunction with the phenomenological characteristics of various processes in laboratory sparks. The model prediction was shown to be consistent with the observations in altitude-triggered lightning [*Laroche et al.*, 1991].

Another type of model, as presented in *Klingbeil and Tidman* [1974], treats the stepping by taking into consideration of the photon ionization of the neutral air in front of the leader tip and solving a set of one-dimensional equations that govern the dynamics of the plasma.

Finally, there is a class of stepped leader models that focus on the large scale geometry of the stepped-leader channel, including its tortuosity and branching. This type of model uses a probabilistic calculation to determine the location, length and direction of subsequent leader steps and aims at studying the channel distribution in space and the corresponding charge distribution in the channel. An example is the fractal model proposed by *Niemeyer et al.* [1984].

Return stroke models

Based on the governing equations, return stroke models are classified by *Rakov and Uman* [1998] into the following four categories:

(1) The gas dynamic models are primarily concerned with the radial evolution of a short segment of the lightning channel. By solving the hydrodynamic equations for high-temperature plasma, these models output the time evolution of the radial distribution of temperature, pressure, electric conductivity and optical radiation intensity.

(2) The electromagnetic models output the current distribution along the channel by finding a numerical solution of Maxwells equations, based on a lossy thin-wire antenna approximation to the lightning channel. This type of model is considered to be the most accurate among the three models listed here as (2), (3) and (4).

(3) The distributed circuit models can be viewed as an approximation to the electromagnetic models. They represent the lightning discharge as a transient process on a vertical transmission line characterized by resistance, inductance and capacitance.

(4) The engineering models directly specify the spatial and temporal distribution of the channel current or the channel line charge density, using the observed return stroke current at the ground, the speed of upward propagating from and the channel luminosity profile.

Dart leader models

One category of dart leader models describes the ionization processes within the dart-leader front and aims at reproducing the propagation characteristics of the dart leader, especially its front propagation speed. Unfortunately, existing models in this category are either unable to produce correct front propagation speed or suffer from insufficient experimental data for determination of the model parameters [Loeb, 1965]. For example, *Jurenka and Barreto* [1982] assume that the residual channel in front of the dart leader to be weakly ionized and treat it as a gas consisting of three components: neutral particle fluid, ion fluid and electron fluid. They use one-dimensional hydrodynamic equations in conjunction with Poisson's equation to resolve the dynamics of the electron fluid while assuming the neutral and ion fluids to be stationary for the time frame of concern. In this model, the dart leader front propagation is driven by the electron fluid pressure wave. *Borovsky* [1995] points out that this electron-pressure driven wave model is insufficient based on the following considerations: 1) the electron-pressure driven wave propagation speed is limited below the electron thermal velocity behind the wave front, which is about $7 \times 10^5 \text{ m s}^{-1}$ at the temperature as high as 30 kK. This speed is an order of magnitude lower than the observed dart-leader propagation speed; 2) the electron pressure waves can only propagate over a distance less than 1cm; 3) the electron pressure cannot transport energy fast enough to account for the air ionization and heating. Furthermore, *Bazelyan* [1995] suggests that electron impact ionization should be taken into account when modeling dart leaders.

Another category of the dart leader models puts emphasis on achieving agreement between the model predictions and the measured electric fields. The most frequently used model of this type treats the dart leader as a uniformly charged line emerging from the center of a volume of charge in the cloud and extending at a constant speed vertically towards the ground. The channel linear charge density and the dart-leader front propagation speed are the two model parameters for this type of model. An example of the usage of these type of models is presented by *Rubinstein et al.* [1995], in which the model parameters are inferred by comparing the predicted electric fields with the measured electric fields produced by triggered lightning leaders.

1.4 Contributions of this work

This dissertation focuses on the development of a numerical model that more accurately captures the physics of the lightning channel and the application of this model to the study of various lightning processes, in order to achieve better understanding of the fundamental physics underlying these processes. More specifically, based on the Time Domain Fractal Lightning (TDFL) model developed by *Carlson et al.* [2010], the following improvements are introduced:

- (1) Reformulation of the numerical scheme that achieves a higher order of accuracy.
- (2) Inclusion of the thermodynamics of the lightning channel.
- (3) Inclusion of an empirical corona sheath model.
- (4) Inclusion of a phenomenological leader model.

This improved model is applied to study the return stroke, the stepped leader and the large scale lightning channel structure from which the following results are obtained:

(1) In the return stroke study, we demonstrate that the return stroke current and optical wave propagation speeds are significantly different, and that there is a finite time delay between the return stroke current and optical wave front.

(2) In the stepped leader study, we demonstrate that the model can produce electric fields on the ground in agreement with experimental recordings, with physically reasonable model parameter values.

(3) In the study of large scale lightning channel structure, we determine the probability distribution of lightning strike location at the ground given an initial channel location in cloud.

In the following chapters, we first describe the theoretical understanding of lightning physics in Chapter 2 and the numerical techniques in Chapter 3. We then present the study of the return stroke, the stepped leader and the large scale lightning channel structure in Chapters 4, 5 and 6.

Chapter 2

The Physics of Lightning Channel

The physical processes involved in lightning flashes span a wide range of spatial and temporal scales. In this chapter, we describe several of the physical processes that are essential for the studies presented in later chapters. Our discussion reveals that many of the processes are poorly understood and it is thus generally difficult to construct a physically accurate model. However, the physics of the highly conductive lightning channel itself is relatively well understood, and we provide a detailed description of the system of equations that govern its electrodynamics and thermodynamics. Much of the rationale behind the design of the models for the studies presented in Chapters 4, 5 and 6 is based on the understanding of the weakness and strength of currently available theories.

2.1 Lightning-producing clouds

The primary type of cloud associated with lightning is termed cumulonimbus, commonly referred to as the thundercloud. The most common feature of the cloud charge structure includes a net positive charge near the top, a net negative charge below it, and an additional small amount of positive charge at the bottom of the cloud. Most of the cloud electric charges reside on hydrometeors, i.e., various liquid or frozen water particles in the atmosphere. The electrification mechanism and the distribution and motion of thunderstorm electric charges are topics of active research.

Because the gravity-driven thundercloud motion is only significant over time scales

much longer than the duration of a lightning flash (~ 1 ms), such motion and the associated charge distribution variation can be neglected as far as the lightning dynamics is concerned. The spatial distribution of the cloud charge is primarily inferred from in situ measurements and multi-ground-station recordings of the electric field. These studies normally report values that represent certain type of averages over regions of several kilometers in radius. The lack of accurate information of the three dimensional spatial distribution of cloud charge and the associated electric field pose limitations in various aspects of lightning study (Section 2.4.3, and Chapters 5, 6).

2.2 Streamers

A streamer is a form of electric discharge that takes place in many phases and stages of lightning flashes. For example, it plays a critical role in the initiation and growth of the lightning channel (section 2.4), and the formation of the charge storage component of an existing lightning channel, i.e., the corona sheath (section 2.3.3). Many aspects of the streamer and its related processes are still under active research and physically accurate models for these processes are in general unavailable. In this section, we describe some of basic characteristics of streamers that we rely upon for the construction of semi-empirical models for various components of the lightning system.

A streamer is a filamentary air plasma channel whose radius can be thousands of times smaller than its length. The plasma in the streamer channel is created by electron avalanche breakdown of the air in front of the streamer tip. The avalanche breakdown requires the presence of a very strong electric field, e.g., 3 MV m^{-1} in SATP (standard ambient temperature and pressure) air. However, a streamer is capable of propagating in an external electric field that is much lower than the air electric breakdown threshold, because the weak external field causes charge accumulation at the streamer tip which in turn induces an electric field that is strong enough to cause avalanche breakdown of the air at the front of the tip. Experimental observations show that the radius of the tip stays constant at a value on the order of 10^{-1} cm for SATP air as the streamer propagates. Moreover, the lateral expansion of the channel behind the tip is shown to be at a speed much lower than the elongation. Descriptions of various experimentally observed streamer characteristics can be found in

Bazelyan and Raizer [1997, Ch. 5, p. 145–155].

The dynamics of the streamer can be thought of as consisting of two distinct parts: the fast processes at the streamer tip and the relatively slow processes in the streamer channel behind the tip.

The fast processes at the streamer tip include the ionization, electron drift and the resulting charge redistribution. In this context, it is particularly important to emphasize that the ionization rate at the leader tip is directly determined by the electric field strength, because the streamer plasma is weakly ionized. These processes together determine the streamer propagation characteristic, such as the propagation speed, the streamer tip radius, streamer tip charge, the degree of ionization and the initial channel conductivity. Accurate treatment of these processes requires sophisticated numerical modeling and is a challenging research topic of its own. Several models in this category is described in *Bazelyan and Raizer* [1997, Ch. 5, p. 176–193]. Also, analysis with a quasi-stationary one-dimensional model is presented in *Bazelyan and Raizer* [1997, Ch. 3, p. 43–53]. The model solves the system of equations consisting of Poisson’s equation and the continuity equation for the electron and ion densities, while using an analytical formula to determine the ionization rate as a function of the electric field strength. The model gives expressions for quantities such as the streamer tip charge density, electron density and propagation speed in terms of the streamer tip radius. The problem of streamer head radius is yet to be solved, for which a brief discussion is given in *Bazelyan and Raizer* [1997, Ch. 3, p. 47].

The relatively slow processes taking place in the streamer channel behind the tip include processes such as the channel lateral expansion, charge re-distribution in the channel and the attachment of free electrons to heavy particles. A related topic is the energy balance and heating in the channel. As is pointed out in *Bazelyan and Raizer* [1997, Ch. 3, p. 67–71], the heating of a single streamer is insufficient to significantly increase the temperature of the heavy particles. As a result, free electrons created by the ionization process at the streamer tip quickly become attached to heavy particles and the plasma loses most of its conductivity once the streamer tip propagates away from the current location. Hence, in order for a streamer to maintain its conductivity, strong electric fields must always be present inside the streamer.

So far we have assumed that the streamer has already been created. Another topic of

great importance is the inception of streamers. Knowledge of this process is essential for the determination of the initiation of lightning, the condition for channel growth and core-sheath charge transfer. *Bazelyan and Raizer* [1997, Ch. 3, p. 76–83] provides a discussion on the conditions for the electron avalanche and avalanche-steamer transition.

Another topic of great importance is the behavior of a group of streamers. Although we focus our discussion on a single streamer, in real lightning processes numerous streamers are initiated simultaneously. Moreover, each streamer branches into (and sometimes merges with) several streamers as it propagates. For example, as discussed in section 2.4, the streamers initiated from the lightning channel leader tip collectively form a streamer zone, which plays a critical role in the formation of new lightning channel segments. The collective behavior of a large number of streamers is significantly more difficult to study quantitatively, both theoretically and experimentally. These difficulties are the primary reasons that empirical models are often needed for lightning study.

2.3 The Lightning Channel

In comparison with the other aspects of the lightning process, the physics of the lightning channel is relatively well understood. The lightning channel, often referred to as the leader channel, is generally considered to consist of a hot plasma core at the center and a charge sheath surrounding the core (Figure 2.1). In the radial direction, \hat{r} , the dimension of the core is on the order of 1 cm, while that of the sheath is on the order of meters to tens of meters. In the axial direction, \hat{z} , the lightning channel is several kilometers in length. The core carries most of the current, and the sheath stores most of the charge that is deposited along the channel.

As discussed below, it is appropriate to further divide the core into two sub-components: the bulk and the boundary of the core. The bulk of the core is the highly ionized hot plasma region. For example, for the return stroke channel discussed in Chapter 4, the temperature and pressure of the bulk of the core are at ≥ 20 kK and 1 atm or higher. In this temperature and pressure range, the free electron density n_e is of the order of 10^{22} m^{-3} or higher and the electron thermal velocity is of the order of 10^6 m s^{-1} . Correspondingly, the mean free path for collisions between free electrons is of the order of $1 \mu\text{s}$ and the time for the free

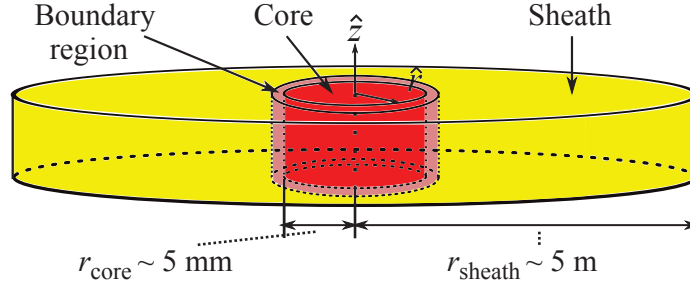


Figure 2.1: The lightning channel structure

electrons to establish a Maxwell velocity distribution is of the order of 10^{-12} s [Zel'dovich and Raizer, 2002, Ch. 6, p. 419]. Similarly, for the heavy particles, the time to establish a Maxwell velocity distribution is on the order of 10^{-10} s. Under these conditions, it is valid to treat the air plasma in the bulk as consisting of an electron and heavy particle gas, while assuming that the excitation and ionization of the heavy particle gas is kept at thermal equilibrium with the electron gas at T_e . In other words, the particle composition of the plasma is determined by the Saha equilibrium equation evaluated at T_e . The bulk region is highly conductive and carries most of the lightning current.

The boundary region of the core is the interface between the bulk of the core and the sheath region. Across the boundary region, the plasma temperature drops from over 10 kK down to almost the room temperature and the free electron density n_e decreases by many orders of magnitude. The plasma state here is much more complicated than that of the core, because it is not in equilibrium and it becomes necessary to consider different types of particles (O_2 , O , O^+ , N , N^+ etc) separately and the finite rate of ionization by electron impact and photon ionization.

The sheath region is formed by numerous streamers that are initiated near the boundary of the core and propagate away from the core. As discussed in section 2.2, a streamer provides little heating to the heavy particles. Hence, after a streamer propagates through a particular location in the sheath, the free electrons quickly become attached to the heavy particles to form a medium of much lower conductivity, so that the sheath region essentially stays at the ambient temperature. Because of the low temperature and the fact that the electrons are attached to the heavy particles forming negative ions, the recombination process of positive and negative ions is very slow, and the sheath plasma is far from being

in thermal equilibrium. In summary, the dynamics of the sheath plasma is governed by a set of processes that are distinctly different from those that take place in the core.

In the following three sections, we first describe some of the equations that govern the dynamics of the bulk and the boundary of the core, and then summarize the current understanding of the sheath region.

2.3.1 The bulk of the core

The bulk of the core is assumed to consist of two gas components: the electron gas (subscript “e”) and the heavy particle gas (subscript “h”), which include all particles other than the electrons, both neutral and ionized. Once the initial composition of the air is known, the states of each of these two gases are fully described by two quantities: their temperatures (T_e , T_h) and pressures (p_e , p_h), or, equivalently, their temperatures and particle densities (n_e , n_h). The heavy particle electronic energy states are assumed to be in partial thermal equilibrium with the electron gas. In other words, T_e is used to calculate the degree of heavy particle ionization and excitation. Generally speaking, this assumption of partial thermal equilibrium does not necessarily hold under all conditions, especially when the process under consideration involves very fast dynamics. For example, the validity of this assumption is investigated in Chapter 4. The temperature of the translational motion of the heavy particles is allowed to differ from T_e and is denoted by T_h . This difference is necessary because of the inefficient energy transfer between electrons and nuclei due to their large mass difference. For the highly ionized plasma in the core, the difference between the densities of positively and negatively charged particles caused by net charge accumulation in the core is negligible in comparison with the densities of the charged particles. To be more specific, the net charge density is given by the following formula:

$$\rho = \sum_i q_i n_i$$

where i denotes the particle species in the plasma, i.e. $i = e, O, O^+, N, N^+$ etc. The particle density and the charge per particle for species i are denoted by n_i and q_i respectively. In

the core, we have

$$\rho \ll q_e n_e$$

As a result, for the calculation of the chemical composition of the plasma in the core using Saha equilibrium equations, the quasi-neutrality assumption can be used. i.e.

$$\sum q_i n_i = \rho \simeq 0$$

The thermodynamic properties of the plasma are then determined by the temperature and the chemical composition of the plasma, as in *D'Angola et al.* [2008].

We now describe the equations that govern the electrodynamics and thermodynamics of the bulk of the core. Note that when the individual components of a vector \mathbf{X} are discussed, it is cast in cylindrical coordinates such that \hat{z} axis is aligned with the axial direction of the core and the origin is located at the center of the core i.e.

$$\mathbf{X} = X^z \hat{z} + X^r \hat{r} + X^\phi \hat{\phi}$$

We further assume cylindrical symmetry, that is that the terms involving a derivative with respect to $\hat{\phi}$ are all zero.

The electric field at any location and any time is calculated using the Electric Field Integral Equation (EFIE) [*Jackson*, 1999, Ch. 6, p. 246–248].

$$\mathbf{E}(\mathbf{x}, t) = \frac{1}{4\pi\epsilon_0} \int d^3\mathbf{x}' \left\{ \frac{\hat{\mathbf{R}}}{|\mathbf{R}|^2} [\rho(\mathbf{x}', t')]_{\text{ret}} + \frac{\hat{\mathbf{R}}}{c|\mathbf{R}|} \left[\frac{\partial \rho(\mathbf{x}', t')}{\partial t'} \right]_{\text{ret}} - \frac{1}{c^2|\mathbf{R}|} \left[\frac{\partial \mathbf{j}(\mathbf{x}', t')}{\partial t'} \right]_{\text{ret}} \right\} \quad (2.1)$$

where \mathbf{x} and \mathbf{x}' denote position vectors in space, t and t' denote time, $\mathbf{R} = \mathbf{x} - \mathbf{x}'$, $\hat{\mathbf{R}}$ is a unit vector in the direction of \mathbf{R} , $\rho(\mathbf{x}', t)$ and $\mathbf{j}(\mathbf{x}', t)$ represent respectively the charge density and the current density at point \mathbf{x}' in space and at time t , $[\]_{\text{ret}}$ means that the expression in the bracket is evaluated at the retarded time, i.e., at $t' = t - (|\mathbf{R}|/c)$. The basic element under the integration sign is the time domain Green function for Maxwell's equations for the electric field \mathbf{E} , as illustrated in Figure 2.2. The EFIE provides a physically accurate description of the electric field due to a set of current and charge sources through

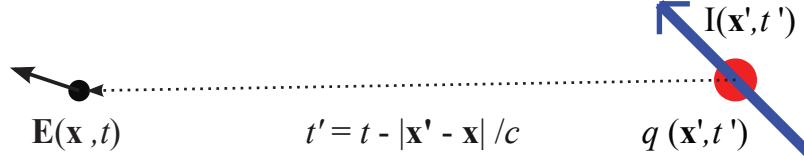


Figure 2.2: The basic element of EFIE

convolution with the time domain Green function over the entire spatial region of concern. In the case of lightning flashes, regions that contribute to the integral include the core, the sheath, the background cloud, the ground and other conducting objects if present. The cloud charge and its image ground charge evolve over a time scale much longer than the entire duration of a lightning flash. For the time window considered ($\sim \mu s$), these charges can thus be taken as constant in time and the induced electric field can be specified as an input to the model. For the sheath region, as discussed in Chapter 3, only the term involving $[\rho(\mathbf{x}', t')]_{\text{ret}}$ needs to be included. All three terms need to be considered for the core region.

Under the assumption that the heavy particle electronic energy states are in partial thermal equilibrium with the electron gas at T_e , we obtain that n_e and n_h are functions of T_e and the initial conditions, i.e., initial temperature T_0 and initial pressure p_0 . The functional values are found by solving Saha equilibrium equations with the constraints of charge quasi-neutrality [D'Angola *et al.*, 2008]:

$$n_e = n_e(T_e, T_0, p_0) \quad (2.2)$$

$$n_h = n_h(T_e, T_0, p_0) \quad (2.3)$$

Next are the momentum conservation equations for the electron gas (the gravity terms are not included due to their smallness):

$$n_e m_e \frac{D\mathbf{U}_e}{Dt} = -\nabla p_e + \nabla \cdot \boldsymbol{\tau}_e + q_e n_e \mathbf{E} + \mathbf{J}_e \times \mathbf{B} - n_e m_{eh} \nu_{eh} (\mathbf{U}_e - \mathbf{U}_h) - m_e \mathbf{U}_e w_e \quad (2.4)$$

and for the heavy particle gas:

$$n_h m_h \frac{D\mathbf{U}_h}{Dt} = -\nabla p_h + \nabla \cdot \boldsymbol{\tau}_h + q_h n_h \mathbf{E} + \mathbf{J}_h \times \mathbf{B} + n_e m_{eh} \nu_{eh} (\mathbf{U}_e - \mathbf{U}_h) - m_h \mathbf{U}_h w_h \quad (2.5)$$

The left hand side of either of the two equations is the acceleration of electron (heavy particle) gas; D/Dt is the substantial derivative; $m_{e,h}$ is the mass of a single electron (average heavy particle); $\mathbf{U}_{e,h}$ is the average velocity vectors of the electron (heavy particle) gas; $\nabla p_{e,h}$ and $\nabla \cdot \boldsymbol{\tau}_{e,h}$ are the gradients of the electron (heavy particle) gas bulk pressure and shear tensor; \mathbf{B} is the magnetic field (in general, \mathbf{B} can be calculated using the Magnetic Field Integral Equation, an analog of Equation (2.1)); the term $n_e m_{eh} \nu_{eh} (\mathbf{U}_e - \mathbf{U}_h)$ represents collisions between electron gas and heavy particle gas, where ν_{eh} is the collision frequency; $w_{e,h}$ is the rate of electron particle (heavy particle) density change due to ionization and recombination; $m_e \mathbf{U}_e w_e$ and $m_h \mathbf{U}_h w_h$ are respectively the changes in momentum due to electron and heavy particle density variation.

The equations of energy conservation for the electron gas and the heavy particle gas are:

$$\frac{\partial n_e \epsilon_e}{\partial t} + \nabla \cdot (n_e \mathbf{U}_e \epsilon_e) = \nabla \cdot (\kappa_e \nabla T_e) - \nabla \cdot (\mathbf{U}_e \cdot p_e) + \mathbf{J}_e \cdot \mathbf{E} - P_{\text{col}}^{\text{elas}} - \frac{\partial n_h \epsilon_h^{\text{int}}}{\partial t} + P_{\text{opt}}^{\text{tot}} \quad (2.6)$$

$$\frac{\partial n_h \epsilon_h}{\partial t} + \nabla \cdot (n_h \mathbf{U}_h \epsilon_h) = \nabla \cdot (\kappa_h \nabla T_h) - \nabla \cdot (\mathbf{U}_h \cdot p_h) + \mathbf{J}_h \cdot \mathbf{E} + P_{\text{col}}^{\text{elas}} \quad (2.7)$$

Equation 2.6 includes all the energy terms that are related to the translational motion of the electrons and the electronic states of the heavy particle. In this equation, $\epsilon_e = (3/2)kT_e$; $P_{\text{col}}^{\text{elas}}$ is the elastic collision energy transfer between the electron gas and the heavy particle gas; $(\partial \epsilon_h^{\text{int}})/(\partial t)$ is the rate of change of the heavy particle electronic states energy. This term is included in Equation (2.6) rather than Equation (2.7) because of the assumption that the heavy particle electronic energy states are in thermal equilibrium with the electron gas. $P_{\text{opt}}^{\text{tot}}$ is the total optical radiation loss of the entire spectrum at a location and is equal to the divergence of the optical radiation intensity field. For the temperature and pressure range considered, variation in energy stored in the radiation intensity field may be neglected [Zel'dovich and Raizer, 2002, Ch. 2, p. 141]. The radiation intensity field is found by solving the radiation transport equations, which in turn requires knowledge of

the photon emission and absorption properties of the plasma [Zel'dovich and Raizer, 2002, Ch. 5, p. 331-338]. Note that for photons at different frequencies, the absorption length can be significantly different and thus the core may appear to be optically thin, or thick, or somewhere in between. Under the assumption that the heavy particle electronic energy states are in thermal equilibrium with the electron gas, the photon emission and absorption properties of the plasma are fully determined by T_e and n_h .

Equation 2.7 for the heavy particle gas includes all the energy terms that are related to the kinetic (i.e., translational) motion of the heavy particles. Note that the term P_{col}^{elas} in Equation 2.6 also appears in Equation 2.7 but with the opposite sign. In other words, the electron gas loses its kinetic energy to the heavy particle gas through elastic collisions.

Finally, the ideal gas law is used to relate the pressures to the temperatures, because the deviation from ideal gas due to coulomb interaction between gas particles is found to be negligible for the temperature and pressure range considered [D'Angola *et al.*, 2008]:

$$p_e = n_e k T_e; \quad p_h = n_h k T_h \quad (2.8)$$

Generally speaking, Equations (2.4 – 2.7) are very difficult to solve numerically. However, it will be shown in Chapter 4 that for the studies concerned in this thesis, all four equations can be greatly simplified. For example, the axial component (along the axis \hat{z}) of Equation (2.4) reduces to the Ohm's Law and its radial component is eliminated by taking advantage of gas dynamic model calculations. It is important to realize that the validity of the simplifications introduced in Chapter 4 has only been verified for the study of subsequent return strokes with commonly observed characteristics. For the study of other lightning processes, or for more extreme cases of return strokes (e.g., peak return stroke current higher than 100 kA), the equations presented in this section should be reexamined to derive the appropriate simplifications. In particular, some of the simplifications made in Chapter 4 may not apply to the study of dart leader process.

2.3.2 The boundary of the core

The boundary of the core is the region across which the plasma state transitions from a highly ionized plasma to a weakly ionized plasma and eventually to SATP (standard ambient temperature and pressure). For several reasons the physics of this region is much more complicated than that of the bulk of the core.

As the density of charged particles decreases by many order of magnitudes across the boundary region, the rate of coulomb collisions between charged particles and the rate of collisions between charged particles and neutral particles are reduced at least by the same order of magnitude. One important consequence of the low collision rate is that the energy distribution of the charged particles is no longer Maxwellian, but becomes directly dependent on the electric and magnetic field. Another important consequence of the low collision rate is that the heavy particle excited and ionized electronic energy states are no longer at thermal equilibrium with the electron gas. That is, an explicit treatment is required for the finite rate of heavy particle excitation and ionization due to electron impact and photo-ionization; e.g., the ionization rate by electron impact is directly dependent of the electric field strength. It is also necessary to include the finite rate of photo-ionization, which is due to the optical radiation from the bulk of the core [*Zel'dovich and Raizer, 2002, Ch. 5, p. 283–303*].

The situation is further complicated by the initiation of streamers near or at the boundary of the core. At many stages of a lightning flash, the charges accumulated in the core are strong enough to cause electric breakdown of the air near the core and thus initiate streamers propagating outwards in the lateral direction. Accurate treatment of the initiation and propagation of the numerous streamers, as well as their effects on the plasma state of the boundary region of the core is well beyond what modern computational resources can handle.

In summary, accurate treatment of the boundary region of the core raises many questions that are both theoretically and computationally challenging. For the studies presented in this thesis, the model is greatly simplified to avoid these complexities. As further elaborated in Chapter 4, these simplifications are based on both observations and theoretical

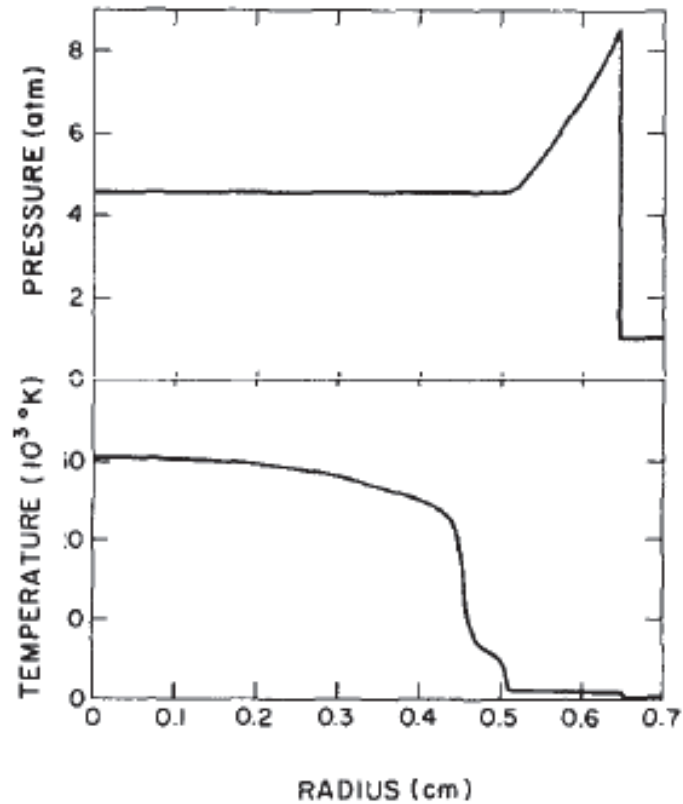


Figure 2.3: The radial distribution of channel thermodynamic properties [Plooster, 1971a].

calculations which suggest that the leader channel has a well-defined narrow boundary region (Figure 2.3). More specifically, the radial distribution of the free electron density is approximately uniform in the bulk of the core and then falls rapidly by many order of magnitudes over a distance much less than the bulk radius. In the rest of this section, we briefly discuss equations that one may consider for a more accurate treatment of the boundary region.

Because of the finite rate of heavy particle excitation and ionization in the boundary regions, it is no longer appropriate to treat the different types of heavy particles (O, O⁺, N, N⁺...) as a single species. One must keep track of the particle densities of the different heavy particle species separately by using the following set of equations, where “*i*” and “*j*” denote the various particle species. The equations are:

(1) Continuity equations

$$\frac{\partial n_i}{\partial t} + \nabla \cdot (n_i \mathbf{U}_i) = w_i \quad (2.9)$$

(2) Momentum conservation equations

$$n_i m_i \frac{D\mathbf{U}_i}{Dt} = -\nabla p_i + \nabla \cdot \boldsymbol{\tau}_i + q_i n_i \mathbf{E} + \mathbf{J}_i \times \mathbf{B} - \sum_{j \neq i} n_i m_{ij} \nu_{ij} (\mathbf{U}_i - \mathbf{U}_j) - m_i \mathbf{U}_i w_i \quad (2.10)$$

(3) Energy conservation equations

$$\frac{\partial n_i \epsilon_i}{\partial t} + \nabla \cdot (N_i \mathbf{U}_i \epsilon_i) = \nabla \cdot (\kappa_i \nabla T_i) - \nabla \cdot (\mathbf{U}_i \cdot p_i) + \mathbf{J}_i \cdot \mathbf{E} + (P_{\text{col}}^{\text{elas}})_i + (P_{\text{opt}}^{\text{tot}})_i \quad (2.11)$$

(4) State equations

$$p_i = n_i k T_i \quad (2.12)$$

In these equations, n_i is the particle density, \mathbf{U}_i the bulk average velocity; w_i the total rate of the different ionization mechanisms D/Dt is the substantial derivative; m_i the mass of a single particle; p_i the bulk pressure; $\boldsymbol{\tau}_i$ the shear stress tensor; q_i the electric charge of a single particle; \mathbf{E} the electric field; \mathbf{J}_i the current density and ν_{ij} the collision frequency between species “ i ” and “ j ”; $(P_{\text{col}}^{\text{elas}})_i$ is the elastic collision energy transfer between the particles of species “ i ” and of all the other species; $(P_{\text{col}}^{\text{tot}})_i$ is the energy transfer between the particles of species “ i ” and the optical radiation field. Both the term $(P_{\text{opt}}^{\text{tot}})_i$ and the contribution of the photo-ionization to w_i require the solution to the radiation transport equation in order to resolve the optical radiation field variations in the boundary region [Zel’dovich and Raizer, 2002, Ch. 2, p. 128–130].

2.3.3 The sheath

Both the experimental observations and the theoretical studies of the sheath are still in their early stages. In particular, a very limited understanding is available for the construction of a physically accurate sheath model for the fast dynamics during the return stroke. In this section, we limit our discussion to certain aspects of the sheath physics that we relied upon for the construction of an empirical model in the studies presented in the following chapters.

Due to the high electrical conductivity in the bulk of the core, nonzero charge density tends to distribute on its boundary. With sufficient charge accumulated, the electric field near the core becomes strong enough to induce air breakdown, which in turn leads to streamer processes that carry the excess charge away from the boundary. Thus, the charge balance in the boundary region is determined by the rate of accumulation due to the current in the bulk and the rate at which the charge is carried away by streamers into the sheath region. The small radial dimension of the core means that a small nonzero charge in the boundary is sufficient to induce air breakdown and create streamers. For the same reason, it is the sheath region, rather than the core, that carries most of the charge deposited along the channel by stepped leaders.

In the sheath region, the air temperature and pressure are much lower and are close to the ambient air conditions. The ionization in the sheath region is caused by numerous streamers that are initiated near the boundary of the core and propagate outwards, leaving behind filamentary conductive channels. Because of the low sheath air temperature, free electrons in these channels quickly attach to heavy particles, resulting in charged particles of much lower mobility. As a result, the sheath plasma is far from thermal equilibrium and its dynamics is distinctly different from both the boundary region and the bulk of the core.

Charge transfer between the sheath and the core takes place as a result of the propagating streamers and the current in the low-conductivity medium. The current induced by a streamer is determined by the amount of charge it carries and the speed it propagates, both of which are functions of the electric field and the air density. To determine the total rate of charge carried into the sheath region, the frequency at which streamers are initiated also needs to be determined. While some basic theories about the charge carried by a streamer and its propagation speed can be found in *Bazelyan and Raizer* [1997, Ch. 5, p. 151–155], the initiation frequency, especially during some of the fast lightning processes such as the return stroke, is poorly understood. Moreover, the collective behavior of the streamers in the sheath is essentially unknown.

2.4 Lightning channel development (+ and - leader)

In this section, we provide a phenomenological description for several forms of streamer-leader transitions that underlie the creation and the growth of the lightning channel. Much of the description is inferred from laboratory studies of long sparks rather than from observations of lightning flashes. The reason we rely on laboratory data is because currently available experimental techniques for lightning observation do not possess enough temporal and spatial resolution to resolve these processes. However, as the observations are gradually improved, more evidence arises in support of the description presented in this section. While the phenomenological description and the final results of most of these transition processes are clear, the underlying physics of these transition processes is not well understood. Most importantly, as mentioned briefly in Section 2.2, the heating by the current of a single streamer is far from sufficient for the heavy particles to reach a high enough temperature for the channel to transit into a leader. Therefore, in the case of a positive leader, there must be a mechanism for the accumulation of currents from numerous streamers within a region of small radius inside the leader head so that this region can be sufficiently heated to become a part of the leader. Unfortunately, there is very little detailed discussion in the literature on this type of mechanism. Consequently, empirical models that are based on the phenomenological description are needed whenever the creation of the leader need to be included in a model.

2.4.1 Positive leader

In laboratory long spark experiments, a positive leader initiates from the anode and carries a positive charge along at its head. The three components of a positive leader that appear in a continuous streak photography performed by an electro-optical image converter are the channel, the head, and the streamer zone (Figure 2.4). Because the leader is highly conductive, the external field leads to charge accumulation at the head, producing a strong electric field in the region near the tip. As a result, streamers initiate at the head and carry charge away from the tip to form the streamer zone. The channel primarily emits visible light, while the streamer zone emits in the near-ultraviolet region. The head is the brightest structure in a streak photo, and its tilt is used to measure the leader velocity. High speed

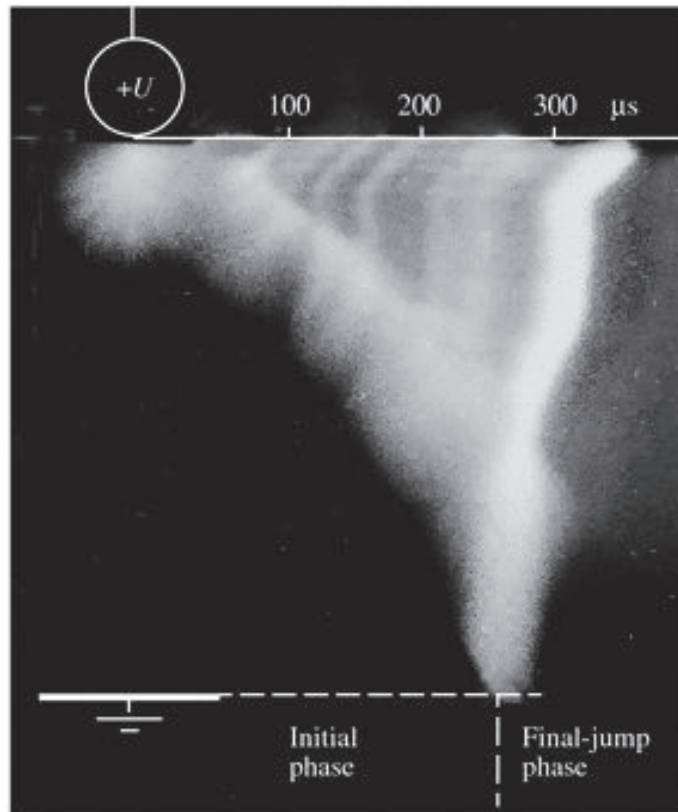


Figure 2.4: Streak image of a positive leader developing in a 8 m air gap [Ivanovskii, 2000].

camera with a good spatial resolution shows that a positive leader propagates by means of consecutive flashes, each of which extends the leader by a length of the order its head radius. The sheath region, sometimes called the charge cover, is also present around the channel but indistinguishable in a streak photo. Part of the charge in the sheath region comes from the streamer zone. In other words, as the leader propagates, its head moves through the streamer zone and so does the region of streamer inception and the boundary of streamer zone. The streamer zone created earlier is left behind and its charge becomes part of the charge in the sheath region. The sheath charge varies over time as charge redistributes on the leader channel surface, which causes new streamers to initiate and carry charge from the channel to the sheath in lateral direction.

Experimental data on charges in the streamer zone and in the sheath are very scarce. Even less well documented is the variation in the charge distribution as a function of time.

This lack of data and theoretical understanding severely limits the possibility of a physically accurate model of these processes.

2.4.2 Negative leader, space stem

In laboratory long spark experiments, a negative leader initiates from the cathode and carries a negative charge at its head. Once the leader channel is created, its properties are essentially the same as those of a positive leader channel. A negative leader differs from a positive leader primarily by the processes in the streamer zone and therefore by the characteristics of the movement of the channel front section.

The streamer zone formation in a negative leader requires higher voltage than in a positive leader. The reason for a higher voltage is the fact that an electron involved in the avalanche ionization in the streamer process, in the case of a negative leader, is driven away from the leader head and thus the avalanche develops in a weaker field. On the other hand, in the case of a positive leader, an electron is driven towards the leader head and thus the avalanche develops in a stronger field.

As shown in Figure 2.5 and discussed in detail in *Biagi et al.* [2010], the streamer zone structure and the leader channel formation mechanism of a negative leader are both significantly more complicated than those of a positive leader. One of the most noticeable features of negative leader channel formation is the presence of a space stem in front of the main channel. In other words, as the main channel of the leader extends, a small segment of the leader channel which is separated from the main channel emerges in the front of the main channel and extends in both directions. This separated leader segment eventually connects with the main channel and initiates a current pulse in the channel. This current pulse causes rapid heating and thus leads to temporary brightening of the channel. As a result, the channel appears in the streak photo as if it suddenly stepped forward. Hence the name negative stepped leader.

2.4.3 Lightning initiation

Among the various lightning initiation mechanisms are initiation inside the cloud, from flying objects (aircrafts, rockets), and ground protruding objects (towers, trees, buildings).

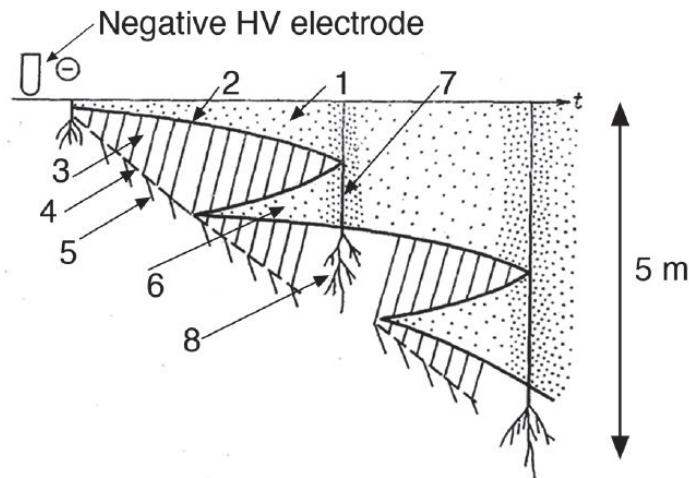


Figure 2.5: Negative leader: (1) primary leader channel, (2) leader tip, (3) positive streamers, (4) space stem, (5) negative streamers, (6) thermalized space stem, which becomes a space leader, (7) space leader connects with the primary leader [Biagi *et al.*, 2010, Gorin *et al.*, 1976].

Nevertheless, the majority of naturally occurring lightning are initiated inside the cloud. The mechanism of lightning initiation inside the cloud is different from processes associated with positive or negative leader, and laboratory long spark initiation from a small electrode. This difference is due to the fact that a lightning channel does not yet exist and thus there is no charge accumulation at the channel tip to create a strong electric field. Another difficulty arises from the fact that both in situ and remote measurements show that the maximum values of the large-spatial-scale electric fields in thunderclouds are insufficient for streamer initiation.

A viable theory of the lightning initiation inside the cloud must provide a mechanism for the streamer initiation and for the transition from streamers to leaders. Generally speaking, lightning initiation remains a challenging problem and is still a subject of active research.

2.4.4 Attachment

The attachment process is one of the least documented and least understood lightning processes. Moreover, the final stage during which the laboratory long spark bridges the air gap may not be applicable to lightning, because the lightning attachment process often involves

the initiation of an upward propagating channel from a protruding conductive object on the ground, and then, when the streamer zones of the upward and downward propagating channels meet, a new channel segment is created to connect the two channels. The creation process of this connecting channel segment may be different from the positive and negative leaders, because of the presence of the streamer zone of the opposite sign. In summary, the attachment process is still poorly understood and the development of a physically accurate model for this process is still a matter of future research.

Chapter 3

Numerical Techniques

Because of the thermodynamics of the core and the core-sheath interaction, the system of equations governing the dynamics of the lightning channel is highly nonlinear. If the full set of equations are solved together, it would be necessary to deal with the high degree of nonlinearity for a large number of variables. Instead, the computation within each time step is carried out in several stages, as shown in Figure 3.1.

The electrodynamics of the core refers to the temporal and spatial evolution of the charge and current distribution in the core. The thermodynamics of the core refers to the temporal and spatial evolution of thermodynamic properties (e.g., temperature, pressure), transport properties (e.g., electrical and thermal conductivities) and various forms of energy (e.g., optical radiation, internal energy variation). The sheath dynamics includes both the charge transfer between the core and sheath and the temporal and spatial variation of the charge distributions in the sheath.

At the first stage, the current and charge distributions in the core are updated, while the thermodynamic properties are kept constant and the core-sheath charge transfer rate is kept equal to that at the previous time step. As discussed in Section 3.1, the equations that need to be solved at this stage are linear and can be solved using well-established methods. For both the second and the third stages, the charge and current distributions in the core become an input. At stage two, the system of equations governing the thermodynamics of the core, especially Equations (2.4–2.7), are highly nonlinear and generally difficult to solve. For the studies presented in this thesis, these equations are greatly simplified based

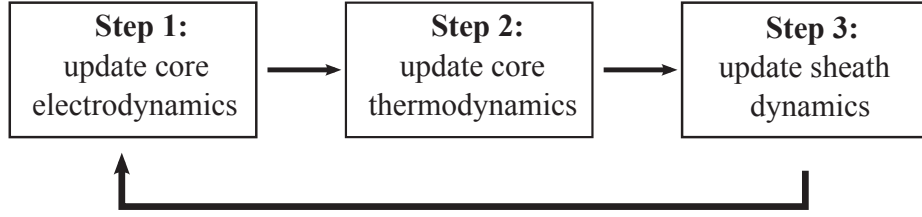


Figure 3.1: The computation flow

on our knowledge of the time and spatial scale of the phenomena under consideration. The resulting equations are simple enough to be solved by using well-established methods. At stage three, the core-sheath charge transfer and the sheath charge distribution is updated using an explicit scheme. The second and third stages are interchangeable, because as far as the models presented in this thesis are concerned, the thermodynamics of the core is decoupled from the sheath dynamics.

The validity of the assumption of steady-state core thermodynamics and constant sheath quantities during step 1 is justified by the difference of relevant time scales. As discussed in Chapter 4, a time step of the order of a few ns is normally used to fully resolve the electrodynamics of the core. On the other hand, both the thermodynamic properties of the core and the charge distribution in the sheath only vary significantly over time scales of the order of $10 \mu\text{s}$.

In the following two sections, we describe the numerical techniques used in the first two stages, for the solution of equations after simplification. The update for the sheath using Equation (4.4) is straightforward.

3.1 Electrodynamics of the core

At stage one, with the thermodynamic properties kept constant and the core-sheath charge transfer rate kept equal to its value at the previous time step, Equations (2.1), (2.4) and (2.5) need to be solved to update the current and charge distributions in the core. As will be discussed in Chapter 4, both the radial component and the axial component of Equations (2.4) and (2.5) can be greatly simplified. More specifically, the radial components of the equations no longer need to be explicitly solved in the first stage. Instead, the radial

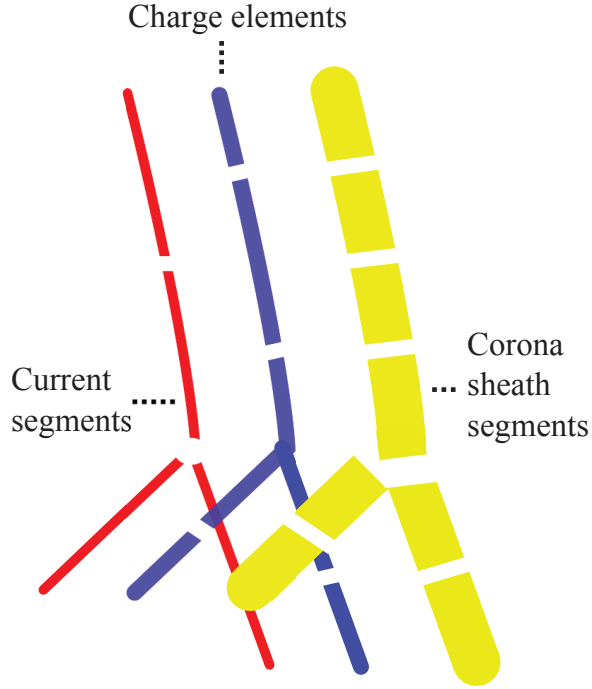


Figure 3.2: The discretization of lightning channel

component of the core current is determined by the charge variation on the boundary of the core and the charge transfer rate between the core and the sheath. The axial components of the equations are reduced to Ohm's Law; in other words, we have

$$\sigma_e(T_e, T_h, p_e, p_h)\mathbf{E}(\mathbf{x}, t) = \mathbf{j}(\mathbf{x}, t) \quad (3.1)$$

where σ_e is the electrical conductivity. The conductivity σ_e is uniquely determined by T_e, T_h, p_e and p_h because of the assumption that heavy particle excitation and ionization are at thermal equilibrium with the electron gas at T_e .

In other words, only Equations (2.1) and (3.1) need to be solved to update the charge and current distributions in the core. For this solution, we use the time-domain Method of Moments (MoM). Below, we describe the discretization of the lightning channel (Figure 3.2) and then explain the basic idea of time-domain MoM.

The core is divided into straight cylindrical segments, from here on called the current segments, with the height of a particular segment specified as L_{cur} and the axial component

of the core current density, j^z , assumed to be uniform (both in the axial direction and in the radial direction) within each segment. It is then possible to introduce I_{core} , the total current that flows along the core, to uniquely specify the axial component of the core current density:

$$j^z = \frac{I_{\text{core}}}{\pi r_{\text{core}}^2}$$

The charge elements are formed from the halves of adjacent current segments. Hence the number of halves of current segments in each charge element equals the number of current segments whose current flows in or out of the charge element. The charge in a charge element is assumed to be uniformly distributed among all of its half current segments. It is further assumed that the charge within each of the half current segment is uniformly distributed on the boundary of the core (for the purpose of calculating \mathbf{E} using EFIE). It is then possible to define λ_{core} , the linear charge density of the core, to uniquely specify the charge distribution in each charge element. The sheath segments are discretized to match the half segments in the charge elements. The charge is assumed to be uniformly distributed within each sheath segment.

The time variation of λ_{core} for a charge element is related to the currents that flow in and out of the element by the charge conservation. For example, consider the i th charge element and use Ω^i to denote the set of current segments whose current flow in or out of the charge element. The number of segments in Ω^i is denoted by N_i . Note that the number of half segments in the charge element is also N_i .

$$\frac{N_i L_{\text{cur}}}{2} \frac{d\lambda_{\text{core}}^i}{dt} = \sum_{j \in \Omega^i} \text{sign}(j) I_{\text{core}}^j \quad (3.2)$$

where j indexes the current segments that flow in or out the i th charge element and $\text{sign}(j)$ is a function that is positive (negative) if the current of the j th segment flow into (out of) the charge element.

In the time domain, the current derivative dI_{core}/dt is taken as constant within each time step. It then follows that the I_{core} varies linearly and λ_{core} varies quadratically within each time step.

To find the electric field at any point in space \mathbf{x} and time t , we start with the EFIE Equation (2.1), restated below for convenience:

$$\mathbf{E}(\mathbf{x}, t) = \frac{1}{4\pi\epsilon_0} \int d^3\mathbf{x}' \left\{ \frac{\hat{\mathbf{R}}}{|\mathbf{R}|^2} [\rho(\mathbf{x}', t')]_{\text{ret}} + \frac{\hat{\mathbf{R}}}{c|\mathbf{R}|} \left[\frac{\partial\rho(\mathbf{x}', t')}{\partial t'} \right]_{\text{ret}} - \frac{1}{c^2|\mathbf{R}|} \left[\frac{\partial\mathbf{j}(\mathbf{x}', t')}{\partial t'} \right]_{\text{ret}} \right\}$$

Note that depending on the distance between \mathbf{x}' and \mathbf{x} , the integration may involve values of ρ , \mathbf{j} at any retarded time t' that is less than t . Integrating over each current segment and charge element, the integral over space is reduced to the sum:

$$4\pi\epsilon_0\mathbf{E}(\mathbf{x}, N\delta t) = \sum_i \int d^3\mathbf{x}' \left(\frac{\hat{\mathbf{R}}}{|\mathbf{R}|^2} [\rho(\mathbf{x}', t')]_{\text{ret}} + \frac{\hat{\mathbf{R}}}{c|\mathbf{R}|} \left[\frac{\partial\rho(\mathbf{x}', t')}{\partial t'} \right]_{\text{ret}} \right) - \sum_k \int d^3\mathbf{x}' \frac{1}{c^2|\mathbf{R}|} \left[\frac{\partial\mathbf{j}(\mathbf{x}', t')}{\partial t'} \right]_{\text{ret}} \quad (3.3)$$

The time t is replaced by $N\delta t$, where δt is the time step. Equation (3.3) hence evaluates the electric field at \mathbf{x} at the N th time step, where i iterates through all the charge elements and k through all the current segments. Note that the integration over sheath segments is not shown in the equation above for clarity but should be included in the actual model. Each of the integrations under the summation sign is restricted to the region of a specific current segment or charge element. Each of these integrations can then be re-expressed in terms of I_{core} and λ_{core} multiplied by a geometrical factor. For example, consider the last term on the right of the equation above for the k th current segment. For the sake of simplicity, we further assume the time delay between \mathbf{x} and any point \mathbf{x}' in the k th current segment to fall in the same time step. That is, for all \mathbf{x}' in the k th current segment, $l\delta t \leq \frac{|\mathbf{x}-\mathbf{x}'|}{c} \leq (l+1)\delta t$ for some integer $l \geq 0$, where c is the speed of light. Then

$$\begin{aligned} \int_{\mathbf{x}' \in k} \frac{1}{c^2|\mathbf{R}|} \left[\frac{\partial\mathbf{j}(\mathbf{x}', t')}{\partial t'} \right]_{\text{ret}} &= \frac{1}{\pi(r_{\text{core}}^k)^2} \left(\int_{\mathbf{x}' \in k} \frac{1}{c^2|\mathbf{R}|} \right) \frac{\partial I_{\text{core}}^{k, N-l}}{\partial t'} \\ &= (\text{GeometricalFactor}) \times \frac{\partial I_{\text{core}}^{k, N-l}}{\partial t'} \end{aligned}$$

where “ $\mathbf{x}' \in k$ ” means that \mathbf{x}' lies in the spatial region spanned by the k th current segment; and $I_{\text{core}}^{k, N-l}$ denotes the current in the k th current segment at $(N-l)$ th time step. Generally,

it is incorrect to assume that the time delay between \mathbf{x} and any point \mathbf{x}' in the k th current segment falls in the same time step. In this case, the integration over a current segment can be split into a summation of a few terms of the above form. The other terms of Equation (3.3) can be represented by similar forms. The geometrical factors can be pre-calculated and stored before the simulation starts. Furthermore, when \mathbf{x}' is far from \mathbf{x} , far field approximation can be used to simplify the integration.

Finally, note that by using Equation (3.2), the terms involving λ_{core} can be re-expressed in terms of $\partial I_{\text{core}}/\partial t$, I_{core} and λ_{core} from earlier time steps. Thus, after the $(N - 1)$ th time step in a simulation is completed, in order to calculate the electric field at the N th time step, the only unknowns in Equation (3.3) are the derivatives $\partial I_{\text{core}}/\partial t$ for every current segment during the time period $t \in [N - 1, N]\delta t$.

To close the system of equations, MoM makes use of a set of “test functions” (defined in *Gibson* [2008, Ch. 3, p. 43]), which are used to evaluate \mathbf{E} in each current segment in order to calculate the current using Ohm’s Law. In our case, system of equations are closed by taking integration of \mathbf{E} at $t = N\delta t$ over each current segment k and by ensuring that Ohm’s Law is satisfied. That is, for every current segment k ,

$$\int_{\mathbf{x} \in k} \mathbf{E}(x, N\delta t) d^3 \mathbf{x} = \pi (r_{\text{core}})^2 L_{\text{cur}} \sigma_e^{-1} I_{\text{core}}^{k,N} \quad (3.4)$$

where the integration is taken over the entire region spanned by the k th segment, $I_{\text{core}}^{k,N}$ denotes the current in the k th current segment at the N th time step and L_{cur} denotes the length of the k th current segment. Substitution of Equation (3.3) into Equation (3.4) to eliminate \mathbf{E} results in a set of equations that only involve $\partial I_{\text{core}}/\partial t$, with the unknowns being the values of $\partial I_{\text{core}}/\partial t$ at the last time step only. The number of equations constructed this way equals to the number of current segments and thus is equal to the number of unknowns. This system of equations are thus suitable for solution by an implicit scheme for the time advancement of $\partial I_{\text{core}}/\partial t$ and can then be solved by using well-established procedures.

MoM is a widely used numerical technique in antenna theory, where the electric conductivity of the metal rods is commonly assumed to be infinite and the current only exists

on the surface of the channel. The “test function” is then chosen to ensure that the tangential component of the electric field on the surface of the metal wire to zero [Miller *et al.*, 1973].

One of the key advantages of the MoM formulation is that only the channel region needs to be discretized and included in the computational domain, instead of discretizing the much larger space around the channel which is the approach used, e.g., in FDTD (finite-difference-time-domain) method. This advantage comes about because EFIE already takes into account of the propagation in free space of the electromagnetic waves due to the current and charge source in the channel. Another significant advantage of this formulation is the simplicity of adjusting the mesh for different geometries of the lightning channel, as it is completely free of a fixed background numerical grid.

We now consider a few generalizations of this scheme for future studies. In the study presented in this thesis, the axial component of the core current is assumed to be uniform in the radial direction, in correspondence with the assumption of uniform thermodynamic properties inside the core (Chapter 4). For the more general case in which the radial dynamics of the core is also considered, the radial distribution of the axial component of the core current can be assumed to be proportional to the radial distribution of the electric conductivity, as in *Plooster* [1971a]. This assumption is equivalent to assuming that the skin effect is insignificant (i.e., skin depth is larger than the core radius). For the frequency range that is considered in the studies presented in this thesis, this assumption is valid as a first order approximation. For example, the subsequent return stroke current normally has a rise time of the order of $1 \mu\text{s}$ and a conductivity of the order of 10^4 S m^{-1} , which corresponds to a skin depth $\simeq 0.5 \text{ cm}$ ($\simeq r_{\text{core}}$). In general, it is necessary to verify this assumption by considering the wave modes in a thin conductive cylinder.

The discretization of the lightning channel introduced in Figure 3.2 is sufficient for the studies presented in this thesis, because the radial dynamics of the core is greatly simplified. In the case when a more accurate treatment of the radial dynamics of the core is needed, the core current segments need to be further discretized in the radial direction. This discretization is particularly important for simulating the time evolution of the radial distribution of the thermodynamic properties.

Finally, this discretization is based on the assumption that the variation in the thermodynamic properties of the core in the radial direction is much steeper than the variation in the axial direction. This assumption is true for most parts of the channel, but caution is needed when it comes to the leader tips, such as the dart leader front and step leader tips.

3.2 Thermodynamics of the core

Even with the current and charge distributions in the core being calculated at stage one, it remains extremely challenging to solve Equations (2.2–2.8), plus the radiation transport equations for optical radiation for the thermodynamics of the core. The difficulties are caused both by the high degree of nonlinearity and the large number of variables. The full solution of such a system is beyond the scope of this thesis. In the following chapters, several levels of simplifications are made to the equations to accommodate the scales and objectives of the study.

The return stroke study presented in Chapter 4 features a relatively detailed treatment of the thermodynamics. It is shown that for return stroke study, the axial components of the electron gas and heavy particle gas momentum equations can be reduced to Ohm’s Law, thus justifying Equation (3.4). Moreover, the various forms of energy transfer along the core are shown to be negligible in comparison with the energy transfer in the radial direction. As a result, only the radial dynamics of the core need to be considered. With several further simplifications, the problem can be reduced to what is studied by gas dynamic models [Rakov and Uman, 1998], which normally assume that the channel properties are uniform in the axial direction. That is, the thermodynamics of the core at different locations can be calculated independently of each other. Instead of solving the hydrodynamic equations as in gas dynamic models, we take advantage of their simulation results and make further simplifications. Finally, the problem is reduced to solving, for each current segment, a set of nonlinear ordinary differential equations which involve only a small number of variables.

Newton’s method is sufficient for this type of computation. Furthermore, these equations are solved independently for each current segment, and thus are easily parallelizable.

Finally, several terms in these equations, such as the specific heat, particle density and optical radiation, are highly nonlinear functions of the temperature, pressure and radius of the core and are very computationally expensive to calculate. These quantities are precalculated for a wide range of temperature, pressure and radius of the core and are stored in tabulated or interpolated form.

For models that attempt to treat the radial dynamics of the core more accurately, the magnetic field is required by Equations (2.4) and (2.5). The magnetic field is particularly important for return strokes with a very high peak current, as the induced magnetic pressure is very high and can have a significant effect on the radial dynamic of the core. In this case, the Magnetic Field Integral Equation (MFIE) [*Jackson*, 1999, Ch. 6, p. 246–248] also needs to be included and treated similarly as the EFIE.

Chapter 4

Return stroke study

Although many physical principles discussed in this chapter are applicable to lightning channels of inter-cloud, intra-cloud, and various forms of cloud-to-ground lightning, we will focus our attention on the negative cloud to ground lightning, primarily because it is the most experimentally well-studied form of lightning. For this kind of lightning, a return stroke is initiated once the lightning channel created either by the downward stepped leader or by the dart leader reaches ground. A current wave I_{core} , launched at the ground, travels upward along the core, neutralizing the corona sheath charge and causing rapid heating in the core which brings the core temperature to well above 20 kK. The rapidly rising core temperature leads to intense optical radiation and significant thermal expansion in the core. As a result of the optical radiation, the current wave is accompanied by a luminous region of the channel extending upward (hereafter referred to as the "optical radiation wave"). The thermal expansion leads to a shock wave propagating away from the core, which is the origin of thunder that accompanies lightning flashes.

In comparison with other stages of the lightning flash, the return stroke is particularly convenient to study, both because of its relatively simple physics and the abundance in the quantity and variety of the available experimental data. The simplicity is due to the fact that before the return stroke, the lightning channel had already been created by either a step leader or a dart leader. Hence, it is no longer necessary to deal with the poorly understood leader creation process in the model.

Optical observation systems including still camera, streak camera and photoelectric

diodes provide description of the geometry and the spatial and temporal evolution of the luminous profile of the lightning channel. Optical spectrum observations provide information on the channel thermodynamic properties. Multiple station electromagnetic field recordings provide data on the RF radiation associated with the return stroke current. There are also recordings of the return stroke current at the ground. Our purpose is to create a multi-physics model which allows comparisons with all the different experimental data.

One aspect of a return stroke that is of special interest is the return stroke speed. A series of observations report the speed of extension of the luminous region, i.e., the optical radiation wave speed, v_{opt} , to be between $\frac{1}{5}$ and $\frac{2}{3}$ of the speed of light c [Idone and Orville, 1982, Mach and Rust, 1989, Weidman, 1998, Wang *et al.*, 1999, Rakov, 2007, Idone *et al.*, 1984, Hubert and Mouget, 1981]. On the other hand, direct measurements of the current wave and its propagation speed v_{cur} are not available. Existing gas-dynamic models cannot be used for this purpose. Such models apply predefined return stroke current to study the radial dynamics of the core [Rakov and Uman, 1998]. These models focus on a small segment of the core and solve hydrodynamic equations assuming translational symmetry along the core. Consequently, they are not suitable for the study of v_{opt} or v_{cur} . Several electromagnetic models calculate I_{core} as a function of both location along the core z , and time t , i.e., $I_{\text{core}}(z, t)$ [Rakov and Uman, 1998]. However, these models do not explicitly treat the thermodynamic aspect of the physics and thus cannot establish a quantitative connection between $I_{\text{core}}(z, t)$ and the optical radiation power $P_{\text{opt}}(z, t)$. In this chapter, we present a model that uses realistic high temperature air plasma thermodynamic properties together with self-consistent solutions of Maxwell's equations coupled with equations for the dynamics of a high temperature air plasma.

In Section 4.1, we first discuss in detail several simplifications to the equations for the core and present an empirical model for the sheath. These simplifications are made possible by several factors including the fact that the core plasma is highly collisional, and the dramatically different time scales in the radial and the axial direction. In Sections 4.2.1 to 4.2.3, we first present the result of a single simulation using a specific set of parameter values, then investigate the difficulties in the definition of v_{cur} by examining the variations in v_{cur} merely as a result of the choice of the definition in theoretical modeling (or measuring technique in experimental studies), and finally discuss the implications of the model

predictions on the calculated electromagnetic radiations by the return stroke current and its impact on applications such as lightning geo-location and lightning-upper-atmosphere coupling. In Sections 4.2.4 to 4.2.7, we examine more carefully how the simulation results vary with model parameter values and conditions. Because some of the simplifications made during the construction of the model introduce quantitative errors into the model, the studies presented in Sections 4.2.4 to 4.2.7 are essential to verify the robustness of the model prediction that v_{cur} is higher than v_{opt} .

4.1 The simplified model

While the discussion in Chapter 2 provides a more general description of the physics of the leader channel, in this section we introduce several simplifications to the equations that govern the models of the sheath and the core. More specifically, the equations discussed in Chapter 2 are generally applicable to the core of a leader channel at any stage of a lightning flash, but are difficult to solve. Fortunately, for the return stroke channel, these equations can be greatly simplified by taking into consideration the temperature and pressure range of concern, the dramatically different time and spatial scales of different aspects of the processes, and the rise time and the peak value of the return stroke current. Regarding the sheath, the current understanding of its physics is insufficient for the construction of a physically accurate model, especially for the fast dynamics of the return stroke. Instead, we make use of an empirical model which is discussed in Section 4.1.2. Finally, in Section 4.1.3 we describe the setup for subsequent return stroke simulation, where the ground recording of the return stroke current is used as an input to the simulation.

4.1.1 The core

This section focuses on the simplifications that can be made to the equations introduced in Chapter 2. First, we discuss qualitatively the return stroke characteristics that the simplifications rely on. Then we list the simplified equations and provide more detailed discussions on the justification for the simplifications for some of the equations.

The temperature and pressure of the return stroke channel exceed 20 kK and 1 atm

respectively when the channel is created by a stepped leader or a dart leader, and are further increased by the Joule heating associated with the the return stroke current. For the entire duration of the return stroke, the air plasma of the core is highly collisional. This collisional state not only justifies the two-gas-component view of the core plasma, but also plays a central role in simplifying the hydrodynamic Equations (2.4–2.7), especially for the axial component of the gas momentum conservation. It is also of interest to point out that, for the temperature and pressure range of concern, the heavy particles are fully dissociated and the electrons are not attached to heavy particles to form negative ions. That is, the heavy particle gas consists only of single atoms such as O, N, O⁺ and N⁺.

Another important characteristic of the return stroke channel is the distinctly different spatial scales of the variation of the thermodynamic properties of the core in the axial and radial directions. To illustrate this, we consider, for both directions, the distances over which the core state variables increase from their initial values to their peak values. In the axial direction, due to the wave nature of the current and optical radiation, this distance can be estimated by multiplying the wave propagation speed along the channel with the rise time from 20% to 80% of the peak at a specific location. According to optical signature observations, the optical wave speed v_{opt} is between $\frac{1}{5}$ and $\frac{2}{3}$ of the speed of light c [*Idone and Orville, 1982, Mach and Rust, 1989, Weidman, 1998, Wang et al., 1999, Rakov, 2007*]. The rise time $\tau_{\text{rise}}^{\text{opt}}$ increases with altitude and is measured to be approximately 1–4 μs [*Wang et al., 1999*]. The rise time for temperature and pressure is $\geq \tau_{\text{rise}}^{\text{opt}}$, because the dependence of optical radiation on temperature is strongly nonlinear and the core becomes optically visible only at temperatures much higher than 20 kK [*Aubrecht and Bartlova, 2009*]. For the current wave, direct measurement of $\tau_{\text{rise}}^{\text{cur}}$ is only available at the ground, which is also on the order of a few μs [*Berger et al., 1975*]. $\tau_{\text{rise}}^{\text{cur}}$ can only increase with altitude because of the dispersion of electromagnetic waves propagating along a thin conducting channel. The current wave speed v_{cur} is expected to be comparable with v_{opt} , because the current wave provides the energy for the heating of the core. In conclusion, the axial distance over which core state variables increase from their initial values to their peak values is on the order of $10^8 \text{ m s}^{-1} \times 1 \mu\text{s} = 100 \text{ m}$.

This spatial scale difference implies that, when a small segment of the core ($\leq 1 \text{ m}$) is considered, it appears nearly translationally symmetric in the axial direction. In other

words, quantitatively, for the radial components of Equations (2.4) to (2.7), the terms involving the spatial gradient in the axial direction (\hat{z}) can be taken as zero, because they are much smaller than their counterparts that involve the spatial gradient in the radial component. Consequently, the radial thermodynamics of the core is governed by a set of equations that are similar to that which is treated by gas dynamic models and thus the simulation results of gas dynamics models can be used to understand the radial dynamics of the core. By taking into account the results of gas dynamic model calculations, the equations that govern the radial dynamics of the core can be further simplified.

In the rest of this section, we describe in greater detail the simplifications that are made to Equations (2.4–2.7), starting with the axial components of Equations (2.4) and (2.5), followed by the axial terms in Equations (2.6) and (2.7), finally the radial components of Equations (2.4) and (2.5), and the radial terms of Equations (2.6) and (2.7).

Firstly, we note that due to the huge mass difference between electrons and heavy particles, the axial component of the core current is by far dominated by electron gas flow, i.e. $U_e^z - U_h^z \simeq U_e^z$ and $j^z \simeq q_e n_e U_e^z$. In the axial component of Equation (2.4), many terms may be neglected. For the temperature and pressure range considered, ν_{eh} is on the order of 10^{11} s^{-1} [D'Angola *et al.*, 2008]. Taking into account of the rise time of return stroke current, the term $m_e(DU_e/Dt)$ is many orders of magnitude smaller than the collision term and may be dropped. Similar consideration of the temperature and pressure rise time shows that w_e , the ionization rate, is also many order of magnitude smaller than ν_{eh} and may also be neglected. Both the bulk pressure and shear terms may be neglected due to the low spatial gradient in axial direction. The treatment of the axial component of $\mathbf{J}_e \times \mathbf{B}$, i.e., $q_e n_e U_e^r B^\phi$ is more complicated. Near the boundary of the core, where both B^ϕ and U_e^r reach their maximum, exclusion of this term can lead to appreciable error in the current density. To see this, we compare the term $U_e^r B^\phi$ with E^z . Given that the return stroke peak current $\mathbf{I}_{\text{core}}^k$ is of the order of 10 kA and r_{core} is on the order of 1 cm, B^ϕ is estimated to be of the order of 1 T from

$$B^\phi = \frac{\mu_0 |\mathbf{I}_{\text{core}}^k|}{2\pi r_{\text{core}}}$$

The electron drift velocity U_e^r is on the order of 10^3 ms^{-1} . For an order of magnitude estimation of E^z , we assume that Equation (3.1) applies. The electric conductivity of the

core σ_e is on the order of 10^4 Sm^{-1} and in order to have current $|\mathbf{I}_{\text{core}}^k| \sim 10 \text{ kA}$ through a core of radius $r_{\text{core}} \sim 1 \text{ cm}$, E^z must be of the order of 10^4 Vm^{-1} . That is, E^z is only one order of magnitude higher than $U_e^r B^\phi$. However, both B^ϕ and U_e^r decrease approximately linearly and therefore $U_e^r B^\phi$ decreases quadratically towards the center of the core and reaches zero at the center. On the other hand, E^z stays approximately constant. As a result, the term $U_e^r B^\phi \ll E^z$ when averaged over the core cross section. This term is thus set to zero for the simulations presented here. However, note that in the case of very high return stroke current ($\sim 100 \text{ kA}$), it may be necessary to include this term.

With $q_e n_e U_e^r B^\phi$ also neglected, we finally obtain the following equation:

$$0 = q_e n_e E^z - n_e m_{\text{eh}} \nu_{\text{eh}} U_e^z;$$

A similar arguments can be made for the axial component of Equation (2.5). However, as mentioned above, due to the much larger mass of heavy particles, their contribution to the total current is negligible. With these considerations, we finally obtain the Ohm's Law, with electric conductivity σ_e defined only by the electron gas:

$$j^z = E^z \sigma_e; \quad \sigma_e = \frac{q_e^2 n_e}{m_{\text{eh}} \nu_{\text{eh}}}$$

Note that for the radial components of the momentum equations of the two gases, many of the simplifications above do not apply. It is in general necessary to solve the momentum equation in the radial direction with most of its terms present, as is done in gas dynamic models [Plooster, 1971a, Hill, 1977, Paxton et al., 1986].

In energy conservation Equations (2.6) and (2.7), the terms such as $\nabla \cdot (n_{e,h} \mathbf{U}_{e,h} \epsilon_{e,h})$, $\nabla \cdot (\kappa_{e,h} \nabla T_{e,h})$, $\nabla \cdot (\mathbf{U}_{e,h} \cdot p_{e,h})$ and $P_{\text{opt}}^{\text{tot}}$ correspond to the heat transfer due to the particle density, temperature, pressure and optical radiation intensity gradients in the axial and radial directions. Considering the huge difference in the axial and radial gradients (as discussed at the beginning of this section), the axial components of the above terms are expected to be smaller than their radial counterparts. As a result, the energy equations may be simplified to include only the radial gradients for a first order treatment. Note that in other cases such as the dart leader or stepped leader, the axial gradients near the tip can be comparable to their radial counterparts and thus cannot be eliminated from the equations.

Many of the terms in the radial components of momentum conservation Equations (2.4) and (2.5), and the remaining terms in Equations (2.6) and (2.7) after the above simplifications, cannot be eliminated using the same arguments as for the axial components. Strictly speaking, in order to resolve the radial dynamics of the core, it is necessary to solve those equations, coupled with the radiation transport equations for optical radiation field [Paxton *et al.*, 1986]. These computations are computationally very expensive, even for a small segment of the channel. For the return stroke channel, it would be necessary to solve these equations repeatedly for each small segment of the channel. More complications come from the boundary region. As discussed in Chapter 2, in the boundary region the ionization and excitation may not be at equilibrium at T_e and it becomes necessary to explicitly include the ionization and excitation rates of the various processes including photon ionization and electron impact ionization. A further complication arises from the fact that the interaction between the boundary and the sheath regions is still not well understood as mentioned in Section 2.3.3. Simplification is thus inevitable, even at the cost of the model accuracy.

To simplify the radial dynamics of the core, we take advantage of the gas dynamic model calculation results. In particular, the core expansion speed is estimated to be on the order of 10^3 ms^{-1} [Paxton *et al.*, 1986]. Given that the initial radial dimension of the core is approximately 1 cm, this speed implies that the core expansion appreciably modifies the channel electromagnetic properties, such as its conductivity, effective capacitance and inductance, only on a time scale $\geq \mu\text{s}$. For this reason, the core expansion should have little effect on the speed of the current and optical waves. Thus, in the most basic set up, the radial expansion which is due to both the gas expansion and the increasing ionization in the boundary region is neglected. The gas dynamic model calculations also show that starting from the center, n_e varies slowly at first in the radial direction and then decreases rapidly over a very short distance, which may be considered the sharp boundary of the core, at radius r_{core} [Paxton *et al.*, 1986, Hill, 1977]. Thus, the conducting portion of the core may be represented by a core radius r_{core} . The bulk of the core is defined as the region bounded by r_{core} and the boundary is assumed to be infinitely thin. Note that r_{core} is likely to be smaller than the estimated optical width of the core based on optical observations. The same gas dynamic model calculations show that the temperature and pressure are nearly

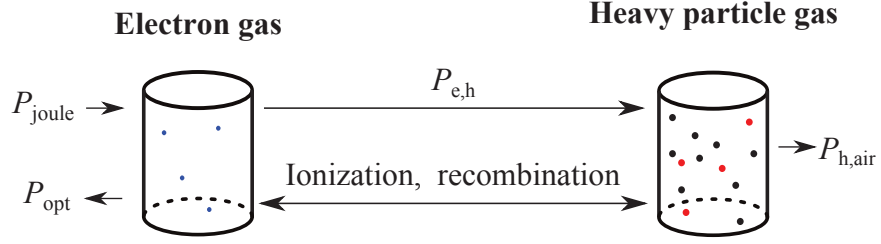


Figure 4.1: Energy input/output for the electron gas and the heavy particle gas — P_{joule} is the energy input to the electron gas by Joule heating, P_{opt} is the energy loss due to optical radiation, $P_{\text{e,h}}$ accounts for the kinetic energy transfer between the electron gas and the heavy particle gas through elastic collisions, $P_{\text{h,air}}$ is the energy transfer between the heavy particle gas and the ambient air, which includes heat transfer and kinetic energy transfer due to gas expansion.

uniform radially in the bulk and hence are assumed to be only a function of the time and the distance along the channel. Because the gas expansion and ionization in the boundary are neglected, both r_{core} and the core mass density stay constant. Furthermore, since the heavy particles are fully dissociated, n_{h} is also a constant. In Section 4.2.5, we use two simple methods to assess some of the possible effects of the error induced by the assumptions (i) $r_{\text{core}} = \text{const}$ and $n_{\text{h}} = \text{const}$, and (ii) that thermodynamic properties are radially uniform at $r < r_{\text{core}}$.

With the simplifications made above, it is no longer necessary to solve the radial components of the gas momentum equations. The energy equations are simplified as follows:

$$\left(C_v - \frac{3}{2} k n_{\text{h}} \pi r_{\text{core}}^2 \right) \frac{dT_{\text{e}}}{dt} = P_{\text{joule}} + P_{\text{opt}} + P_{\text{e,h}} \quad (4.1)$$

$$\frac{3}{2} k n_{\text{h}} \pi r_{\text{core}}^2 \frac{dT_{\text{h}}}{dt} = P_{\text{h,e}} - P_{\text{h,air}} \quad (4.2)$$

The energy transfer processes described by these two equations are summarized in Figure 4.1. In Equation (4.1), P_{joule} (W/m) is the per channel length rate of energy gain of electron gas by Joule heating, given by $P_{\text{joule}} = E^z I_{\text{core}}$, where I_{core} is dominated by the electron gas flow $j^z E^z$. As is explained in Section 4.1.2, the other component, $j^r E^r$, is much smaller because of the much lower sheath current density. The quantity $P_{\text{opt}} \leq 0$ is

the power loss per channel length due to optical radiation integrated over the entire spectrum. In general, the determination of optical radiation loss requires the solutions of the radiation transport equation or its approximations [Plooster, 1971b, Paxton et al., 1986, Hill, 1977]. For a given temperature and r_{core} , much of the computation can be performed beforehand. In this case, we use the approach suggested in Lowke [1974] and Aubrecht and Bartlova [2009]. Note that all processes of photon emission and absorption involve only free electrons and heavy particle electronic energy states and thus are also functions of only T_e and n_h . The quantity $P_{e,h}$ is the energy transfer by elastic collisions between the electron gas and the translational motion degrees of freedom of the heavy particle gas, given by $P_{e,h} = 3 \frac{m_e}{m_h} \nu_{eh} n_e k (T_e - T_h)$, where ν_{eh} is the momentum collision frequency between electron gas and the heavy particle gas, estimated from σ_e [D'Angola et al., 2008]. The smallness of the factor (m_e/m_h) is responsible for the inefficiency in kinetic energy transfer during collisions between electrons and the much heavier heavy particles. This inefficiency is the fundamental reason for the difference between T_e and T_h during the return stroke rapid heating process. C_v is the constant volume heat capacity per channel length assuming $T_e = T_h$. This term takes heavy particle excitation and ionization into account, as well as the kinetic motion of the electrons and heavy particles. The heavy particle kinetic energy per channel length is given by $\frac{3}{2} k n_h (\pi r_{\text{core}}^2)$, where $n_h (\pi r_{\text{core}}^2)$ is the total number of heavy particles per channel length. Also, $\frac{3}{2} k n_h$ is the constant volume specific heat for the heavy particles, because they are fully dissociated and there are no rotational or vibrational degrees of freedom. With the heavy particle kinetic energy subtracted from C_v , the left hand side of Equation (4.1) represents the internal energy variation with T_e .

Equation (4.2) describes the evolution of the kinetic energy of the heavy particle gas. In this equation, $P_{h,e}$ is the kinetic energy transfer from heavy particle gas to electron gas, with $P_{h,e} = -P_{e,h}$. The quantity $P_{h,\text{air}}$ denotes energy losses from the heavy particles inside the core to the region outside of the core, such as the heat conduction due to temperature gradient and the kinetic energy transfer as a result of gas expansion. The thermal conduction loss is included as in Bazelyan and Raizer [1997, Ch. 2, p. 38–42]. Because of the constant radius assumption, the loss due to gas expansion is neglected. Gas dynamic model calculations show that this type of energy loss accounts for less than 5–10% of the total

energy loss [Plooster, 1971b, Hill, 1977, Paxton et al., 1986]. Moreover, the same conclusions are reached with simulations allowing r_{core} to expand at speeds up to 1000 ms^{-1} (Section 4.2.5).

The set of simplified equations above involve various thermodynamic and transport properties of high temperature air plasma, including the degree of ionization (required to calculate the total particle density and temperature and pressure relationship), the constant volume heat capacity C_v and the electrical conductivity σ_e . For $T_e = T_h$, closed-form expressions for these quantities, with temperature and pressure as the independent variables, are given in *D'Angola et al.* [2008]. For $T_e \neq T_h$, the same expressions can be used with T_e as the temperature and a pseudo-pressure p^s , defined by

$$p^s = (n_e + n_h)kT_e \quad (4.3)$$

Similarly for P_{opt} , p^s is taken as the pressure to make use of the results presented by *Aubrecht and Bartlova* [2009], which gives P_{opt} as a function of temperature, pressure and core radius.

This generalization of the results for $T_e = T_h$ to the case when $T_e \neq T_h$ is valid because, fundamentally, the degree of ionization and the various thermodynamic and transport properties are determined by the electron gas temperature, the heavy particle density and electronic energy states. Under the assumption of partial thermal equilibrium between the electron gas and the heavy particle electronic energy states, these quantities become functions of T_e and n_h .

4.1.2 The sheath

Both experimental observation and theoretical studies of the sheath are still in their early stages. In particular, very limited understanding is available for the construction of a physical sheath model for the fast dynamics during the return stroke.

During the return stroke, the current wave propagates along the core with a speed of the order of the speed of light c . Considering any specific location along the core, within a short temporal and spatial region, the current can be approximately expressed as $I_{\text{core}} = I_{\text{core}}(z - \alpha ct)$, where α is a numerical scaling factor. The quantity αc specifies the current

wave propagation speed and thus α is of a value close to 1. The linear charge density λ accumulation at this location may be estimated by:

$$\frac{\partial \lambda}{\partial t} = \nabla \cdot \mathbf{I}_{\text{core}} = -\frac{1}{\alpha c} \frac{\partial I}{\partial t}$$

For subsequent return strokes, the current at the ground is measured to have a rise time of the order of $1 \mu\text{s}$ and a peak current around 10 kA. The current propagating along a thin conducting core experiences dispersion and attenuation, and thus the rise time increases while the peak current decreases with altitude. As a result, $(\partial \lambda / \partial t)$ is on the order of $10^{-4} \text{ C m}^{-1} \mu\text{s}^{-1}$. Note that this rate decreases with altitude because of the dispersion and attenuation of the current wave. On the other hand, the linear charge density that can induce electric field near the core, which is strong enough to cause air breakdown, may be estimated by

$$\lambda_{\text{thresh}} = 2\pi r_{\text{core}} \epsilon_0 E_{\text{thresh}}$$

where $r_{\text{core}} \sim 1 \text{ cm}$ and $E_{\text{thresh}} \sim 3 \text{ MVm}^{-1}$ is the threshold electric field for electron impact avalanche breakdown. From the above equation, λ_{thresh} is estimated to be $\sim 2 \times 10^{-6} \text{ C m}^{-1}$. That is, in tens of nanoseconds, enough charge can be accumulated in the core to create field necessary for the initiation of streamers, which in turn carries the excess charge into the sheath.

Qualitatively, the sheath contributes to the dynamics of the core in two important ways. The rate at which the charge is carried from the core to the sheath by the streamers, i.e., streamer current, determines the charge balance in the boundary region of the core and the radial component of the current inside the core. The charge redistribution from the core to the sheath affects the axial component of the electric field inside the core and therefore the return stroke current. Unfortunately, the accurate treatment of either problem is extremely difficult. Both the creation and propagation of streamers and the interaction between them remain theoretically and computationally challenging. Extensive study has been done on the creation and propagation of a single streamer. However, the frequency at which streamers are created in the presence of fast charge accumulation remains unknown. Available study on this matter is usually based on the assumption of quasi-stationarity and thus is not

suitable for the study during the return stroke. After all, the large number of streamers involved would make any numerical calculation that attempts to explicitly keep track of each streamer extremely computationally-intensive. Existing theoretical studies and modeling efforts treat the sheath as a continuum medium, using the effective conductivity, permeability and permittivity to represent the average behavior of the streamers [Moini *et al.*, 2000, Lehtinen, 2012]. In this thesis, we take a similar approach and use an empirical model that captures the sheath dynamics on relatively longer time scales ($\sim \mu\text{s}$). Moreover, several measures can be taken to deal with the lack of precise knowledge of the spatial distribution and time evolution of the sheath charge. For example, for the same amount of charge in the sheath, different electric field in the core is produced by the sheath in the model described below with different radius r_{sheath} . The effect of inaccurate assumption on the sheath charge distribution can be effectively examined by comparing the simulation results obtained using different values of r_{sheath} . As to the time evolution, we note, as discussed below, that the time scale for the charge transfer and temporal variation in the sheath charge distribution is of the order of $1 \mu\text{s}$. Similar to the expansion of the core discussed in Section 4.1.1, this time scale implies that the temporal evolution of sheath charge does not alter the qualitative relationship between v_{cur} and v_{opt} . Hence, similar simplifications and test procedures are used for the sheath model.

The sheath is assumed to be a cylinder with its central axis aligned with the core. The radius of the cylinder is independent of altitude and is kept constant throughout the duration of the simulation. The charge distribution within the sheath is assumed to be uniform in the radial direction. The charge transfer current $I_{c,s}$ between the sheath and the core (in the radial direction) is determined by the following rule:

$$I_{c,s} = \begin{cases} 0 & \text{if } \lambda \leq \lambda_{\text{thresh}} \\ \frac{\lambda - \lambda_{\text{thresh}}}{\tau_{\text{sh}}} & \text{if } \lambda \geq \lambda_{\text{thresh}} \end{cases} \quad (4.4)$$

where $\tau_{\text{sh}} \simeq \frac{\epsilon_0}{\sigma_{\text{sh}}} \simeq 1 \mu\text{s}$ is the relaxation time for excess charge in the core to be carried to the sheath. The charge relaxation when $\lambda \geq \lambda_{\text{thresh}}$ is the step response of a capacitor-resistor circuit with $RC = \tau_{\text{sh}}^{-1}$. Thus τ_{sh} can be estimated by considering the sheath conductivity ($\sim 10^{-5} \text{ S m}^{-1}$) estimated in Maslowski and Rakov [2006, 2009]. Other types of charge distributions can be used, which give solutions equivalent to different choices of

the sheath radius. The assumption of any kind of functional form of charge distribution, or, more generally, a quasi-stationary sheath charge distribution, is only valid when it is the sheath charge distribution averaged over a long time scale that is considered. A lower limit of the time scale can be estimated by considering the time it takes for a streamer to traverse a distance comparable to the sheath radius. A fast streamer travels at speeds on the order of 10^7 ms^{-1} [Bazelyan and Raizer, 1997] and the sheath radius is estimated to be a few meters [Maslowski and Rakov, 2006, 2009]. Thus, the time span over which the average is taken needs to be much larger than $0.1 \mu\text{s}$. According to the study by Maslowski and Rakov [2006, 2009], the sheath radius may vary with altitude. This effect is neglected here because the predicted altitude variation in r_{radius} differs significantly depending on the choice of return stroke current model in the studies above and it is not clear which choice is more proper.

In order to calculate the electric field inside the core due to the sheath charge distribution, we note that, because of the low sheath conductivity and thus the large τ_{sh} , only the term involving $[q(\mathbf{x}', t')]_{\text{ret}}$ in the EFIE equation (Equation 2.1) needs to be considered when integrating over the sheath region. However, the other two terms may be underestimated by the model if the charge transfer between the sheath and the core involve processes with short time scales.

4.1.3 Simulation setup

Although the same principles of physics apply to both the first and the subsequent return strokes, it is convenient to focus on the subsequent return stroke for several reasons. Firstly, the return stroke channel properties vary more smoothly because it is created by the dart leader as opposed to the channel for the first return stroke which consists of highly non-uniform steps created by a stepped leader. As a result, for the simulation of subsequent return strokes, the initial conditions specifying the return stroke channel properties are simpler. Secondly, the experimental data of subsequent return stroke study from triggered lightning experiment is rich both in quantity and quality, because of the better controlled experimental environment. Moreover, with triggered lightning, it will be easier to set up experiments that make synchronized observations of the optical radiation, electromagnetic

radiation and return stroke ground current. As it will become clear in this chapter, in order to verify the theoretical predictions of this thesis, this type of experiments will be of great value for the study of the physics of lightning channel.

Subsequent return strokes are usually initiated by the dart-leader process. Dart leaders propagate toward ground along the residual channel of the previous return stroke in a continuous (i.e. non-stepped) fashion, with the speed of the order of 10^7 ms^{-1} . Some dart leaders may exhibit stepping behavior near the bottom portion of the channel, before connecting to the ground and initiating a return stroke. The time interval between the first and the second return strokes, as well as between adjacent subsequent return strokes, is of the order of 50 ms. Despite cooling between return strokes, the temperature of the core remains an order of magnitude higher than ambient temperature ($\sim 300 \text{ K}$) before the dart-leader process starts [Uman and Voshall, 1968]. In the same period, the pressure in the core has essentially reached a value close to atmospheric pressure [Plooster, 1971b]. During the dart-leader process, the core is heated to a temperature close to 20 kK and becomes highly conductive. The pressure also increases, but remains at values close to 1 atm. Because of the background electric field \mathbf{E}_{bg} produced by the cloud charge and its induced ground charge, the charge redistributes inside the core so that the axial component of \mathbf{E}_{bg} is canceled. Given the dart-leader speed, there is sufficient time for core-sheath charge transfer to reach equilibrium, except for the bottom portion of the channel which is several meters long.

The model configuration shown in Fig. 4.2 is used for the simulation of subsequent return strokes. For the purpose of this thesis, we consider a straight lightning channel. While the channel in the model follows a straight line, real lightning channel is tortuous. However, Hill [1968] shows that the average angle of change in channel direction is less than 20° , and thus the error in the channel length representation is less than 6%. Note that Equations (2.1–2.8) are written in vector forms, and thus they are valid for arbitrary channel geometry. In the case of a straight lightning channel, the direction of \mathbf{I}_{core} and the component of the electric field inside the core that is parallel to the core, \mathbf{E}_{core} , no longer depends on the location along the core. As a result, they can be replaced with the scalars I_{core} and E_{core} . The background field E_{bg} is assumed to be uniform, of magnitude 10^5 V m^{-1} . At first, the core is disconnected from the ground by a gap of 3 meters and

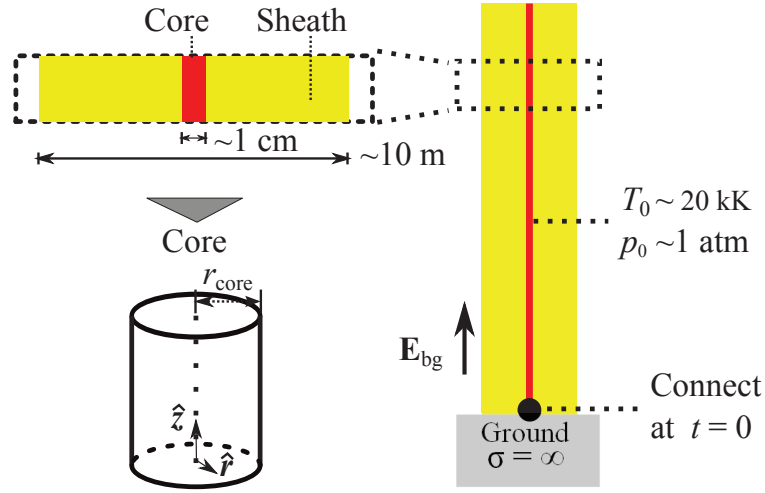


Figure 4.2: Subsequent return stroke simulation setup. T_0 and p_0 are the initial temperature and pressure of the core, σ is the electrical conductivity, E_{bg} is the electric field due to the cloud charge and its induced ground charge

the charge is allowed to redistribute in the core and the sheath until the static equilibrium is reached. Then, at time $t = 0$, the channel is extended to close the gap between the core and the ground by a new core segment, everywhere inside the core, the initial temperature T_0 and the initial pressure p_0 are set to $T_e = T_h = T_0 = 20 \text{ kK}$ and $p_e + p_h = p_0 = 1 \text{ atm}$. Simulations assuming different values of T_0 and p_0 are presented in Section 4.2.4. The actual physical process that closes the gap, the attachment, and the creation of a new channel, unfortunately, can not be analyzed using the theory discussed so far, which relies on the preexistence of a hot plasma channel. In particular, the heating in the present model is confined to the volume within a filamentary core channel, with energy input by current flowing in arc type plasma, while the actual physical process of attachment involves heating of air in a much larger volume and possibly by numerous streamers [Bazelyan and Raizer, 1997, Ch. 6, p. 238–242]. Since physics of the current and optical wave propagation along the core is independent of how the current is generated at the bottom of the channel, the return stroke current at the ground, $I_{\text{core}}(z = 0, t)$, is external to this model and is assumed

to be given by

$$I_{\text{core}}(z = 0, t) = I_{\text{core}}^{\text{max}}(z = 0) \begin{cases} \frac{t}{\tau_{\text{rise}}} & \text{if } t \leq \tau_{\text{rise}} \\ \exp\left(-\frac{t-\tau_{\text{rise}}}{\tau_{\text{fall}}}\right) & \text{if } t \geq \tau_{\text{rise}} \end{cases} \quad (4.5)$$

which is also used gas dynamic models [Plooster, 1971b] and is representative of experimentally recorded ground current [Berger *et al.*, 1975]. In the equation, τ_{rise} , τ_{fall} , $I_{\text{core}}^{\text{max}}$ are the rise time, fall time and peak current respectively. For subsequent return strokes, τ_{rise} and $I_{\text{core}}^{\text{k}}(z = 0)$ mostly fall in the range 0.3–4.5 μs and 5–30 kA, with median $\sim 1 \mu\text{s}$ and $\sim 12 \text{ kA}$ respectively. The fall time τ_{fall} is typically of the order of tens of μs and is fixed at 30 μs for all presented simulations, because its variation has negligible effect in the time window considered.

It is worth noting that, regardless of the value of E_{bg} , charge redistributes in the core and sheath during the dart-leader process in such a way that the axial component of the electric field after reaching the equilibrium is zero inside the core. During the return stroke, the current wave causes a variation in the charge distribution, which is superimposed onto the existing charge distribution, and induces a perturbation to the axial component of the electric field which accompanies the current wave. Consequently, the physics of the return stroke current wave propagation is independent of E_{bg} . On the other hand, at the bottom of the channel, where the dart leader connects with the ground, the charge distribution established during the dart-leader process may be one of the determining factors in the generation of return stroke current (assumed to be given in the present model by Equation (4.5)). Also, the core-sheath charge transfer may be far from equilibrium for this portion of the channel, because the channel is newly created and it may take a time $> 1 \mu\text{s}$ equilibrium to establish. Thus, the possible effects of E_{bg} on the generation of return stroke at the ground are implicitly included by the choice of the values of t_{rise} , t_{fall} and $I_{\text{core}}^{\text{max}}$.

Insofar as the current and optical wave propagation along the core is considered, this model is also applicable to the first return stroke. However, when it comes to determining T_0 , p_0 , r_{core} , as well as the sheath model parameters, several difficulties remain. For example, for a negative cloud-to-ground lightning, the core of the first return stroke is created by a downward stepped-leader process. In each step the leader propagates over a distance of the order of tens of meters. The time interval between steps is of the order of tens of

μs . That is, the times at which the different sections of the channel are created as a result of leader steps can be up to hundreds of microseconds apart. As a result, thermodynamic properties of different portions of the channel may have significantly different values. Since quantitative understanding of the physics of the leader steps is still very limited, it remains unclear how to estimate the distribution of T_0 , p_0 and r_{core} along the core. Moreover, optical observations indicate that leader steps are accompanied by bursts of streamers originating from the tip of the leader, and extending outward over a distance of tens of meters [Berger, 1967]. Limitation in quantitative understanding of this phenomenon means that initial charge distribution in corona sheath is also difficult to estimate. As it is discussed in Section 4.2.4, large variations in these parameters may have significant impact on the optical wave propagation.

4.2 Results and discussion

4.2.1 A subsequent return stroke simulation

We first examine the simulation result for a single return stroke (Fig. 4.3). The temporal and spatial evolution of I_{core} and P_{opt} are shown by Fig. 4.3a and 4.3c respectively. The optical radiation wave front highlighted in Fig. 4.3c corresponds to the time when, at each altitude z , $P_{\text{opt}}(z, t)$ reaches 20% of its peak value at the ground ($z = 0$). v_{opt} is the slope of the wavefront and is approximately $0.45 c$ in this case. This definition of wavefront and wave speed is consistent with the technique used to measure optical return stroke speed from streak camera recordings [Idone and Orville, 1982]. Applying the same definition of wavefront to $I_{\text{core}}(z, t)$, v_{cur} is found to be approximately $0.84 c$. Fig. 4.3f shows a comparison of the wavefronts, which reveals a finite time delay between them.

Both waves experience attenuation and dispersion as they propagate along the core. For example, by fitting an exponential decay curve to $\max_t P_{\text{opt}}(z, t)$, the height decay constant is found to be approximately 0.6 km, in agreement with *Jordan and Uman* [1983]. The 10-90 % rise time of $P_{\text{opt}}(z, t)$, is $0.71 \mu\text{s}$ for $z = 30 \text{ m}$ and $2.3 \mu\text{s}$ for $z = 300 \text{ m}$, in agreement with *Wang et al.* [1999]. In contrast, the height decay constant for $\max_t I_{\text{core}}(z, t)$ is approximately 1.05 km. The 10-90 % rise time of $I_{\text{core}}(z, t)$, is $0.80 \mu\text{s}$ for $z = 30 \text{ m}$ and

0.9 μs for $z = 300$ m.

Analysis of P_{joule} (Fig. 4.3b) and T_e (Fig. 4.3d) offers further insight into the underlying dynamics. Because of the dispersion and attenuation in the current wave, $P_{\text{joule}}(z, t)$ decreases with z (Fig. 4.3b), and so does the heating rate of the core (Fig. 4.3d). On the other hand, P_{opt} is a highly nonlinear function of T_e and thus the wavefront of P_{opt} corresponds to a T_e that is much greater than the initial temperature ($T_e \approx 32$ kK at the optical radiation wave front for the simulation shown). The lower heating rate at higher altitude (due to lower current) means that longer time is required for the core to reach such a high temperature. As a result, the optical radiation wave front is further delayed with respect to the current wave front at higher altitude, hence the lower v_{opt} than v_{cur} .

In Fig. 4.3d, the maximum T_e at ground is approximately 38 kK, reasonably close to the estimated maximum temperature of 36 kK based on spectroscopic observations [Orville, 1968], although the spectroscopic observations have a limited time resolution (~ 2 to $5 \mu\text{s}$) that may reduce the true maximum. The maximum n_e is approximately $8 \times 10^{23} \text{ m}^{-3}$, in reasonable agreement with Orville [1968]. As to $T_e - T_h$, it is significant initially, reaching beyond 1 kK in approximately $2 \mu\text{s}$ after the current wave arrives, but quickly decreases to nearly zero within a few μs (Fig. 4.3e), in agreement with gas dynamics model studies [Paxton *et al.*, 1986].

4.2.2 The definition of return stroke speed

Several types of optical recording techniques are available for experimental study of the return stroke. Depending on the data formats obtained using different recording techniques, two methods are used in the literature to measure the optical wave speed. In streak camera measurements, the generally accepted method is to identify the time when light intensity first exceeds the background level on streak photographs [Idone and Orville, 1982]. A similar method is used to identify the onset point of the return stroke optical wave at each height in photoelectric measurements. Studies of measurements obtained by the Automatic Lightning Progressing Feature Observation System (ALPS) makes use of the fast rising portion of the optical waveform over time to identify the time delay between small channel segments at different heights [Wang *et al.*, 1999].

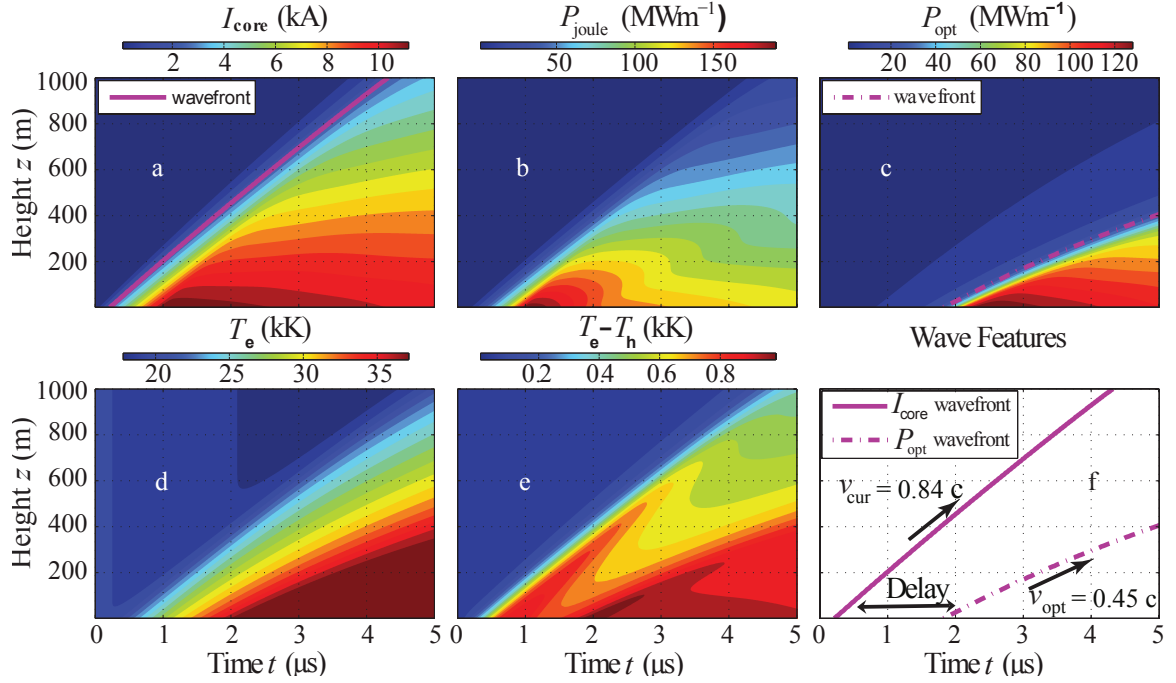


Figure 4.3: The electrodynamics and thermodynamics of a subsequent return stroke. (a) is the return stroke current I_{core} , (b) the joule heating power P_{joule} , (c) the optical radiation power P_{opt} , (d) the electron gas temperature T_e and (e) the different between electron gas temperature T_e and heavy particle gas temperature T_h . The parameter values for this simulation are: $T_0=20$ kK [Orville, 1968], $r_{\text{core}}=4$ mm [Rakov, 1998], $p_0=1$ atm [Uman and Voshall, 1968], $I_{\text{core}}^{\text{max}}=12$ kA, $\tau_{\text{rise}}=1$ μs and $\tau_{\text{fall}}=30$ μs [Rakov and Uman, 2002, Ch. 4, p. 146].

In this section, we discuss two methods to identify the wavefront of the optical wave in the computer simulation, and their correspondence to the two methods used to study the experimental data. After identifying the wavefront, the return stroke optical wave speed v_{opt} , can be found by measuring the distance traveled by the wavefront in a given time window. The same methods are used to find the current wavefront and current wave speed, v_{cur} .

Wavefront using fixed threshold

This method is similar to identifying the time when light intensity first exceeds the background level on streak photographs. The wavefront optical power $P_{\text{opt}}^{\text{thresh}}$ is defined as a fixed fraction α of the peak optical power at the ground ($z = 0$). Figure 4.5b shows several wavefronts according to different choices of α . It is clear that for $\alpha \leq 0.2$ the difference in the resulting return stroke speed is relatively small.

The return stroke speeds presented in the paper and other sections of the supplementary materials are measured using this method. We choose this method because it only requires knowledge of the peak power at the ground rather than at all altitudes.

Wavefront using fast rising portion

The onset point at each altitude z is found by the following procedure. First two points are identified at which the optical power just reaches β_1 and β_2 fractions of the peak optical power at the same altitude. Then a line is drawn going through the two points. The point at which the line crosses the time axis is identified as the onset point at that altitude ($t_{\text{fast rising portion}}$ in Figure 4.4). Finally the wavefront is found by joining the onset points.

Figure 4.5c includes an example of the wavefront obtained using this definition, and for the comparison purpose, also an example using the fixed threshold method. Similar to the first method, the wave speed tend to vary within a small range depending on the value of β_1 and β_2 . However, as Fig. 4.5c shows, the range of variation for the two methods overlap with each other and thus v_{opt} defined with both methods are consistent with each other.

When a single return stroke is considered, v_{opt} varies within a small range ($\pm 10\%$ in Fig. 4.5b) depending on the choice of the values of α , β_1 and β_2 . This variation is only a result of the mathematical definition of v_{opt} (which is related to the measuring technique in an experiment) and does not have a direct physical meaning. When different return strokes are considered, the waveform of $P_{\text{opt}}(z, t)$ does not vary as a simple linear scaling with return stroke parameters such as T_0 , p_0 , τ_{rise} and $I_{\text{core}}^{\text{peak}}(z = 0)$. Consequently, for different return strokes, the same value of α corresponds to different values of $P_{\text{opt}}^{\text{thresh}}$, and the same β_1 and β_2 correspond to different parts of the rising portion of the optical waves. Due to the nonlinear variation in $P_{\text{opt}}(z, t)$, it is not possible to define a v_{opt} that has unique and

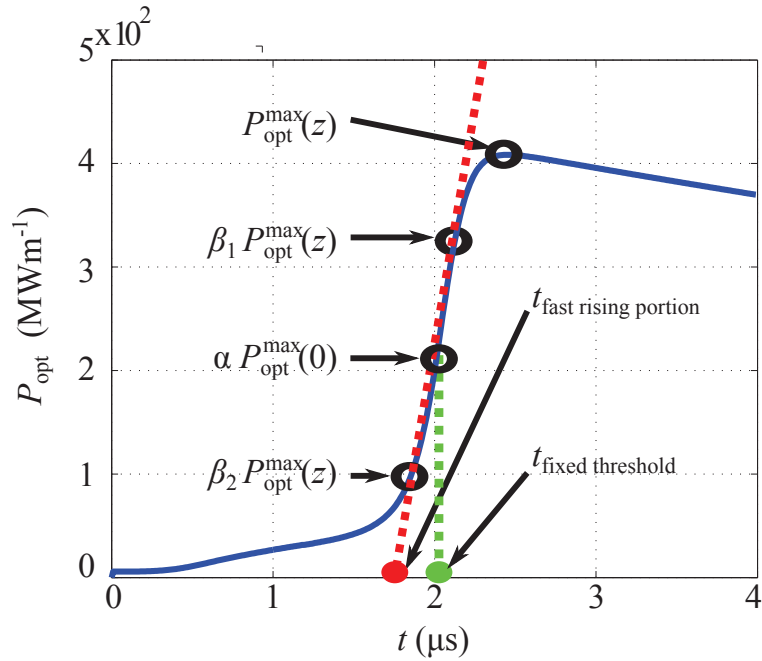


Figure 4.4: Wavefront definition using the fixed threshold and the fast rising portion of the waveform.

consistent physical meaning for all return strokes. As a result, for both methods discussed above, it can be difficult to extract a clear physical meaning from the variations in v_{opt} with different return strokes, especially when the difference in v_{opt} between these different return strokes is relatively small.

4.2.3 The implications of a higher current speed

As shown by *Krider* [1992], *Thottappillil et al.* [2001, 2004], *Thottappillil and Rakov* [2007], the higher v_{cur} has profound effect on the calculated return stroke electromagnetic radiation. For example, calculation of the electric field 100 km away from return stroke channel base as presented by *Thottappillil and Rakov* [2007] shows that, as v_{cur} increases from $0.5c$ to c , the field angular distribution becomes more focused towards the vertical direction above the channel and the field peak amplitude rapidly increases by over an order of magnitude. The higher peak electric field directly leads to a higher probability of initiation

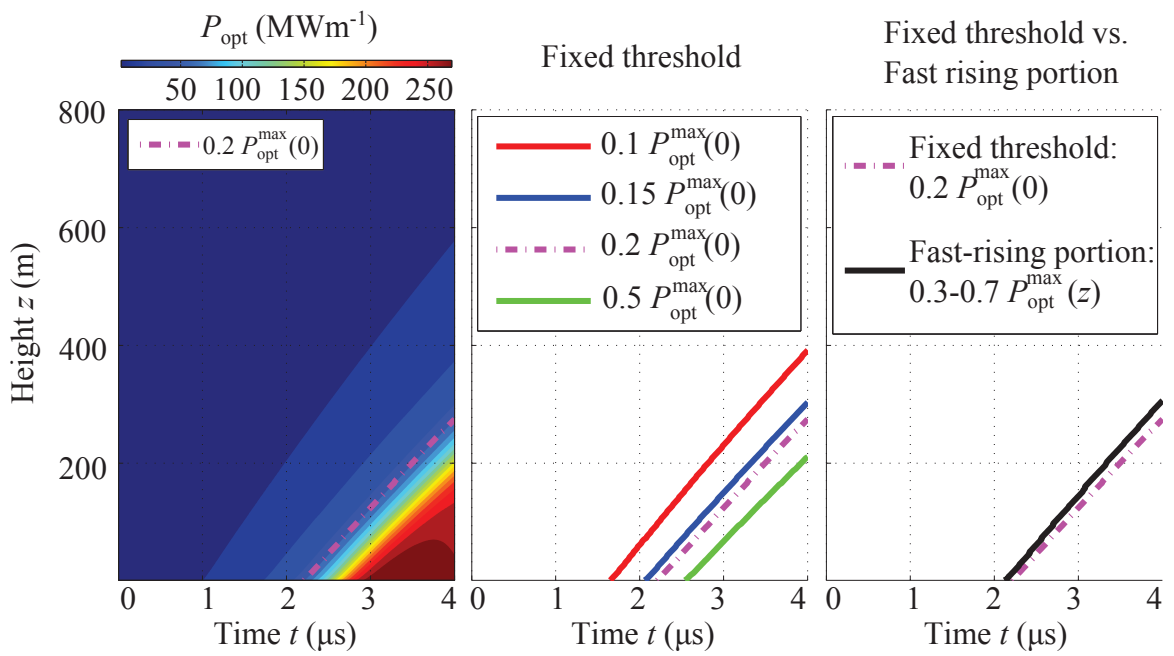


Figure 4.5: (a) Optical power and the wavefront using the method in Section 4.2.2, with $\alpha = 0.2$. (b) Wavefronts using method in Section 4.2.2, with $\alpha = 0.1, 0.15, 0.2$ and 0.5 . Correspondingly, $v_{\text{opt}} = 0.57c, 0.53c, 0.52c, 0.48c$ respectively. (c) Wavefronts using methods in both sections. v_{opt} found using the method in Section 4.2.2 is $0.54c$.

for Transient Luminous Effects (TLE) in the mesosphere, while the field angular distribution may affect the geometrical appearance of these phenomena. Generally speaking, the relationship $v_{\text{cur}} > v_{\text{opt}}$ is important for lightning geolocation [Cummins *et al.*, 1998] and lightning-upper-atmosphere coupling applications [Cummer *et al.*, 1998], for which the electromagnetic pulse radiated from lightning has been derived by assuming $v_{\text{cur}} = v_{\text{opt}}$. It is also of interest to note that, based on comparison between the calculated and experimentally observed electromagnetic field near return stroke channel, Thottappillil *et al.* [2001] suggests the possibility of $v_{\text{cur}} \approx c$ near the bottom of the channel.

4.2.4 Model parameter dependence

The delay of the optical radiation wave relative to the current wave also varies appreciably with initial conditions of the core. For example, Figure. 4.6 shows the increase in the time delay between the peak I_{core} and peak P_{opt} at the ground with decreasing initial temperature. Further experiments with rocket-triggered lightning that look into the time delay between channel base current and optical emissions may be used to narrow down the parameters of the initial states of the core near ground. Also it is worth noting that, for a real return stroke, the core initial temperature is expected to be lower at higher altitudes, and thus the delay of the optical radiation wave with respect to the current wave is expected to be further increased. As a result, v_{opt} could be even further reduced relative to v_{cur} at higher altitudes.

Figure 4.7 presents v_{cur} (dash lines) and v_{opt} (solid lines) for a series of simulations using different values of r_{core} and $I_{\text{core}}^{\text{max}}$. The shaded areas indicate the variation in v_{opt} as the threshold used to identify optical radiation wavefront is varied from 15% to 25% of the maximum $P_{\text{opt}}(z, t)$ at $z = 0$. As noted above, v_{cur} varies much less with the choice of threshold. However, even after taking into account these variations, the dependence of v_{opt} on r_{core} is still very pronounced. This dependence is a result of the highly nonlinear dependence of P_{opt} on r_{core} [Aubrecht and Bartlova, 2009]. On one hand, the strong dependence suggests that precise calculation of v_{opt} requires improved treatment of the radial dynamics of the core, as well as more accurate knowledge of the initial condition of the core. On the other hand, v_{cur} being consistently higher than v_{opt} for a wide range of parameter values,

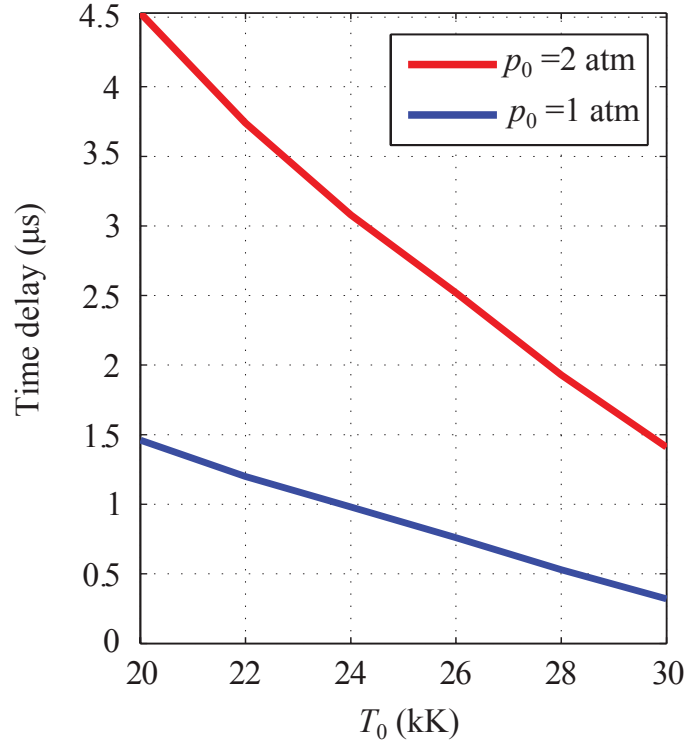


Figure 4.6: The time delay of peak P_{opt} relative to peak I_{core} at ground as a function of the initial channel temperature T_0 for initial pressure $p_0 = 1, 2$ atm. For all the simulation presented, $p_0 = 1$ atm, $r_{\text{core}} = 4$ mm, $I_{\text{core}}^{\text{max}} = 12$ kA, $\tau_{\text{rise}} = 1 \mu\text{s}$ and $\tau_{\text{fall}} = 30 \mu\text{s}$.

as well as for simulations that allow r_{core} to expand according to predefined functions, confirms that the relationship is robust against the errors associated with model assumptions of the core. Also note that the large variation in v_{opt} for a given $I_{\text{core}}^{\text{max}}$ may partially explain the absence of correlation between $I_{\text{core}}^{\text{max}}$ and v_{opt} observed by *Mach and Rust* [1989]. In contrast, v_{cur} appears to be independent on $I_{\text{core}}^{\text{max}}$. This independence indicates that $I_{\text{core}}(z, t)$ scales approximately linearly with $I_{\text{core}}^{\text{max}}$, despite of the nonlinear dependence of σ_e on T_e and in turn on $I_{\text{core}}^{\text{max}}$. This is because, with $T_e \geq 20$ kK, the core remains highly conductive for the entire duration of return stroke. However, the linearity no longer holds in the presence of core expansion. Similar tests are performed for the other model parameters, and in all cases v_{cur} is consistently higher than v_{opt} , confirming that the relationship is unaffected by errors associated with the model assumptions.

Examination of how simulation results vary with different constant values of r_{core} is

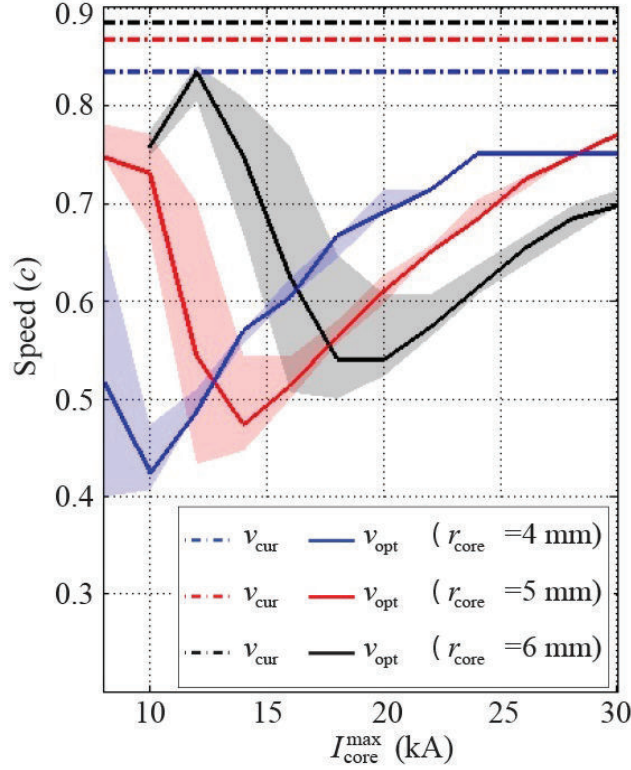


Figure 4.7: The variation of v_{opt} and v_{cur} with r_{core} and $I_{\text{core}}^{\text{max}}$. v_{cur} and v_{opt} are normalized w.r.t the speed of light c . For all the simulation presented, $T_0 = 20$ kK, $p_0 = 1$ atm, $\tau_{\text{rise}} = 1 \mu\text{s}$ and $\tau_{\text{fall}} = 30 \mu\text{s}$. The shaded areas indicate the variation in v_{opt} as the threshold used to identify optical radiation wavefront is varied from 15% to 25% of the maximum $P_{\text{opt}}(z, t)$ at $z = 0$. v_{opt} for $r_{\text{core}} = 6$ mm and $I_{\text{core}}^{\text{max}} < 10$ kA is not shown, because in these cases, 20% of the maximum optical power at ground is less than the initial optical power and thus the definition does not apply.

also important for several other reasons. According to gas dynamic model calculations, the free electron density distribution in the radial direction $n_e(r)$ varies relatively slowly at first near the center and, after a distance of a few millimeters away from the center, falls rapidly by several orders of magnitude over a narrow but finite sized region. On the other hand, in the model $n_e(r)$ is assumed to be constant in r at first and then falls sharply to zero at r_{core} . This r_{core} is best interpreted as an effective radius with which the idealized model of the core can represent the behavior of the real core. For a given $n_e(r)$ profile, finding the correct choice of r_{core} is not simple. Moreover, estimations of r_{core} based on

optical observations are more likely to be the optical thickness of the core rather than the dimension over which n_e is significant. Thus it is necessary to examine how sensitivity the result is to variations in r_{core} .

4.2.5 The expanding core

Without solving the full set of hydrodynamics equations, it is not possible to include the core expansion in a self-consistent manner. Nevertheless, r_{core} can be made to vary in time according to a predefined function $r_{\text{core}}(t)$. By further specifying the contributions of the ionization and gas expansion factors to this function, this approach can be used to examine how each factor or a mixture of both affects the simulation results.

Simulation results shown in Fig. 4.8b,c assume that core expansion is only caused by gas expansion in the bulk and thus the total number of heavy particles is a constant throughout the simulation. $r_{\text{core}}(t)$ is varied according to the function:

$$r_{\text{core}}(z, t) = \begin{cases} r_0 & \text{if } t \leq t_0(z) \\ r_0 + v_{\text{core}}t & \text{if } t \geq t_0(z) \end{cases} \quad (4.6)$$

where z indicates the location along the core, r_0 the initial core radius and v_{core} the core expansion speed; $t_0(z)$ is the time at which the current starts to rise from zero. Note that $t_0(z)$ is a function of z while v_{core} is independent of both t and z . An alternative choice of $r_{\text{core}}(t)$ would be an analytical formula based on gas dynamic model calculations [Plooster, 1971b], as shown below in Equation (4.7).

$$r_{\text{core}}(t) \approx 9.35 I_{\text{core}}(t)^{\frac{1}{3}} t^{\frac{1}{2}} \text{cm} \quad (4.7)$$

Nevertheless, for qualitative study Equation (4.6) is sufficient. Moreover, the Equation (4.7) is only valid for the linear rising portion of the return stroke current, while the return stroke current in these simulations experience significant variation with altitude and time, and thus Equation (4.7) does not necessarily lead to a more accurate estimation.

The heavy particle kinetic energy loss per unit length of the core, P_{kin} , associated with the gas expansion is taken into account by subtracting the following term from the energy

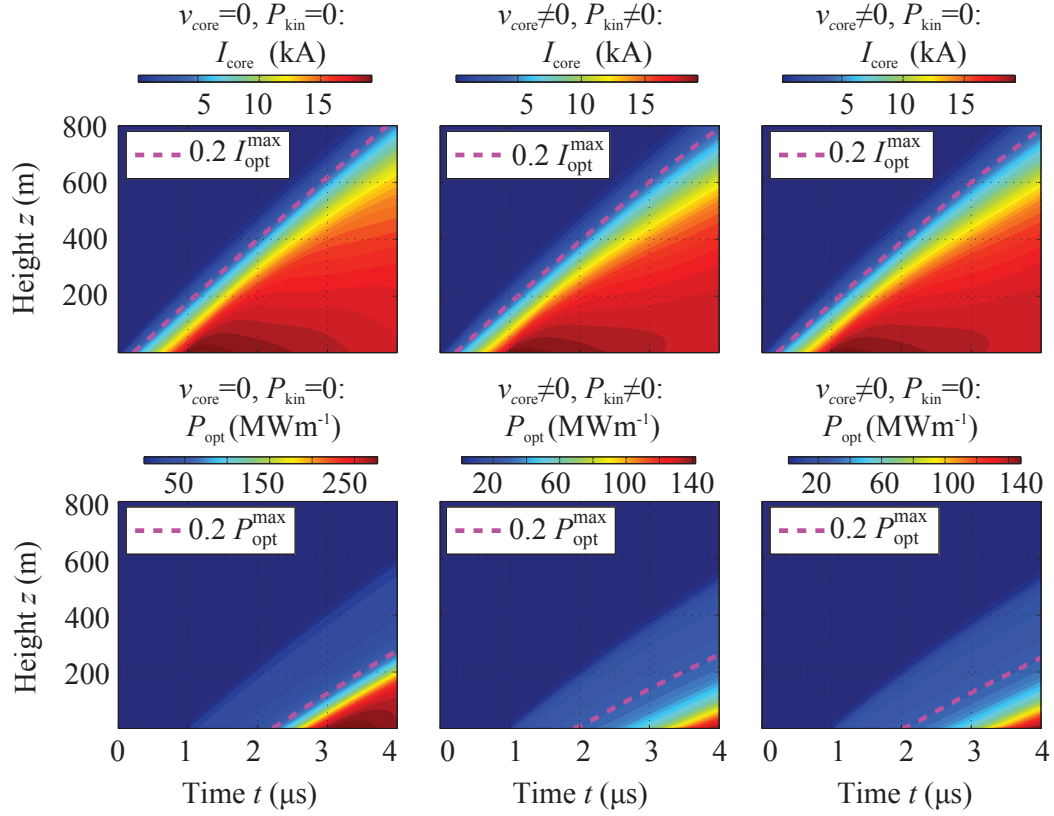


Figure 4.8: Effect of gas expansion in the core. Left: $r_{\text{core}} = \text{const}$. Middle: r_{core} varies according to Equation (4.6) with $v_{\text{core}} = 500 \text{ m s}^{-1}$. P_{kin} is taken into account as in Equation (4.8). Right: r_{core} varies according to Equation (4.6) with $v_{\text{core}} = 500 \text{ m s}^{-1}$. $P_{\text{kin}}=0$.

gain in Equation (4.2).

$$P_{\text{kin}} = 2\pi r_{\text{core}}(z, t) p_{\text{h}}(z, t) \frac{\partial r_{\text{core}}(z, t)}{\partial t} \quad (4.8)$$

Note that p_{h} is used because n_e is by definition only nonzero inside the core. In Fig. 4.8, comparison is made between simulations with $v_{\text{core}} = 0 \text{ m s}^{-1}$ and 500 m s^{-1} . The wavefront portion of the current wave shows very little difference between all three cases. In particular, v_{cur} is approximately $0.75c$ in all three cases. This is in agreement with the argument that I_{core} can be estimated with high accuracy while neglecting the radial dynamics within each short time frame. The difference increases with time, as a result of

core expansion. On the other hand, the optical wave patterns with core expansion show appreciable differences from that with constant r_{core} . Interestingly, the difference between simulations with and without kinetic energy loss is relatively small, implying that changes in the optical wave primarily stem from the dependence of thermodynamic properties and P_{opt} on pressure, particle density and core radius, rather than from the extra kinetic energy loss optical velocity. v_{opt} is about $0.52c$ for constant r_{core} and $0.45c$ for cases with core expansion. The peak optical power is nearly halved for simulations with core expansion in comparison with that assuming constant r_{core} . The apparently reduced τ_{delay} in the case of core expansion is not physical and is largely a result of how the wavefront is defined (Section 4.2.2).

4.2.6 Validation of ionization equilibrium assumption

The model assumes that in the bulk of the core, ionization and excitation of the heavy particles are always at partial thermal equilibrium with the electron gas at T_e . During the return stroke, the core temperature remains above 20 kK. In this temperature regime, both electron impact and photon-particle interaction contribute to the ionization and excitation of heavy particles. In order to examine the validity of the partial equilibrium assumption, it is necessary to explicitly take into account of the contribution to the finite rate of ionization and excitation by both mechanisms. Unfortunately, rigorous treatment of these rates remain both theoretically and computationally challenging for a number of reasons. In particular, the different heavy particle species (O, O⁺, N, N⁺ etc) can no longer be combined as a single species but have to be treated separately. Also, within each heavy particle species, the difference in reaction rates for different electronic energy states may make it necessary to divide the single species into subspecies based on grouping by the electronic energy states, which also absorb and emit photons at different rates. Thus, to find the optical radiation intensity, it becomes necessary to explicitly solve the radiation transport equations separately for a large number of optical frequencies [Zel'dovich and Raizer, 2002, Ch. 5, p. 283–303]. In summary, attempts to include more rigorous treatment of the ionization and excitation lead to an explosion in the model complexity and quickly make the model computationally intractable.

In this section, we first introduce several modifications to the model which take into account the finite rate of ionization by electron impact. Then, the ionization rate is scaled up with a multiplication factor to simulate the boost in ionization rate by photo-ionization. We first describe an enhanced model and then study the conditions for partial equilibrium in ionization and excitation.

Extensions to the model which include ionization dynamics

In the extended model, the different heavy particle species (O, O⁺, N, N⁺ etc.) are treated separately. That is, their densities are no longer determined by Saha equilibrium equations and must be explicitly included as state variables of the plasma. Since the kinetic energy transfer between heavy particles remains an efficient process, their translational motion reach equilibrium quickly and share a common T_h as before. Ionization and excitation, as well as their reverse processes, are essentially transitions between the electronic energy states of the heavy particles. For each heavy particle species, the energy gap between its ground state and the first excited electronic energy states is several eV larger than the gaps between higher energy states. Given that state transition rates depend on energy gap exponentially, the transition between the ground state and the first excited state is by far the slowest. Once excited, the energy gap for ionization become much smaller. Thus, once an electron in the heavy particle is excited from the ground state to the first excited state, it is also assumed to immediately become ionized. That is, the ionization rate is assumed to be equal to the excitation rate from the ground state to the first excited state. Direct transitions between the ground state and the second or higher energy states are neglected, since they are much smaller than the transition rate between the ground and the first excited state [Zel'dovich and Raizer, 2002, Ch. 6, p. 386–396].

With these assumptions, the temporal evolution of particle densities are given by a series of equations involving the ionization rates of the different heavy particle species. As an example, n_e satisfies:

$$\frac{\partial n_e}{\partial t} = \sum_i \alpha_{i,e} n_i n_e - \sum_i \beta_{i,e} n_i^+ n_e^2$$

where i represent heavy particle species. Note that for the temperature and pressure range

considered, only singly and doubly ionized ions need to be included [D'Angola *et al.*, 2008]. The first term on the right hand side represents the total ionization rate of heavy particles, in this case it is given as the excitation rate from the ground level to the first excited level of the electronic energy states. The second term represents the reverse processes of recombination, in which $\beta_{i,e}$ is related to $\alpha_{i,e}$ by the principle of detailed balance.

$$\beta_{i,e} = \frac{\alpha_{i,e}}{K_{i,e}(T_e)}$$

where the equilibrium constant $K_{i,e}(T_e)$ is determined by Saha equation [Zel'dovich and Raizer, 2002, Ch. 6, p. 387].

Electrical conductivity σ_e can no longer be estimated using the method discussed in Section 4.1, because the system is not necessarily in thermal equilibrium. Instead, it is calculated as a function of T_e and particle densities of all the particle species present [Mason *et al.*, 1967, Devoto, 1966]. Thermal conduction is neglected because it is found to be negligible in comparison with Joule heating, optical radiation loss and ionization loss in the simulations discussed in the paper, as well as in gas dynamic model calculations.

Similarly, the method used in Section 4.1 for the estimation of optical radiation no longer applies. Since the calculation of optical radiation in the fully-dynamic scenario is computationally extremely expensive, the following approximation is used instead. At first, a n_e^{eq} is calculated assuming that the ionization and excitation are in thermal equilibrium at T_e . Then a $P_{\text{opt}}^{\text{eq}}$ is found in the same way as in the model discussed in the paper. At last, the actual optical power loss is approximated by scaling down $P_{\text{opt}}^{\text{eq}}$ using the following formula:

$$P_{\text{opt}} = P_{\text{opt}}^{\text{eq}} \left(\frac{n_e}{n_e^{\text{eq}}} \right)^2$$

Strictly speaking, this formula is only applicable for frequencies at which the core appears to be optical thin, which mostly corresponds to the Bremsstrahlung radiation due to interactions between charged particles. For frequencies at which the photon absorption mean free path is comparable or smaller than the core radius, the estimation of optical radiation power in non-equilibrium situation is difficult. As to the rate of ionization, the photons can either increase the rate through photon absorption processes or reduce it by reducing the density of excited heavy particles through induced emission. To study the effect of these

processes, we use a multiplication factor

$$\theta = \frac{\alpha_{i,e}^{\text{eff}}}{\alpha_{i,e}}$$

to modify electron-impact ionization rate. $\beta_{i,e}$ is adjusted accordingly to ensure that Saha equilibrium equations are satisfied at equilibrium.

Equilibrium Conditions

In order to examine whether the partial equilibrium assumption of ionization and excitation is satisfied, we introduce the following metric as an indicator of the distance from partial thermal equilibrium

$$\eta_{i,k}^{\text{eq}} = \frac{1}{K_{i,k,e}(T_e)} \frac{n_e n_i^{k+1}}{n_i^k}$$

where i denotes the atom type ($i = \text{O}, \text{N}$) and k denotes the degree of ionization ($k = 0, 1$). $K_{i,k,e}$ is the equilibrium constant and is given by Saha equation. It is the ratio between the densities when they reach thermal equilibrium:

$$K_{i,k}(T_e) = \left(\frac{n_e n_i^{k+1}}{n_i^k} \right)_{\text{eq}}$$

Ionization equilibrium is achieved when $\eta_{i,k}^{\text{eq}} = 1$ for all i and k . A value smaller than 1 indicates that ionization dominates over recombination and a value larger than 1 indicates the opposite. Note that this metric is nonlinear. For example, if both n_e and n_i^{k+1} are at 70% of their equilibrium value, $\eta_{i,k}^{\text{eq}} = 0.49$, while if both n_e and n_i^{k+1} are at 1% of their equilibrium value, $\eta_{i,k}^{\text{eq}} = 10^{-4}$. At higher temperatures when double ionization become significant, the ionization rate is very high and ionization equilibrium is always satisfied, hence only the rate of single ionizations are tested.

In Figure 4.9, $\eta_{i=\text{N},k=0}^{\text{eq}}$ for the core near the ground is shown for $\theta = 1, 5$ and 10. The ionization energy of O is similar to that of N and thus $\eta_{i=\text{O},k=0}^{\text{eq}}$ behaves similarly to $\eta_{i=\text{N},k=0}^{\text{eq}}$. In all three cases, $T_0 = 20$ kK, $p_0 = 2$ atm, $r_{\text{core}}, \tau_{\text{rise}} = 1$ μs , $\tau_{\text{fall}} = 30$ μs and

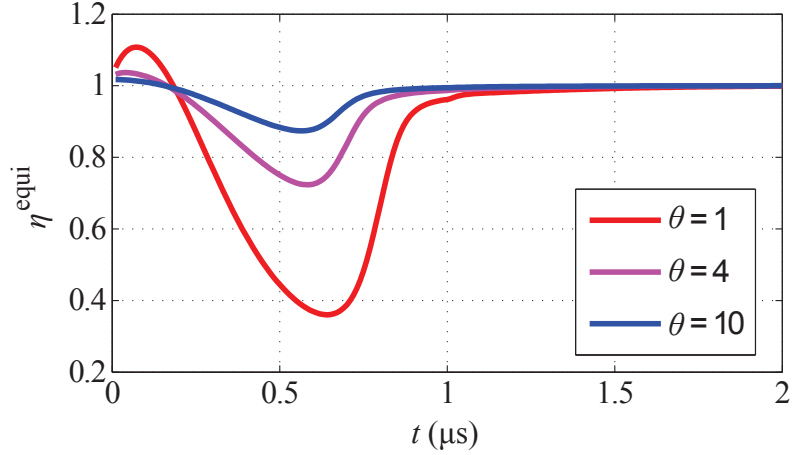


Figure 4.9: Tests of heavy particle ionization equilibrium at T_e during return stroke. For all simulations presented, $T_0 = 20$ kK, $p_0 = 2$ atm, r_{core} , $\tau_{\text{rise}} = 1$ μs , $\tau_{\text{fall}} = 30$ μs and $I_{\text{core}}^{\text{max}} = 12$ kA.

$I_{\text{core}}^{\text{k}} = 12$ kA. Note that η is initially higher than 1, despite the assumption that the channel is initially at thermal equilibrium before the return stroke current is initiated. This is because of the error in the interpolated formula for particle densities as a function of temperature and pressure [D'Angola *et al.*, 2008]. Nevertheless, this error does not affect the study of equilibrium condition.

At $\theta = 1$, i.e. only ionization by electron impact is taken into account, the deviation from partial thermal equilibrium is relatively large for the first 1 μs . However, even at $\theta = 4$, the system is not far from partial thermal equilibrium. At $\theta = 10$, ionization equilibrium is almost always satisfied throughout the duration of return stroke. Since photon ionization rate can be much higher at the high temperatures of the core, we conclude that it is reasonable to assume ionization equilibrium for return stroke simulation.

4.2.7 Analysis of other parameter variations

The study of the variation of simulation results with model parameters is useful for several reasons. The parameters for the core, T_0 , p_0 and r_{core} may have different values for different return strokes as a result of variations in the physical condition, examples of which are the dart leader speed and the time between the dart leader and the previous return stroke. For a

particular return stroke, both T_0 and p_0 may be higher near the bottom of the channel. Also, the error may come from the estimations of T_0 and p_0 in the literature. As to the sheath, the empirical model is only a semi-qualitative representation of the actual physics and it is important to check that conclusions made in the paper are unaffected by variation in the sheath model parameters. Parameters for the numerical calculation are the time step δt and spatial grid size δL . They must be small enough to ensure the numerical accuracy.

In the following discussion, comparisons are made between a base case and simulations in which the value of one of the model parameters is varied. The base case uses the following parameter values: $T_0 = 10$ kK, $p_0 = 1$ atm, $r_{\text{core}} = 5$ mm, $r_{\text{sh}} = 4$ m, $\tau_{\text{sh}} = 1$ μs .

Figure 4.10 shows $I_{\text{core}}(z, t)$ and $P_{\text{opt}}(z, t)$ for simulations using three different values of T_0 : $T_0 = 10$ kK, 13 kK and 16 kK. Correspondingly we obtained for these cases, $v_{\text{cur}} \simeq 0.75 c, 0.8 c$, and $0.85 c$ and $v_{\text{opt}} \simeq 0.52 c, 0.55 c$, and $0.66 c$. In other words, both v_{cur} and v_{opt} increase with T_0 . Also, for higher T_0 , τ_{delay} is decreases. For a subsequent return stroke, the core preheated by dart leader may have a higher temperature near the bottom. This temperature gradient may partly contribute to cause the decreasing v_{opt} with altitude that was reported in *Idone and Orville* [1982].

Figure 4.11 shows $I_{\text{core}}(z, t)$ and $P_{\text{opt}}(z, t)$ for simulations using two different values of p_0 : $p_0 = 1$ atm and 2 atm. Correspondingly, we obtained $v_{\text{cur}} \simeq 0.75 c$, and $0.75 c$ and $v_{\text{opt}} \simeq 0.52 c$ and $0.58 c$. While $I_{\text{core}}(z, t)$ is nearly unaltered, the rise time of $P_{\text{opt}}(z, t)$ increases significantly with the pressure. One possible explanation is that, under the same r_{core} and T_0 , a higher p_0 means higher total mass of the core, which in turn leads to increased heat capacity and thus lower heating rate in the core. Despite the significantly different rise times, we observe that in both cases v_{cur} is significantly higher than v_{opt} and τ_{delay} is finite.

Figure. 4.12 shows $I_{\text{core}}(z, t)$ and $P_{\text{opt}}(z, t)$ for simulation results using three different sets of sheath model parameters, r_{sh} and τ_{sh} : $r_{\text{sh}} = 4$ m, $\tau_{\text{sh}} = 1$ μs ; $r_{\text{sh}} = 8$ m, $\tau_{\text{sh}} = 1$ μs ; and $r_{\text{sh}} = 4$ m and $\tau_{\text{sh}} = 0.5$ μs . Correspondingly, we obtained $v_{\text{cur}} \simeq 0.75 c$ for all three cases and $v_{\text{opt}} \simeq 0.52 c, 0.51 c$, and $0.59 c$. Changes in r_{sh} has little impact on $I_{\text{core}}(z, t)$ and $P_{\text{opt}}(z, t)$. The variation of τ_{sh} has a more significant effect. Nevertheless, for the purpose of the primary conclusions put forth in this thesis, we observe that v_{cur} still remains significantly higher than v_{opt} and τ_{delay} remains finite.

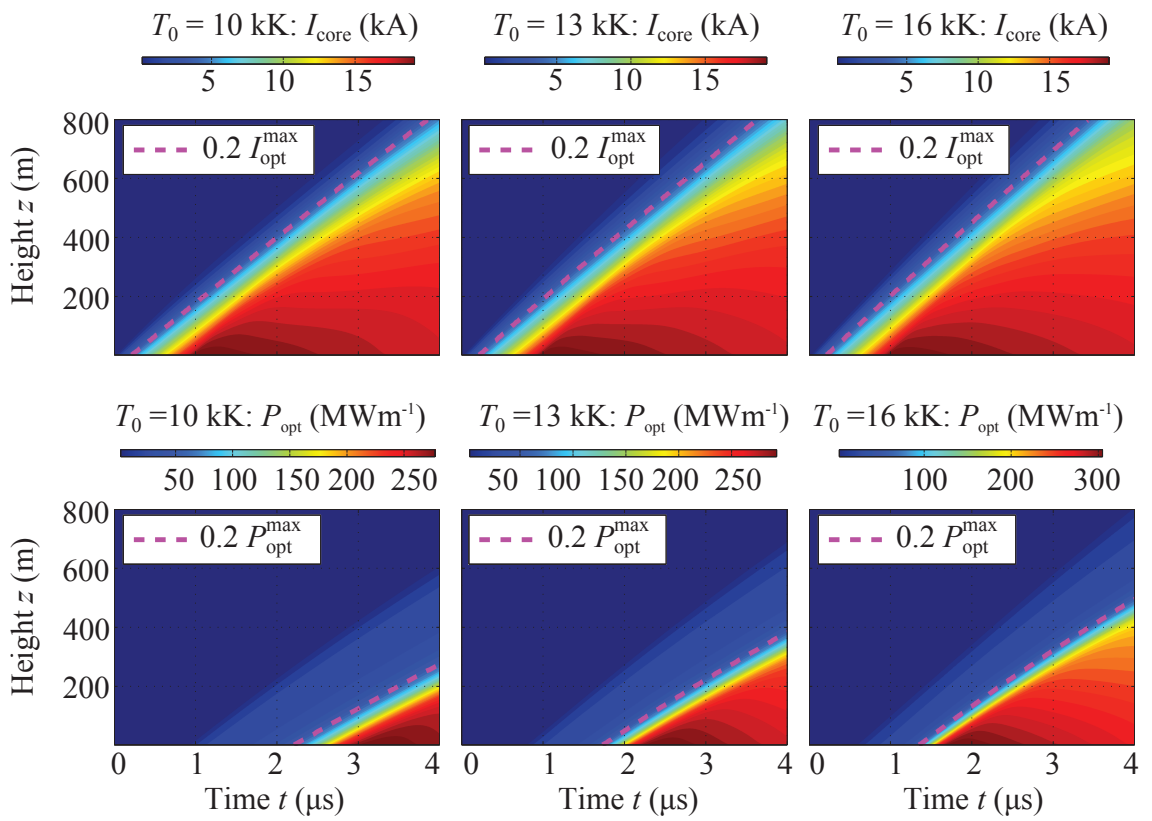


Figure 4.10: Variation in initial temperature T_0

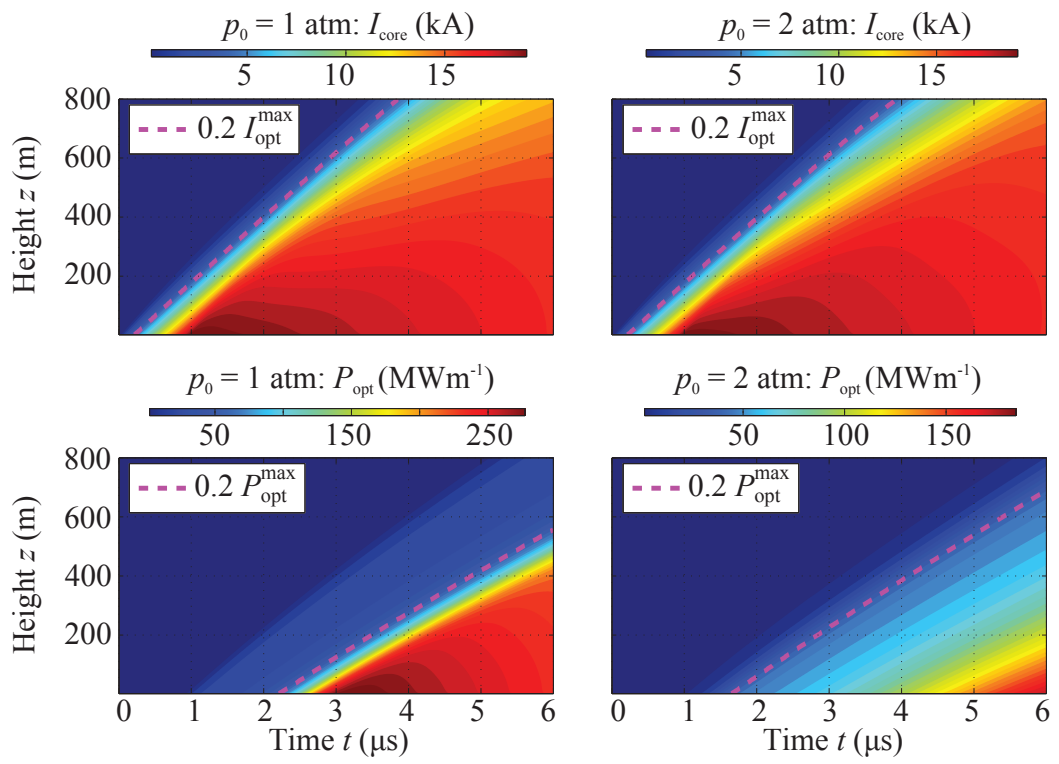


Figure 4.11: Variation in p_0

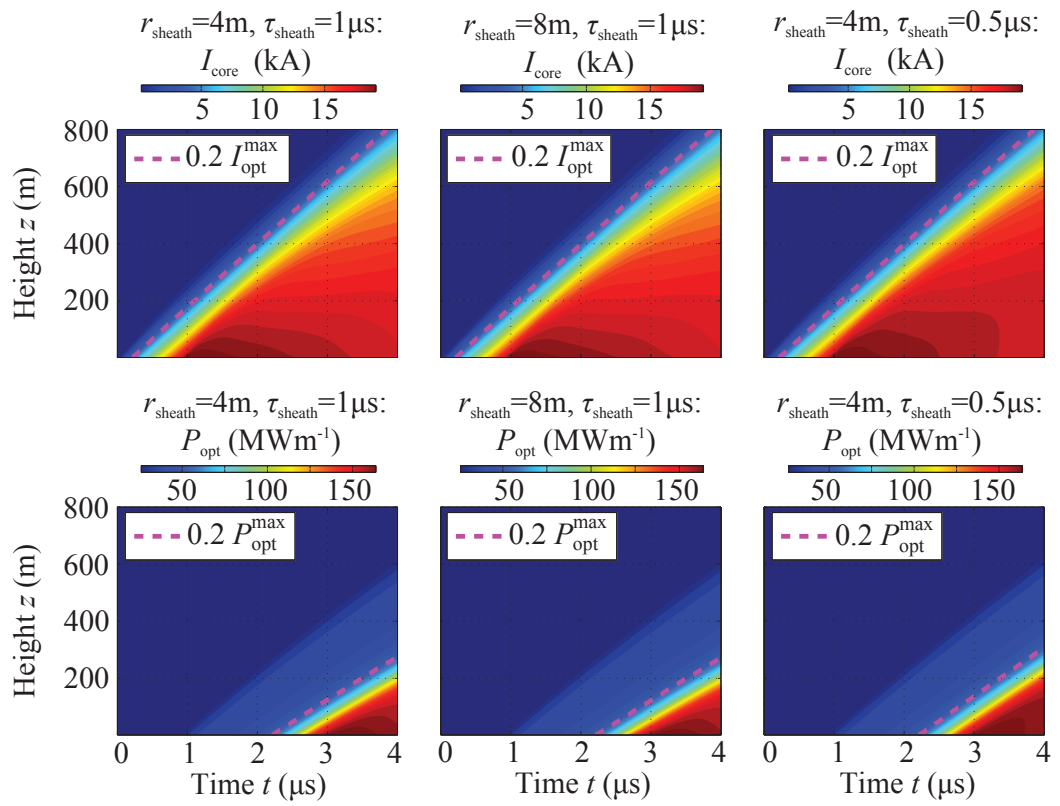


Figure 4.12: Variation in sheath model parameters r_{sh} and τ_{sh}

Chapter 5

Single Leader Step Study

As was briefly discussed in Chapter 2, the micro-physical processes that underly the leader development, especially the streamer-leader transition, are not well understood. Consequently, the construction of a physically accurate model for leader process is still out of reach. On the other hand, the theory discussed in Chapter 4 is applicable to the new lightning channel that had already being created by the leader process. Based on this consideration, we discuss the extension to the model by using a phenomenological model for the simulation of leader steps. In this model, a new lightning channel created by the leader process is explicitly added into the computational domain, while the leader characteristics such as its type, length, direction, propagation speed are directly specified based on experimental observations.

Without explicit treatment of the micro-physical processes, this model is unable to make predictions to the leader characteristics. Nevertheless, as discussed in Section 5.2, the model can potentially be useful for the study of ground station recordings of the electromagnetic pulse signals associated with the leader steps taking place inside the cloud. Moreover, in Chapter 6, this model forms one of the building blocks of a larger model that can be used to study the large scale lightning channel geometrical structure.

In fact, with the ground station recordings as the primary method of observation for the leader process, it could be difficult to provide comprehensive experimental verifications for more sophisticated leader models that attempt to include the micro-physical processes. It is thus of interest to use the phenomenological model as a preliminary probe to investigate

the dependence of the predicted electric field at the ground on the model parameters. The result can then be used as a guideline for the development of parsimonious leader models for applications that only target ground station recordings, and for highlighting important effects to capture the design of a more physically accurate model.

5.1 The Phenomenological Leader Model

In this model, new portions of highly conductive lightning channels are directly added into the computational domain to mimic the observed leader mechanisms. The leader characteristics such as its location of initiation, length, direction and propagation speed are specified as model parameters based on averages of experimental observations. A new leader is discretized into current and charge segments in the same way as the existing channel. The current segments are added into the system over time so that the average leader extension speed is as specified, while the charge and sheath segments are updated accordingly. The initial status of the thermodynamic properties of the newly added current segment, such as its initial temperature, pressure and radius, also need to be directly specified. Measurements for these quantities are limited. Because streamer-leader transition takes place within the temperature range of $3000 \sim 5000$ K, the initial channel temperature can be set to a value in this range. The initial values for channel pressure and radius are less certain. Considering the time it takes for streamer-leader transition to take place ($\sim 30 \mu s$), it may be reasonable to set the initial pressure to a value close to the atmosphere pressure. The initial radius could be of the order of a few millimeters to centimeters according to the typically observed laboratory long spark discharge and lightning channel radius.

Based on the total charge near its location of initiation, a leader is determined to be a positive leader if the total charge is positive and a negative leader if the total charge is negative. Correspondingly, new channel segments are added in to the system according to the schematics shown in Figure 5.1 to mimic the experimentally observed leader development (Section 2.4).

The computational flow discussed in Chapter 3 is modified to include the stage of adding new current segments (Figure 5.2). Note that once a new current segment is added into the system, the charge and current are updated accordingly in the next time step.

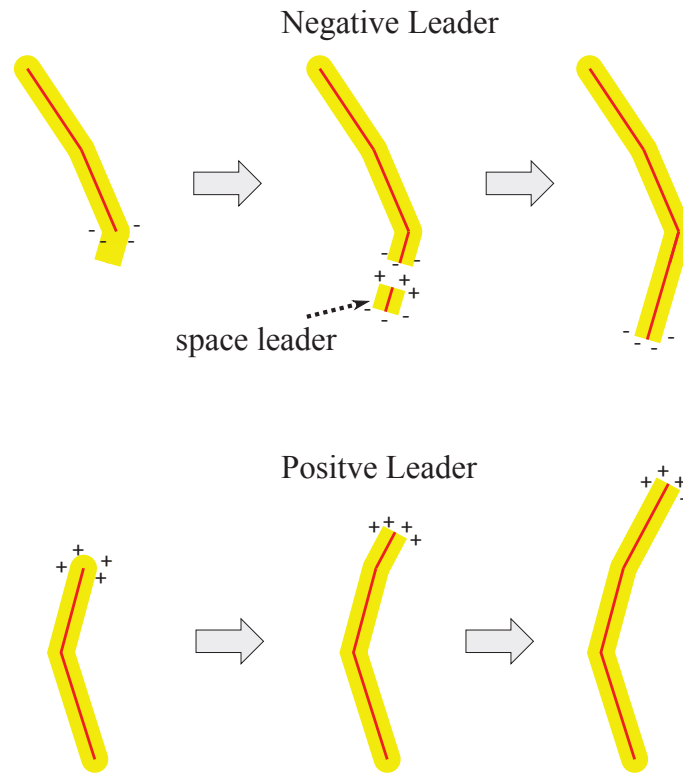


Figure 5.1: Schematic plot for the negative (top panel) and the positive (bottom panel) leaders. In the phenomenological leader model. Current segments are added into the computational domain to mimic the schematic plots.

It is important to realize that the current segment length needs to be chosen based on considerations of the spatial gradient along the lightning channel. In Chapter 4 we briefly mentioned that current segments with a length of 3 m is sufficient because the difference between simulation results using 3 m and 1.5 m long current segments is negligible. Fundamentally, this is because of the relatively long rise time of the return stroke current ($> 1\mu s$) and thus the low spatial gradient along the channel. Unfortunately, this statement no longer holds true near the tip of a lightning channel. This is because the current and charge distribution, as well as the thermodynamic properties of the channel, vary rapidly over a small distance along the channel near the tip. Consequently, the method discussed above inevitably introduces numerical artifacts into the simulation results. One may consider reducing the numerical errors by reducing the current segment length, but this leads to a rapid increase in the number of variables. Adaptive current segment length may prove to

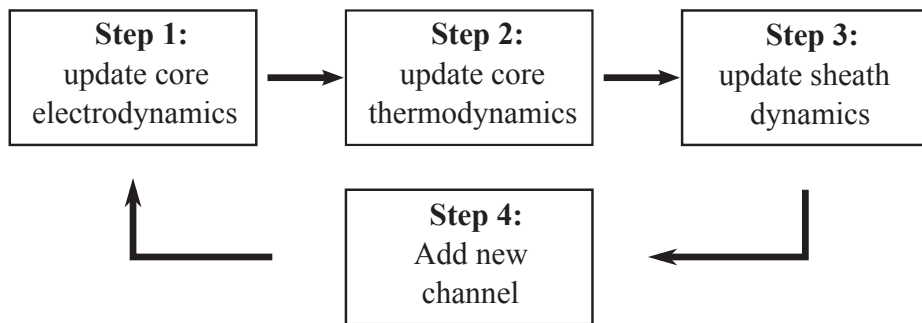


Figure 5.2: Revised computational flow for the extended model.

be effective in this situation. The development of a more proper treatment of the lightning channel tip is an important step to further improve the model in the future.

5.2 Analysis of Ground Station Recordings

The model discussed in Section 5.1 can be particularly useful in the analysis of ground station recordings of the electromagnetic signals radiated by the lightning channel as a result of the leader process. This is partly because the radiated electromagnetic field is determined only by the charge and current history in the lightning channel, and only indirectly dependent on the thermodynamics of the leader process. Moreover, as the distance between the observation point and the radiation source increases, the fine structure of the lightning channel becomes less significant.

As an example, we consider the simulation of a single negative leader step and compare the simulated and experimentally measured radiated electric field on the ground associated with this leader step. Figure 5.3 summarizes the key components of this type of study. In an ideal situation, we have complete information about the structure of the lightning channel before the single leader step which we are interested in simulating. The model is then used to simulate the current and charge redistribution in the entire channel as a result of the new leader step. The associated radiated electromagnetic waves on the ground can then be calculated. Unfortunately, this setup is currently beyond reach for several reasons such as the lack of accurate information about the in-cloud lightning channel structure and the electric field due to the cloud charge. In this respect, it is convenient to focus the study

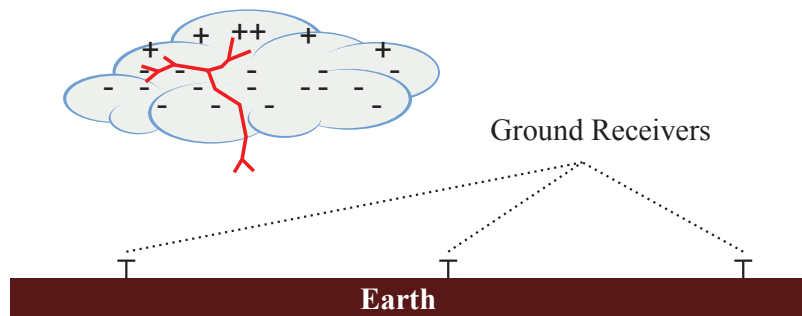


Figure 5.3: Schematics of the study of electromagnetic field recordings by ground stations using the lightning model

on the early stages of lightning channel development, such as immediately following the initial breakdown, due to their potentially simpler geometrical structure. For the rest of this chapter, we introduce a simplified setup for the simulation of a single negative leader step during the initial breakdown and then compare the simulated electric field at the ground station to experimental observations.

5.2.1 Simulation Setup

The setup for the simulation of a single leader step during the initial breakdown is shown in Figure 5.4. The location of the leader step to be simulated is provided either by the Lightning Mapping Array (LMA) or the The Huntsville Alabama Marx Meter Array (HAMMA). Both systems measure leader step locations that are associated with the impulsive electric field variations recorded by the ground receivers. For the particular flash to be considered (Section 5.2.2), the estimated locations of all the leader steps that take place during the initial breakdown are close to each other in comparison with their distances to the ground receivers. Hence their coordinate average can be used as the estimate of the leader step location. A straight channel is used to represent the unknown existing lightning channel. This is likely to be more reasonable for the initial breakdown than for the later stages of the lightning channel, since it could be the case that at the initial stage, the lightning channel is relatively less tortuous and branched. The channel length can be estimated from the LMA and HAMMA observations. The locations of the ground receivers are specified according to the locations of the HAMMA receivers. For simplicity, the direction of the leader step is

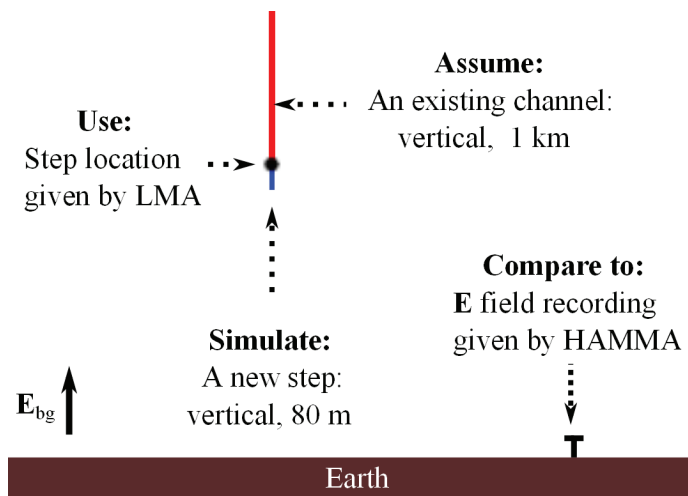


Figure 5.4: Study of electromagnetic field recordings by ground station using the lightning model

assumed to be vertically downward. At the end of this section, we suggest a way to relax this assumption.

For this particular study, we make a few further simplifications. The temperature of the channel is assumed to change according to an effective heat capacity per unit length C_1 . For this particular study, a time scale of less than 20 microseconds is considered, during which the cooling is insignificant and is thus neglected. The core temperature variation is then simply given by:

$$C_1 \frac{dT}{dt} = I_{\text{core}}^2 R_{\text{core}}$$

where R_{core} is the resistance per channel length.

We assume that the charge and current distribution in the existing lightning channel has reached steady state before the initiation of the new negative leader step. This is reasonable because there is normally a time period of the order of 50 μs between two negative leader steps [Rakov and Uman, 2002, ch. 4, p.131]. The high conductivity in the existing lightning channel ensures that the charge relaxation in the channel is on a time scale much less than this time window. For the new negative leader, we assume the entire leader is added into the system at once and make the further assumption that the entire leader is heated uniformly by the current that starts flowing in it after connection. That is, all the current segments

in the leader have the same temperature. This is achieved by first finding the total Joule heating in the leader and then evenly distributing the energy over all current segments in the leader.

5.2.2 The Huntsville Alabama Marx Meter Array (HAMMA) Observation

For both the leader step location estimation and the ground station recording of electric field variation, we use the data provided by the HAMMA system. HAMMA is a network of electric field change meters (Marx meters) located in the area surrounding the University of Alabama Huntsville. The electric field change meters have a 100 ms time constant and are sampled at 1 MHz with GPS time synchronization (i.e. bandwidth 10 Hz–500 kHz). These meters provide measurements of electric field changes associated with both slow and fast processes in lightning discharge. We focus on fast pulses measured during the initial growth of a lightning discharge on October 26, 2010 at 19:04:59 UT. Figure 5.5 shows the recording from one of the stations. The electric field associated with the initial breakdown is enlarged in the bottom panel of the figure.

5.2.3 Results

Prior to comparing to the model predictions to observations, we examine how the characteristics of the received field on the ground, such as its amplitude, duration, and the rise time of the pulses, depends on the various model parameters (Figure 5.6). Extensive parameter explorations reveal that the most relevant parameters affecting these characteristics are the specific heat of the channel C_1 , the applied background electric field E_{bg} , and the lengths of the existing channel $L_{channel}$ and the leader step L_{leader} .

To be more specific, the peak amplitude of the electric field is strongly affected by C_1 , E_{bg} , and $L_{channel}$. E_{bg} and $L_{channel}$ together determine the channel charge distribution near the leader, and thus higher E_{bg} and $L_{channel}$ lead to higher current in the channel. C_1 controls the rate at which the leader temperature and thus the conductivity varies. Smaller C_1 leads to faster increase in leader conductivity and thus shorter rise time and higher peak value of

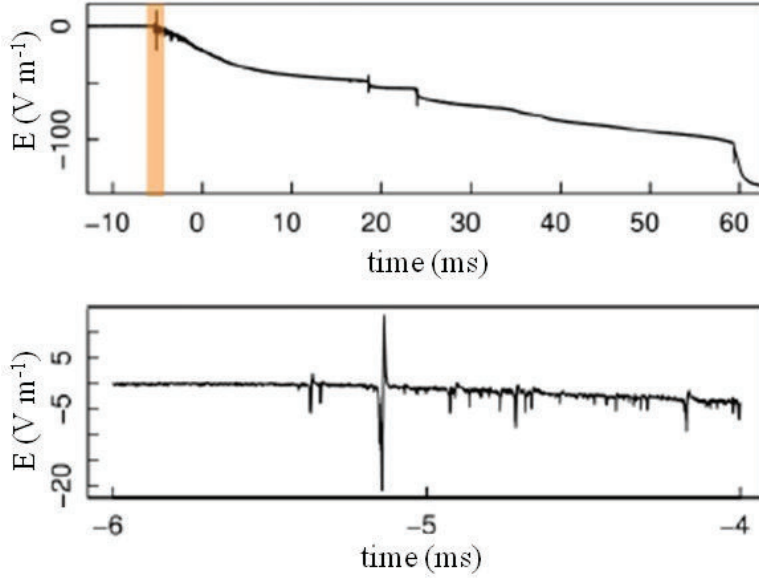


Figure 5.5: An example of the electric field variation recorded by one of the HAMMA stations

the channel current and the electric field at ground. The step length primarily affects the duration of the pulse.

By choosing appropriate parameter values, the simulated electric field can be matched to the HAMMA observation. Because experimental data of the values of E_{bg} and L_{channel} are unavailable, the peak amplitude of the simulated electric field pulse is uncertain. Thus, we only compare the shapes of the waveforms (i.e. features like rise-time, relaxation time etc) of the simulated and the HAMMA observation. That is, before a comparison is made, the simulated electric field is normalized so that it has the same peak amplitude as the observation. In the panels of Figure 5.7, we show three instances of the simulated pulse and the observation by a particular HAMMA station. For all three cases, the model parameters such as r_{core} , r_{sheath} , $\tau_{\text{c,s}}$ and C_1 are set to the same values. These parameters are related to the fundamental physics of the leader channel and are expected to be invariant from one case to another. The parameters that are tuned to ensure the match are E_{bg} and L_{leader} . These parameters represent factors that can vary for different leaders. The consistency in the theory-experiment matching suggests that the used values of r_{core} , r_{sheath} , $\tau_{\text{c,s}}$ and C_1

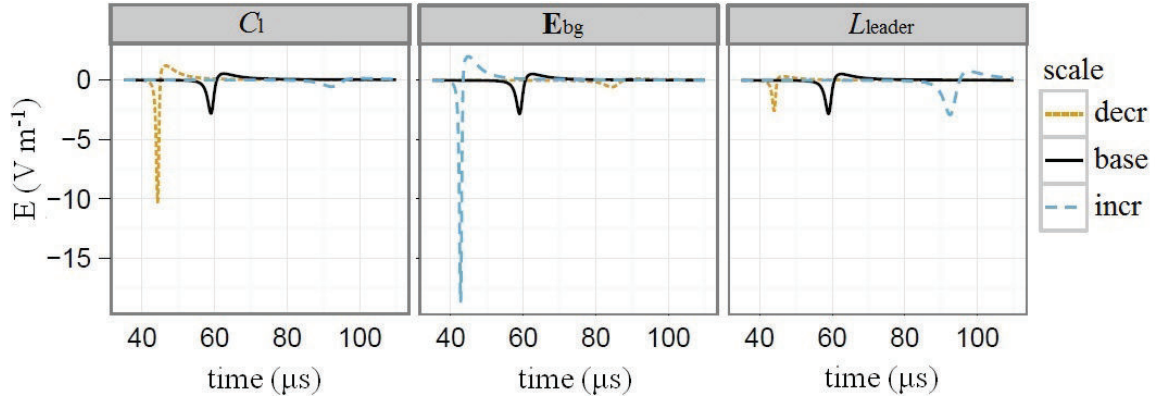


Figure 5.6: Variation in the predicted electric field with model parameters. For C_1 and L_{leader} , the parameter values are 50 %, 100 % and 200 % of the base value, labeled as three scales: 'decr', 'base' and 'incr'. For E_{bg} , the three scales are 75 %, 100 % and 125 % of the base value.

may represent averages of the actual physical values. For example, $C_1 = 2 \text{ J K}^{-1} \text{ m}^{-1}$ falls in the range of the corresponding values of high temperature air plasma in the temperature between 5000 K and 10000 K [D'Angola *et al.*, 2008].

An enhancement to the study above is to use data of electric field pulses associated with the same leader step that are recorded by several stations to further constrain the model parameters. It is also important to note that because the time scale under consideration is much longer than $1 \mu\text{s}$, the assumption of constant r_{core} can induce significant quantitative error and a more careful treatment of the radial dynamics of the core may be necessary for a more accurate model.

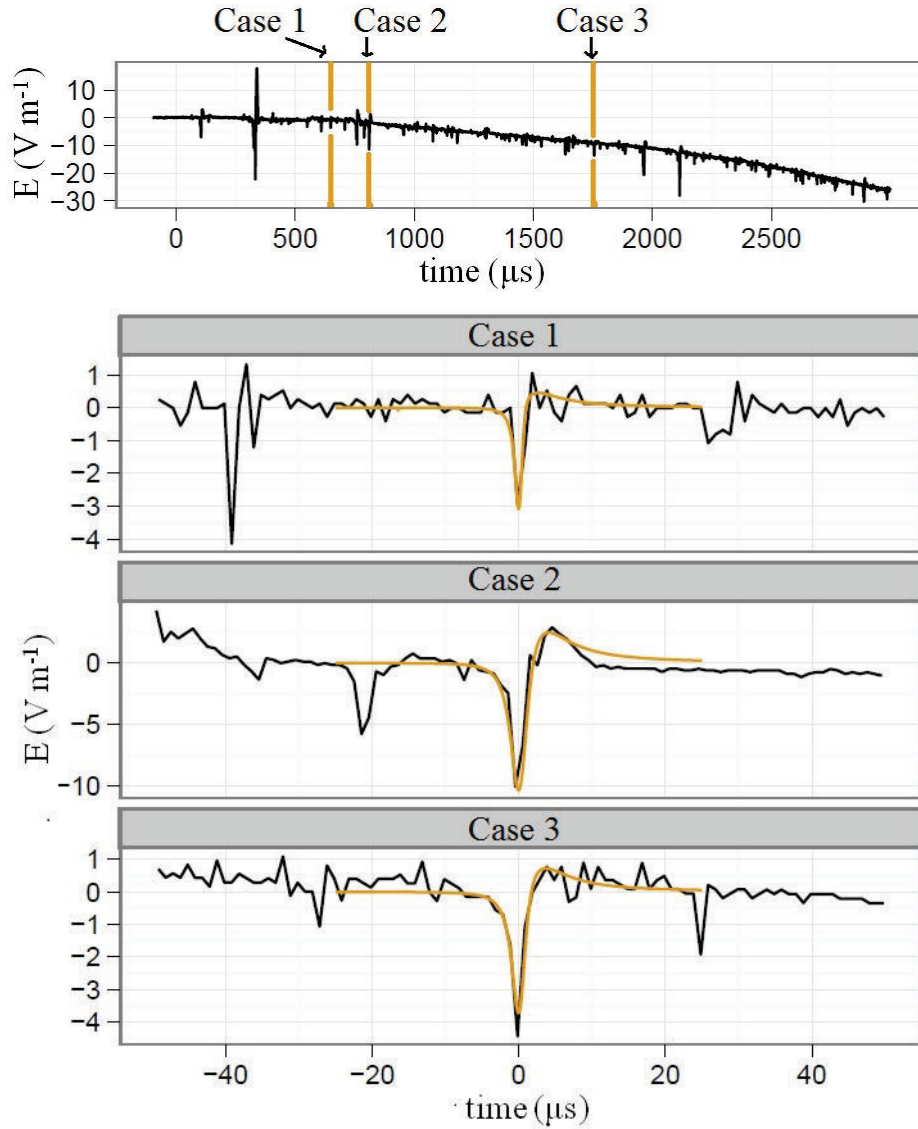


Figure 5.7: Matches for three pulses between the model prediction and data from the HAMMA observation. For all three cases, $r_{\text{core}} = 1 \text{ cm}$, $r_{\text{sheath}} = 4 \text{ m}$, $\tau_{c,s} = 0.5 \mu\text{s}$, $C_1 = 2 \text{ J K}^{-1} \text{ m}^{-1}$, $L_{\text{channel}} = 1 \text{ km}$. For case 1, $L_{\text{leader}} = 50 \text{ m}$ and $E_{\text{bg}} = 103 \text{ kV m}^{-1}$. For case 2, $L_{\text{leader}} = 200 \text{ m}$ and $E_{\text{bg}} = 125 \text{ kV m}^{-1}$. For case 3, $L_{\text{leader}} = 100 \text{ m}$ and $E_{\text{bg}} = 105 \text{ kV m}^{-1}$.

Chapter 6

Large Scale Structure of the Lightning Channel

Throughout the duration of a thunderstorm, numerous lightning flashes are initiated, with their channels spreading over a spatial region spanning tens of kilometers. It is of great interest to explore the possibilities of simulating the large scale geometrical structure of the lightning channel, for the study of lightning and cloud charge interaction as well as for the trace gas production by lightning.

The formulation using EFIE is particularly convenient for this type of study. This is because the EFIE directly evaluates the electromagnetic fields at any location due to the presence of a system of current and charge sources. As a result, the calculation of the propagating electromagnetic fields do not require a dense 3-dimensional mesh. In fact, the mesh is only needed to be defined where the current and charge sources are located. While a lightning channel may span over a spatial region with dimensions on the order of ten kilometers in each direction, its charge and current are confined within and around the channel core. The EFIE formulation takes advantage of this sparsity in lightning channel geometry to greatly reduce the number of variables in the numerical simulation. Moreover, since the numerical grid is directly specified where the core and sheath reside, the lightning channel is not confined to a predefined grid and it is straightforward to accommodate a very complicated lightning channel geometry.

From a theoretical point of view, one of the biggest obstacles for the study of large scale

lightning channel is, once again, the lack of understanding of the physics of the stepped leaders. Hence, it is not yet possible to accurately predict the leader characteristics, such as its initiation, direction, length and propagation speed. From an experimental point of view, accurate data on the lightning channel geometry and its electromagnetic environment is generally unavailable for regions inside the cloud (because of opacity), where most of the lightning channel resides. As a result, it is difficult to make detailed comparison between model predictions and observations. While these difficulties make the construction of a physically accurate model beyond reach, for practical interest, meaningful models can still be constructed by taking measures to reduce the model complexity. For the rest of this chapter, we first introduce a probabilistic model for the determination of leader characteristics and then briefly discuss a Monte-Carlo type of study based on simulations of the lightning strike location on the ground given the initial location of the lightning channel in the cloud.

6.1 The Probabilistic Leader Model

Several leader simulation methods are available for coping with the lack of understanding of the underlying physics. In particular, one type of model that is often used for the simulation of large scale geometrical structure of the lightning channel is the Fractal Lightning Models [*Riousset et al.*, 2007], which makes use of a probabilistic model for the determination of leader characteristics. On the other hand, *Mazur et al.* [2000] presents a more deterministic model that relies on various assumptions of the sheath and streamer zone for the determination of the direction and length of the leader. The former approach is favored for the large scale lightning structure simulation because of a smaller volume of computation required.

More fundamentally, because of the possibly highly chaotic streamer-leader transition processes as discussed in *Bazelyan and Raizer* [1997, Ch. 6, p. 238–243], the leader characteristics may demonstrate a certain degree of randomness even if the micro-physical processes are taken into account. Ideally, the probabilistic model could be derived either from theoretical considerations of the micro-physical processes or from extensive experimental

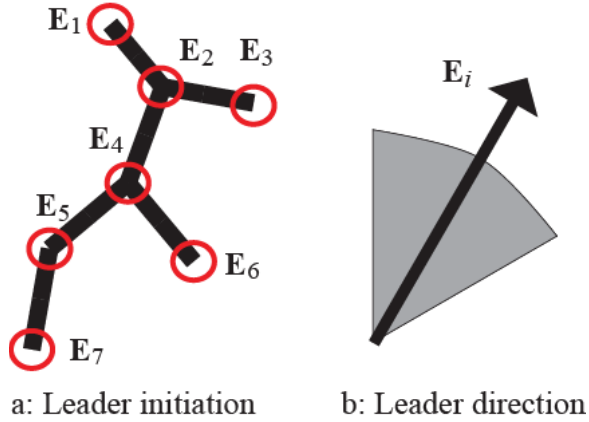


Figure 6.1: Probabilistic leader model

study of leader geometry and electromagnetic environment. However, since neither approach is possible at current stage of research, we make use of the following parametric model to determine the leader initiation, type, direction, length, and propagation speed.

At each time step, after the charge and current distribution in the core and the sheath are updated, the initiation of a leader is determined in a way similar to *Riousset et al.* [2007]. At first, the electric field \mathbf{E} is evaluated at various locations around the core (Figure 6.1a). If the magnitude of the electric field $|\mathbf{E}|$ at a location is higher than the threshold value E^k , it is considered to be a candidate where leader would initiate. After all possible leader initiation locations have been identified, the probability p of choosing a particular extension is given by:

$$p_i(\mathbf{E}_i) = \begin{cases} \frac{1}{F} ||\mathbf{E}_i| - E^k| & \text{for } |\mathbf{E}_i| > E^k \\ 0 & \text{for } |\mathbf{E}_i| \leq E^k \end{cases}$$

where \mathbf{E}_i is the total electric field at location i and $||\mathbf{E}_i| - E^k|$ is the weight for the i th location. The total electric field is the sum due to both the cloud charge distribution and lightning channel current and charge. The divisor F is the sum of all weights. Finally, one location is randomly chosen based on the probability distribution defined above. The threshold E^k is chosen to be the air breakdown electric field and can be made altitude dependent to take into account of the neutral density variation.

The leader type, direction, length and propagation speed are determined in this work

using an approach different from *Riousset et al.* [2007]. The leader type is determined by the relative direction between the electric field and the lightning channel. Since the electric field is primarily determined by the charge on the channel, the sum of the charges on the closest core and sheath segments are instead used to determine the leader type. Positive charge leads to positive leader and negative charge to negative leader. The leader direction is determined by a uniform distribution within a cone surrounding the electric field (Figure 6.1b). The length of the leader is determined by a uniform distribution within the observed range of value, 50~100 m. The leader speed is taken as 10^7 ms^{-1} . These values are chosen to be consistent with the discussion in [*Rakov and Uman*, 2002, Ch. 4, p. 131]. Note that each leader is divided into small current segments and each segment is added into the system gradually so that the averaged extension speed is the specified leader speed.

An example of a large-scale simulation is presented in Figure 6.2, with the red color representing positive charge and blue color representing negative charge.

6.2 Lightning Strike Location on the Ground

With the probabilistic leader model, the evolution of the lightning channel is a random process and Monte-Carlo type of study can be performed with the lightning model to study various lightning channel properties in a statistical sense. As an example of the potential applications of this approach, we present the study of the probabilistic distribution of the lightning strike location on the ground, given its initial location in cloud. We consider two configurations, one with and the other without a conducting protruding object on the ground. Note that if the electric field in the vicinity of the ground object rises above the air breakdown field, a leader may be initiated from the ground object and propagate upward. The initiation may be induced by an approaching downward lightning channel or simply because of the charge accumulation at the tip of the protruding object. Depending on its distance from the lightning channel, this leader may be guided by the lightning channel's electric field and propagate in an overall direction towards the lightning channel eventually connecting with it, or may propagate approximately independently from the lightning channel.

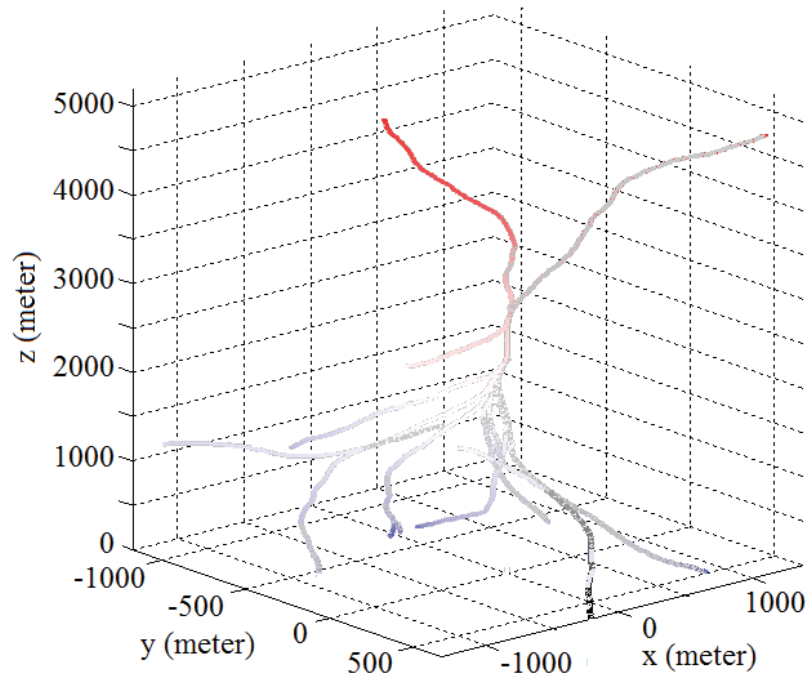


Figure 6.2: An example of the simulated large scale geometrical structure of the lightning channel and the charge distribution. The red color denotes positive charge and the blue color denotes negative charge. The cloud charge induced electric field is assumed to be uniform downward with magnitude 10^5 V m^{-1} .

6.2.1 Simulation Setup

Similar to the way done in the stepped-leader study presented in Chapter 5, the difficult problem of the lightning channel initiation is not explicitly treated. Instead, at time $t = 0$, the simulation starts with an pre-existing channel that has been created by the initial breakdown process. Before the simulation starts, charge is allowed to redistribute in its core and sheath so that the current in the core because zero. This is reasonable because both the positive and negative leaders modify the channel geometry on a time scale of tens of microseconds, while both the charge redistribution in the highly conductive core and the core-sheath charge transfer take place over time scales at least an order of magnitude smaller. The initial channel length, location and direction are model input parameters. Note that the initiation of lightning channel at a specific location is primarily determined by electrostatic fields produced by nearby charges. As a result, only the overall spatial scale of the pre-existing

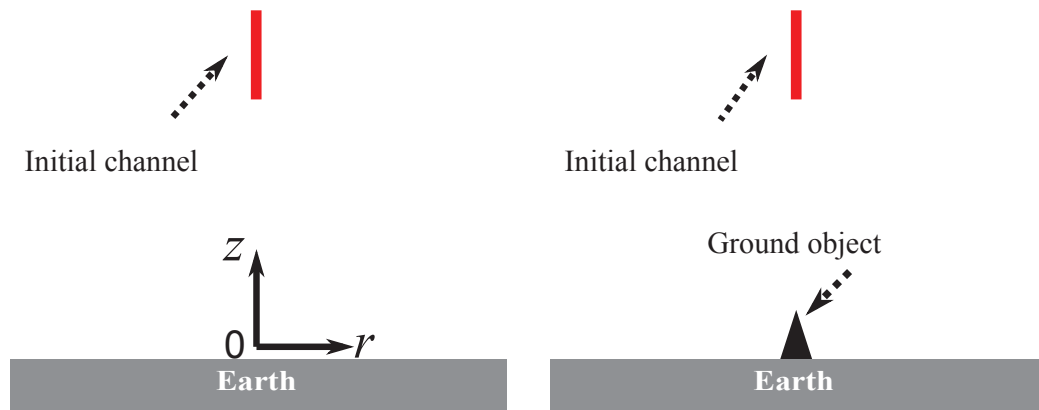


Figure 6.3: Probabilistic leader model. Left panel: leader initiation, Right panel: leader direction

channel affects the charge accumulation and in turn the channel growth after the simulation starts, while the detailed geometry of the pre-existing channel does not necessarily significantly modify future channel growth. In other words, it is reasonable to assume a straight channel with its length, direction and location as model parameters to represent the average effect of an actual pre-existing lightning channel. For a more quantitative justification of this assumption, one may consider testing with different initial channel geometry and compare the simulation results.

Another component of the model is the electric field distribution over a large spatial range due to the cloud charge. In a more elaborate model, one may consider specifying the electric field distribution using output from numerical models that simulate the cloud charge distribution or using interpolated values from experimental measurements. For the study presented in this chapter, which only intends to be a demonstration of the concept, we simply assume that the electric field due to the cloud charge is uniform.

The ground protruding object can be modeled simply as another thin lightning channel on the ground. The highly-conducting ground is, similarly to the return stroke study of Chapter 4, treated by using the method of images. It is also necessary to consider the process by which the lightning channel connects to the ground, the ground objects or the leader initiated from the ground object. This final attachment process is one of the least well observed lightning processes. Nevertheless, it is generally believed that the lightning

channel connects to the ground once its streamer zone at the channel tip overlaps with the streamer zone of an up-rising leader from a ground object. In laboratory long spark experiments, the spark leader is also observed to connect to the opposite electrode directly when its streamer zone reached the electrode. Since various observations imply that the streamer zone of a lightning channel is on the order of tens of meters, we assume that the lightning channel connects to the ground once its distance from the ground is less than 50 m, or connect to the ground object or the up-rising leader from the ground object once their distance is less than 100 m.

6.2.2 A study of lightning rod protection efficiency

In Monte-Carlo type of studies, the model is run a large number of times to create an ensemble of sample lightning channels. This ensemble forms the sample space of the random process. Various statistical properties of the large-scale geometry of the lightning channel can then be estimated by taking averages over this sample space. As an example, we consider the task of determining the lightning rod protection efficiency. At first, a large number of simulations are performed for each of the two cases: one with and the other without the lightning rod on the ground. Then for each of the two cases, the probability density per unit area of the stroke location is estimated from the simulation results. Finally, comparison is made between the two probability densities. The results are presented in Figure 6.4. The top panel of Figure 6.4 shows the probability density per unit area of the stroke location on the ground as a function of distance from the point directly below the initial lightning channel. The bottom panel is the distribution after including a ground object directly below the initiation location with a height of 60 meters. In this particular case, the ground object only modifies the strike location probability distribution in an circular area with a radius of approximately 100 meters centered at the ground object, which is equal to the assumed distance limit for the connection to take place between the lightning channel and the ground object or the up-rising leader from the ground object. In other words, the radius of protection provided by the ground object to its surrounding objects of lower height may be limited by the size of the streamer zone. One possible study that is of practical importance is to examine the variation in the ground object protection radius with its height

and location. For example, if the ground object is very tall, an upward leader may initiate and start propagating before the presence of an approaching downward leader. As a result, the upward leader propagation is less affected by the downward leader and the protection radius may vary. In order to draw conclusions of practical use, reliable leader model parameters must be obtained either by theoretical consideration or by extensive experimental observations. Also note that the lightning channel growth is highly diverging. In order to investigate local phenomena such as the variation in the protection radius by a tall object at the ground, it is necessary to perform a very large number of simulations so that enough samples reach the regions close the ground object.

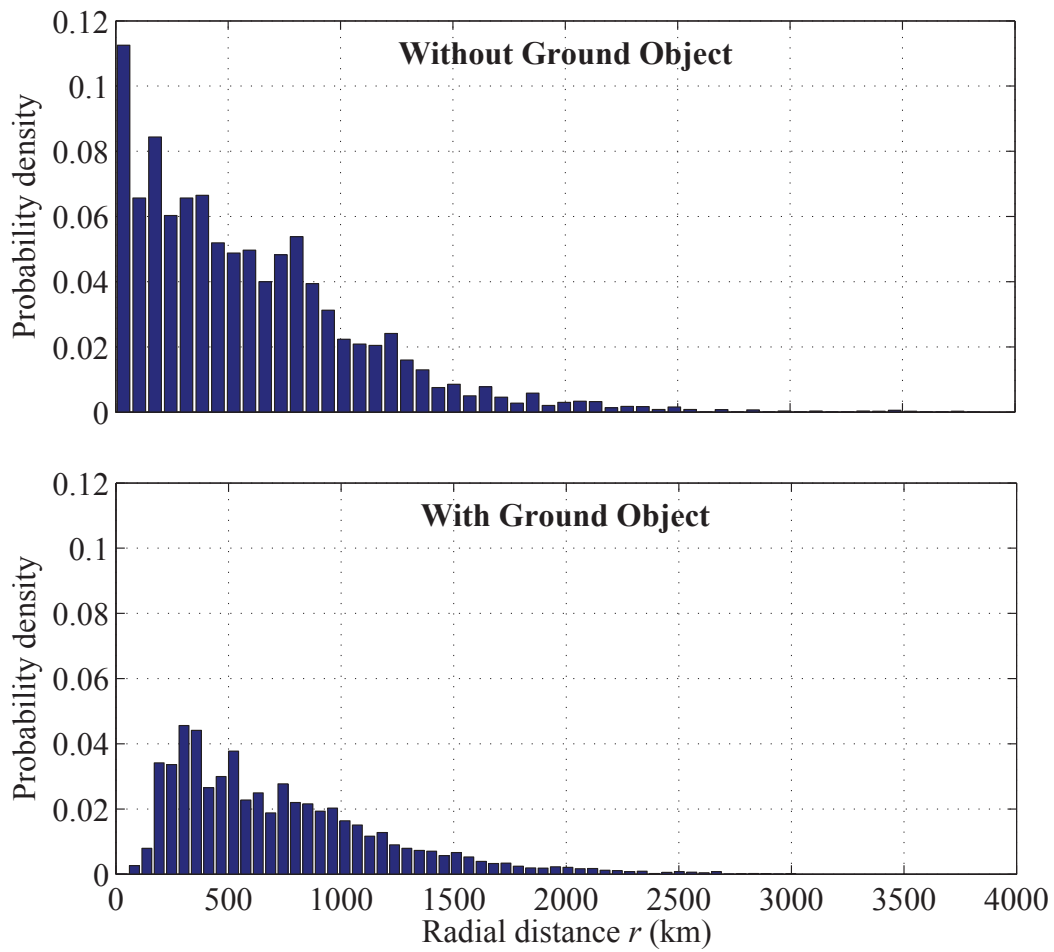


Figure 6.4: Probability density per unit area of lightning strike as a function of distance away from the center. Top panel: without ground object, Bottom panel: with ground object. Note that for the case in which the ground object is present, the probability density at the center (the ground object location) is not presented as it would be infinity. For both cases approximately 1000 simulations are used to estimate the probability density.

Chapter 7

Conclusions and Future Work

This dissertation reviews the current understanding of the physics of various lightning processes and presents a numerical lightning model that improves previous lightning simulation techniques by treating both the thermodynamics and the electrodynamics of the core, by including an empirical model of the sheath and by including a phenomenological stepped leader model with a probabilistic model to determine the leader characteristics. The dissertation also presents the application of this model to the study of the return stroke, the leader step and lightning channel large scale geometrical structure.

Most importantly, although thermodynamics of the core is generally highly complex, the dissertation demonstrates that by taking into account the hugely different spatial and temporal scales of the dynamics of the various components of the lightning channel, the system of equations that govern the high temperature plasma dynamic of the core can be greatly simplified to such a degree that the computation becomes numerically feasible.

The return stroke speed presented in Chapter 4 demonstrates that the inclusion of the thermodynamics is necessary for accurate modeling of the fast dynamics of lightning channel. The study shows that the interaction between the optical and current wave along the return stroke channel is highly nonlinear and suggests that the return stroke current wave speed propagates at a significantly higher speed than the observed optical wave speed. This finding has a profound impact on many applications that currently assume a current wave speed equal to the optical wave speed, for example for the purpose of calculating the radiated electromagnetic fields.

Limited both by the theoretical understanding and the availability of experimental data, physically accurate simulation of both a single leader step and the lightning channel large-scale geometrical structure are beyond reach. Nevertheless, Chapters 5 and 6 present partially physical models of these processes and discuss their potential applications. The leader step study in Chapter 5 compares simulations using two different models and shows that in order to reproduce the ground-observed electric field pulses associated with single steps, a greatly simplified step leader model is sufficient. The study of lightning channel large scale geometrical structure in Chapter 6 makes use of a probabilistic model to determine the leader characteristics and as an example, describes a Monte-Carlo type of study using the model to investigate the probability distribution of lightning strike location at the ground given the initial location of the channel inside the cloud.

7.1 Suggestions for future work

In order to further investigate the properties of a return stroke, many studies of practical importance can be immediately performed with the model presented in Chapter 4. Examples are the inclusion of an initial temperature and pressure gradient in the return stroke channel and accounting for the initial air composition variation due to altitude variation. These factors may have significant effects on the current and optical waveforms when the return stroke current propagating over a channel of several kilometers in length is required, for example, as an input for the study of lightning induced upper-atmosphere phenomena. In order to more accurately predict the return stroke current and optical waveforms, a more rigorous treatment of the core radial dynamics is necessary. By following the same framework discussed in Chapter 3, equations treated by gas dynamic models can be incorporated into the model for this purpose.

The dart leader is another interesting topic to study. However, in addition to the return stroke model treatment to the existing lightning channel, it is necessary to consider more carefully the treatment of the physics at the dart-leader tip, as it involves the re-creation of the core. Along this line of investigation, some interesting problems to study are the physical mechanism that is responsible for the dart leader propagation speed and the channel thermodynamic property status immediately after the dart leader and before the return

stroke.

Regarding the study of the large scale lightning channel geometrical structure, the large-scale simulations can be performed to investigate problems such as the lightning channel structure dependence on the cloud charge distribution, cloud charge removal by lightning channel and the total lightning channel length and thus the NO production per lightning flash.

Bibliography

- V. Aubrecht and M. Bartlova. Net emission coefficients of radiation in air and SF₆ thermal plasmas. *Plasma Chem Plasma Process*, 29:131–147, 2009.
- E. M. Bazelyan. Waves of ionization in lightning discharge. *Plasma Phys. Rep.*, 21:470–478, 1995.
- E.M. Bazelyan and Y. P. Raizer. *Spark Discharge*. CRC Press, Boca Raton, NY, 1997.
- K. Berger. Novel observations on lightning discharges: results of research on Mount San Salvatore. *J. Franklin Inst.*, 283:478–525, 1967.
- K. Berger, R. B. Anderson, and H. Kroninger. Parameters of lightning flashes. *Electra*, 41: 23–37, 1975.
- C. J. Biagi, M. A. Uman, J. D. Hill, D. M. Jordanand, V. A. Rakov, and J. Dwyer. Observations of stepping mechanisms in a rocket-and-wire triggered lightning flash. *J. Geophys. Res.*, 115:D23215, 2010.
- D. J. Boccippio, E. R. Williams, S. J. Heckman, W. A. Lyons, I. T. Baker, and R. Boldi. Sprites, elf transients, and positive ground strokes. *Science*, 269:1088–1091, 1995.
- W. L. Boeck, O. H. Vaughan, R. J. Blakeslee, B. Vonnegut, M. Brook, and J. McKune. Lightning induced brightening in the airglow layer. *Geophys. Res. Lett.*, 19:99–102, 1992.
- A. Bondiou-Clergerie, P. Lalande, P. Laroche, J. C. Willett, D. Davis, and I. Gallimberti. The inception phase of positive leaders in triggered lightning: comparison of modeling

- with experimental data. *Proc. 10th Int. Conf. on Atmospheric Electricity, Osaka, Japan*, pages 676–679, 1996.
- J. E. Borovsky. An electrodynamic description of lightning return strokes and dart leaders: guided wave propagation along conducting cylindrical channels. *J. Geophys. Res.*, 100: 2697–2726, 1995.
- B. E. Carlson, N. G. Lehtinen, and U. S. Inan. Terrestrial gamma ray flash production by active lightning leader channels. *J. Geophys. Res.*, 115, 2010.
- W. L. Chameides and J. C. G. Walker. A photochemical theory of tropospheric ozone. *J. Geophys. Res.*, 78:8751–8760, 1973.
- P. J. Crutzen. The influence of nitrogen oxides on the atmospheric ozone content. *Q.J.R Meteor. Soc.*, 96:320–327, 1970.
- S. A. Cummer, U. S. Inan, and T. F. Bell. Ionospheric D region remote sensing using VLF radio atmospherics. *Radio Science*, 33:1781–1792, 1998.
- K. L. Cummins, E. P. Krider, and M. D. Malone. The U.S. national lightning detection network and application of cloud-to-ground lightning data by electric power utilities. *IEEE Trans. on Electromagn. Compat*, 40(4):1781–1792, November 1998.
- A. G. D’Angola, G. Colonna, C. Gorse, and M. Capitelli. Thermodynamic and transport properties in equilibrium air plasmas in a wide pressure and temperature range. *Eur Phys J D*, 46:129–150, 2008.
- R. S. Devoto. Transport properties of ionized monatomic gases. *Phys. Fluids*, 9:1230–1240, 1966.
- H. Fukunishi, Y. Takahashi, M. Kubota, K. Sakanoi, U. S. Inan, and W. A. Lyons. Elves: Lightning-induced transient luminous events in the lower ionosphere. *Geophys. Res. Lett.*, 23:2157–2160, 1996.
- W. C. Gibson. *The Method of Moments in Electromagnetics*. Taylor & Francis Group, New York, 2008.

- B. N. Gorin, V. I. Levitov, and A. V. Shkilev. Some principles of leader discharge of air gaps with a strong non-uniform field. *IEE Conf. Publ.*, 143:274–278, 1976.
- R. A. Helliwell and J. P. Katsufakis. VLF wave injection into the magnetosphere from simple station, antarctica. *J. Geophys. Res.*, 79:2511–2518, 1974.
- R. A. Helliwell, J. P. Katsufakis, and M. L. Trimpi. Whistler-induced amplitude perturbation in VLF propagation. *J. Geophys. Res.*, 78:4679–4688, 1973.
- R. D. Hill. Analysis of irregular paths of lightning channels. *J. Geophys. Res.*, 73:1897–1906, 1968.
- R. D. Hill. Energy dissipation in lightning. *J. Geophys. Res.*, 82:4967–4968, 1977.
- R. D. Hill, R. G. Rinker, and D. Wilson. Atmospheric nitrogen fixation by lightning. *J. Geophys. Res.*, 89:1411–1421, 1984.
- P. Hubert and G. Mouget. Return stroke velocity measurements in two triggered lightning flashes. *J. Geophys. Res.*, 86:5253–5261, 1981.
- V. P. Idone and R. E. Orville. Lightning return stroke velocities in the thunderstorm research international program (trip). *J. Geophys. Res.*, 87:4903–4915, 1982.
- V. P. Idone, R. E. Orville, P. Hubert, L. Barret, and A. Eybert-Berard. Correlated observations of three triggered lightning flashes. *J. Geophys. Res.*, 89:1385–1394, 1984.
- U. S. Inan and D. L. Carpenter. Lightning induced electron precipitation events observed at $L \sim 2.4$ as phase and amplitude perturbations on subionospheric VLF signals. *J. Geophys. Res.*, 92:3293–3303, 1987.
- U. S. Inan, T. F. Bell, and J. V. Rodriguez. Heating and ionization of the lower ionosphere by lightning. *Geophys. Res. Lett.*, 18:705–708, 1991.
- A. V. Ivanovskii. Mechanism for propagation of a positive leader. *Technical Physics.*, 45: 710–719, 2000.
- J. D. Jackson. *Classical Electrodynamics*. John Wiley & Sons, Hoboken, NJ, 1999.

- D. M. Jordan and M. A. Uman. Variation in light intensity with height and time from subsequent lightning return strokes. *J. Geophys. Res.*, 88:6555–6562, 1983.
- H. Jurenka and E. Barreto. Study of electron waves in electrical discharge channels. *J. Appl. Phys.*, 53:3581–3590, 1982.
- R. Klingbeil and D. A. Tidman. Theory and computer model of the lightning stepped leader. *J. Geophys. Res.*, 79:865–869, 1974.
- P. R. Krehbiel, M. Brook, and R. A. McCrory. An analysis of the charge structure of lightning discharge to the ground. *J. Geophys. Res.*, 84(C5):2432–2456, May 1979.
- E.P. Krider. On the electromagnetic fields, poynting vector, and peak power radiated by lightning return strokes. *J. Geophys. Res.*, 97:15913–15917, 1992.
- P. Laroche, V. Idone, A. Eybert-Berard, and L. Barret. Observations of bidirectional leader development in triggered lightning flash. *Proc. 1991 Int. Conf. on Lightning and Static Electricity, Cocoa Beach, Florida*, pages 571–580, 1991.
- N. G. Lehtinen. A waveguide model of the return stroke channel with a metamaterial corona. *Radio Science*, 47:RS1003, 2012.
- N. G. Lehtinen, T. F. Bell, and U. S. Inan. Monte carlo simulation of runaway mev electron breakdown with application to red sprites and terrestrial gamma ray flashes. *J. Geophys. Res.*, 104:24699–24712, 1999.
- L. B. Loeb. Ionizing waves of potential gradient. *Science*, 148:1417–1426, 1965.
- J. J. Lowke. Predictions of arc temperature profiles using approximate emission coefficients for radiation losses. *J. Quant. Spectrosc. Radiat. Transfer.*, 14:111–122, 1974.
- D. M. Mach and W. D. Rust. Photoelectric return-stroke velocity and peak current estimates in natural and triggered lightning. *J. Geophys. Res.*, 94:6159–6164, 1989.
- G. Maslowski and V. A. Rakov. A study of the lightning channel corona sheath. *J. Geophys. Res.*, 111:D14110, 2006.

- G. Maslowski and V. A. Rakov. Dynamics of lightning channel corona sheath predicted by return-stroke models with specified longitudinal current distribution. *Publs. Inst. Geophys. Pol. Acad. Sc.*, D-73:412, 2009.
- E. A. Mason, R. J. Munn, and F. J. Smith. Transport coefficients of ionized gases. *Phys. Fluids*, 10:1827–1832, 1967.
- V. Mazur, L. H. Ruhnke, A. Bondiou-Clergerie, and P. Lalande. Computer simulation of a downward negative stepped leader and its interaction with a ground structure. *J. Geophys. Res.*, 105:22361–22369, 2000.
- E. K. Miller, A. J. Poggio, and G. J. Burke. An intergro-differential equation technique for the time-domain analysis of thin wire structures. 1. the numerical method. *J. Comput. Phys.*, 12:24–48, 1973.
- R. Moini, V. A. Rakov, M. A. Uman, and B. Kordi. A new lightning return stroke model based on antenna theory. *J. Geophys. Res.*, 105:29693–702, 2000.
- L. Niemeyer, L. Pietronero, and H. J. Wiesmann. Fractal dimension of dielectric breakdown. *Phys. Rev. Lett.*, 52(12):1033–1037, March 1984.
- R. E. Orville. A high-speed time-resolved spectroscopic study of the lightning return stroke: Part 2. a quantitative analysis. *J. Atmos. Sci.*, 25:839–851, 1968.
- A. H. Paxton, R. L. Gardner, and L. Baker. Lightning return stroke. a numerical calculation of the optical radiation. *Phys. Fluids*, 29:2736–2741, 1986.
- M. N. Plooster. Numerical simulation of spark discharge in air. *Phys. Fluids*, 14:2111–2123, 1971a.
- M. N. Plooster. Numerical model of the return stroke of the lightning discharge. *Phys. Fluids*, 14:2124–2133, 1971b.
- V. A. Rakov. Some inferences on the propagation mechanism of dart leaders and return strokes. *Journal of Lightning Research*, 1:80–89, 1998.
- V. A. Rakov. Lightning return stroke speed. *Journal of Lightning Research*, 1:80–89, 2007.

- V. A. Rakov and M. Uman. Review and evaluation of lightning return stroke models including some aspects of their application. *IEEE Trans. Electromagn. Compat.*, 40(4): 403–426, November 1998.
- V. A. Rakov and M. A. Uman. *Lightning Physics and Effects*. Cambridge Press, Cambridge, UK, 2002.
- J. A. Rioussset, V. P. Pasko, P. R. Krehbiel, R. J. Thomas, and W. Rison. Three-dimensional fractal modeling of intracloud lightning discharge in a New Mexico thunderstorm and comparison with lightning mapping observations. *J. Geophys. Res.*, 112:D15203, 2007.
- W. Rison, R.J. Thomas, P.R. Krehbiel, T. Hamlin, and J. Harlin. A GPS-based three-dimensional lightning mapping system: Initial observations in central new mexico. *Geophys. Res. Lett.*, 26(23):3573–3576, December 1999.
- M. Rubinstein, F. Rachidi, M. A. Uman, R. Thottappilli, V. A. Rakov, and C. A. Nucci. Characterization of vertical electric fields 500 m and 30 m from triggered lightning. *J. Geophys. Res.*, 100:8863–8872, 1995.
- R. K. Said, U. S. Inan, and K. L. Cummins. Long-range lightning geolocation using a VLF radio atmospheric waveform bank. *J. Geophys. Res.*, 115:D23108, 2010.
- D. D. Sentman, E. M. Wescott, D. L. Osborne, D. Hampton, and M. Heavner. Preliminary results from the sprites94 aircraft campaign: 1. red sprites. *Geophys. Res. Lett.*, 22: 1205–1208, 1995.
- D. K. Sharma, M. Israil, J. Rai, and S. C. Garg. Lightning induced heating of the ionosphere. *Atmosfera*, pages 31–38, 2004.
- R. Thottappillil and V. A. Rakov. Review of three equivalent approaches for computing electromagnetic fields from an extending lightning discharge. *Journal of Lightning Research*, 1:90–110, 2007.
- R. Thottappillil, J. Schoene, and M. A. Uman. Return stroke transmission line model for stroke speed near and equal that of light. *Geophys. Res. Lett.*, 28:3593–3596, 2001.

- R. Thottappillil, M. A. Uman, and N. Theethayi. Electric and magnetic fields from a semi-infinite antenna above a conducting plane. *J. Electrostatics*, 61:209–221, 2004.
- M. A. Uman and R. E. Voshall. The time-interval between lightning strokes and the initiation of dart leaders. *J. Geophys. Res.*, 73:497–506, 1968.
- D. Wang, N. Takagi, and T. Watanaeb. Observed leader and return-stroke propagation characteristics in the bottom 400 m of a rocket-triggered lightning channel. *J. Geophys. Res.*, 104:14369–14376, 1999.
- C.D. Weidman. Lightning return stroke speed near channel base. *Proc. 1998 Int. Lightning Detection Conf.*, 25, 1998.
- E. M. Wescott, D. D. Sentman, D. Osborne, D. Hampton, and M. Heavner. Preliminary results from the sprites94 aircraft campaign: 2. blue jets. *Geophys. Res. Lett.*, 22:1209–1212, 1995.
- Y. B. Zel'dovich and Y. P. Raizer. *Physics of Shock Waves and High-Temperature Hydrodynamic Phenomena*. Dover Publications, inc., New York, 2002.